ORNL
[redacted] MASTER COPY 16

OAK RIDGE NATIONAL LABORATORY
operated by
UNION CARBIDE CORPORATION
NUCLEAR DIVISION
for the
U.S. ATOMIC ENERGY COMMISSION

ORNL-TM-2020

FUELS AND MATERIALS DEVELOPMENT PROGRAM QUARTERLY PROGRESS REPORT FOR PERIOD ENDING SEPTEMBER 30, 1967

P. Patriarca

CLASSIFICATION CANCELLED
David R. Hamrin 8/26/2011
ADD Signature Date
Single review of CCRP-declassified documents was authorized by DOE Office of Declassification memo of August 22, 1994.

Classification Cancelled
[redacted]
By Authority Of AECM-2104 a2, B6a
By [illegible] Date AUG 21 1974

[redacted]

Full release DR 10

LEGAL NOTICE

This report was prepared as an account of Government sponsored work. Neither the United States, nor the Commission, nor any person acting on behalf of the Commission:

A. Makes any warranty or representation, expressed or implied, with respect to the accuracy, completeness, or usefulness of the information contained in this report, or that the use of any information, apparatus, method, or process disclosed in this report may not infringe privately owned rights; or

B. Assumes any liabilities with respect to the use of, or for damages resulting from the use of any information, apparatus, method, or process disclosed in this report.

As used in the above, "person acting on behalf of the Commission" includes any employee or contractor of the Commission, or employee of such contractor, to the extent that such employee or contractor of the Commission, or employee of such contractor prepares, disseminates, or provides access to, any information pursuant to his employment or contract with the Commission, or his employment with such contractor.

[redacted]

ORNL-TM-2020

Contract No. W-7405-eng-26

FUELS AND MATERIALS DEVELOPMENT PROGRAM QUARTERLY PROGRESS REPORT FOR PERIOD ENDING SEPTEMBER 30, 1967

Compiled by

P. Patriarca

FEBRUARY 1968

OAK RIDGE NATIONAL LABORATORY
Oak Ridge, Tennessee
operated by
UNION CARBIDE CORPORATION
for the
U.S. ATOMIC ENERGY COMMISSION

[redacted]

[redacted]

[redacted]

FOREWORD

This is the fourteenth quarterly progress report describing work performed at the Oak Ridge National Laboratory for the Fuels and Materials Branch, Division of Reactor Development and Technology, U.S. Atomic Energy Commission. The specific programs covered are as follows:

Program Title	Person in Charge	Principal Investigator(s)
Part I. Metals and Ceramics Division		
Development and Testing of Sol-Gel Oxide Fuel for LMFBR	P. Patriarca	A. L. Lotts J. L. Scott R. G. Wymer*
Fuel Element Fabrication Development	G. M. Adamson, Jr.	W. R. Martin
Mixed Nitride Fuels Development	W. O. Harms	J. L. Scott
Nondestructive Test Development	W. O. Harms	R. W. McClung
Sintered Aluminum Products Development	G. M. Adamson, Jr.	W. R. Martin D. G. Harman
Zirconium Metallurgy	C. J. McHargue	P. L. Rittenhouse
Weldability of Nickel-Bearing Alloys	G. M. Adamson, Jr.	G. M. Slaughter
Part II. Reactor Chemistry Division		
Fission-Gas Release and Physical Properties of Fuel Materials During Irradiation	O. Sisman	R. M. Carroll J. G. Morgan
Part III. Solid State Division		
Irradiation Effects on Alloys and Structural Materials	D. S. Billington	J. T. Stanley

*Chemical Technology Division.

[redacted]

CONTENTS

Page

Summary ix

Part I. Metals and Ceramics Division

1. Development and Testing of Sol-Gel Oxide Fuel for LMFBR 3
   - Preparation of $(U,Pu)O_2$ Sol-Gel Material 3
   - Plutonium Ceramics Facilities 4
     - Building 3019 Facilities 6
     - Building 4508 Facilities 6
   - Development of Sol-Gel $(U,Pu)O_2$ Fabrication Techniques 7
     - Sphere-Pac Development 8
     - Sol-Gel UO_2 and $(U,Pu)O_2$ Pellet Development 9
   - Characterization of Sol-Gel $(U,Pu)O_2$ Fuels 16
     - Thermodynamic Evaluations of the $(U,Pu)O_2$ System 17
   - Irradiation Testing of Sol-Gel $(U,Pu)O_2$ Fuels 18
     - Noninstrumented Screening Type Irradiation Tests 19
     - Oak Ridge Research Reactor Instrument Irradiation Tests . 24
     - Transient Testing of Sol-Gel-Derived $(U,Pu)O_2$ Fuels . . . 25
     - Fast Flux Irradiation Tests of Sol-Gel $(U,Pu)O_2$ Fuels . . 25
     - Gas-Cooled Fast Reactor Program 26
2. Fuel Element Fabrication Development 27
   - Fabrication of Miniature Fuel Plates to Evaluate Cheaper and Better Fuels 27
     - Reduction of Swelling in U_xAl_y Compacts by Alloying . . . 36
     - Evaluation of Fuel Homogeneity in Blends, Compacts, and Rolled Plates 38
     - Ultrasonic Nonbond Detection in Experimental Fuel Plates . 39
     - Investigation of Surface Films on Aluminum Fuel Plates . . 40
   - Conversion of UF_6 to UO_2 with a Flame Reactor 41
   - Preparation of PuO_2 Powder from PuF_6 by Chemical Vapor Deposition 45

[redacted]

[redacted]

Page

3. Mixed Nitride Fuels Development 46
   Fabrication of Mixed Nitrides 47
      Synthesis 47
      Powder Consolidation 48
      Pseudobinary System UN-PuN 49
   Nitride Fuel Cycle Studies 50
   Thermodynamics of Plutonium Nitride 50
      Phase Data 51
      Vaporization 52
      Thermodynamics 52
      Experimental 52
   Synthesis of Uranium Nitride and Production of Fine Precipitates in It 53
      New Synthesis Facility 54
      Microstructural Variations in Sintered UN Arising from Synthesis of the Powder 56
      Preparation of Materials for Dispersion Studies 56
4. Nondestructive Test Development 58
   Electromagnetic Test Methods 58
      Analytical Studies 58
      Phase-Sensitive Eddy-Current Instrument 59
   Ultrasonic Test Methods 60
      Ultrasonic Frequency Analysis 60
      Optical Visualization of Ultrasound 62
5. Sintered Aluminum Products Development 65
   Dispersion Preparation 65
   Powder Consolidation 66
   Mechanical Property Evaluation of SAP 67
   Secondary Working of SAP 76
   Nondestructive Evaluation of SAP 77
   Advanced Sintered Aluminum Products 78

[redacted]

[redacted]

Page

6. Zirconium Metallurgy 82
   Anisotropy in Zircaloy 82
      Tubing Test Program 82
      Torsion Tests 82
   Circumferential Texture Gradients in Zircaloy Tubing 85
   Texture Development in Single-Crystal Zirconium 89
      Schmid Factors 89
      Rolling Textures 92
   Inhibition of Oxidation by Anodic Films 92
   Phosphorus Concentrations in Anodic Films Formed in H_3PO_4 . 94
7. Weldability of Nickel-Bearing Alloys 97
   Special Alloy Fabrication 97
   Hot-Ductility Testing 98
   VARESTRAINT Testing Performed under Subcontract at Rensselaer Polytechnic Institute 102

Part II. Reactor Chemistry Division

Fission-Gas Release and Physical Properties of Fuel Materials During Irradiation 107
   Steady-State Fission-Gas Release from UO_2 Single-Crystal Specimen C1-19 108
   Steady-State Fission-Gas Release from Fine-Grain UO_2 Specimen C1-20 111
   Cooling Bursts and Iodine Release 115
   Computer Program for Defect-Trap Model 116

Part III. Solid State Division

Irradiation Effects on Alloys and Structural Materials 119
   Radiation Effects on Pressure-Vessel Steels 122
      Effects of Irradiation Temperature and Post-Irradiation Annealing 122
      Effect of Thermal Neutron Damage 130
      Fracture Appearance Measurements 131

[redacted]

[redacted]

Page

Effect of Interstitial Solutes on Radiation Hardening in Iron 133

Introduction 133

Material 135

Irradiation 136

Results 137

Observation of Neutron Irradiation Damage in Niobium by Transmission Electron Microscopy 139

Materials and Experimental Procedures 140

Experimental Results and Discussion 141

The Effect of Oxygen on "Stage III" Annealing in Neutron-Irradiated Niobium 144

Introduction 144

Experimental Procedures 146

Results 147

Discussion 149

Radiation Hardening in B.C.C. Metals Niobium and Iron . . . 152

Introduction 152

Experimental Procedure 154

Experimental Results 155

Discussion 159

Dislocation Mobility in Single Crystal Niobium 165

[redacted]

[redacted]

SUMMARY

PART I. METALS AND CERAMICS DIVISION

1. Development and Testing of Sol-Gel Oxide Fuel for LMFBR

We initiated a program for the preparation, development, and testing of sol-gel-derived fuels for the LMFBR. In preparation for the full scope of the program, we complemented our existing plutonium-handling facilities by installing a pilot-scale facility for the preparation of UO_2-PuO_2 sol-gel material. This facility operates at a capacity of 200 g of plutonium per day. We are also in the process of installing additional equipment for the fabrication and out-of-reactor characterization of plutonium-bearing materials.

We have used routinely the Sphere-Pac method of loading two-size fractions of microspheres to obtain densities in the range of 83 to 84% volume packing in cylindrical rods. Attempts have been made to increase the packing density by use of a larger number of size fractions, but as yet this work has not been successful. Pellets of UO_2 ranging from 67 to 93% of theoretical density have been made from a variety of materials including whole microspheres, crushed microspheres, dried sol-gel shards, and sol that had been freeze dried.

To prepare for a full-scale test program for out-of-reactor characterization of material, we have conducted literature searches and outlined the programs comprehensively. One of the efforts has been to use available thermodynamic data on the $(U,Pu)O_2$ system to understand and predict the compatibility of mixed oxide fuels with cladding materials.

The irradiation test program was initiated, and two of the five capsules in the noninstrumented series for the ETR were removed after one cycle of ETR operation. This was because one capsule had failed near the scheduled end of a reactor cycle. Our burnup analyses have shown that the fuel had operated at an average heat rating greater than 1400 w/cm. Concurrent with the start of the ETR irradiation tests, we had initiated the development of an improved calculational procedure for highly enriched fuels and particularly for plutonium-containing fuels in

[redacted]

thermal flux irradiations. The procedure involved the use of an existing code called ANISN. The procedure predicts heat ratings that closely match those derived from the burnup analysis of the two capsules which were removed from the ETR. Consequently, all additional capsules, including the three currently being irradiated in the ETR, have had their operating conditions established by the improved calculational procedures. Design of ORR instrumented irradiation tests, transient tests, and fast flux irradiation tests has been initiated.

2. Fuel Element Fabrication Development

Factors affecting plate fabrication and irradiation performance for research reactor fuel elements are being examined to evaluate cheaper and better fuels. Miniature fuel plates containing high fuel loadings of two basic types each of fuels, U_3O_8 and U_xAl_y, are being made. Initial results indicate the fabricability of compacts was very different for two grades of each type of fuel. We are evaluating the fuel homogeneity in powder blends, fuel compacts, and rolled plates by x-ray attenuation and radiography for both types of fuel. Ultrasonic nonbond detection of experimental fuel plates is in progress.

A small effort has continued on the direct conversion of fissionable halides to refractory fuel compounds using the "flame reactor" concept. Submicron-size powders having suitable chemistry including fluorine contents less than 10 ppm have been produced at a rate of 5 kg per day. An economic evaluation of this technique is under way.

3. Mixed Nitride Fuels Development

The literature on synthesis, fabrication, and properties of mixed uranium-plutonium nitrides was surveyed. We concluded that mixed nitrides might best be prepared by synthesis and blending of the two pure nitrides. For fabrication by cold-pressing and sintering, the particle size and oxygen contaminant seem to be the main factors of concern in obtaining high densities. Alternate fabrication techniques are uniaxial and isostatic hot pressing.

We showed that "UC_2" can be prepared from sol-gel UO_2 by solid-state reaction with powdered graphite in argon and studied the kinetics of the reaction. We are now studying the further conversion of this "UC_2" to the U(C,N) solid solution by reaction with nitrogen. A second kinetic study will be made on the direct conversion of carbon-containing UO_2 microspheres to carbonitride.

We are critically reviewing thermodynamic and phase information on the plutonium-nitrogen system to define the areas where data are lacking. Our first experimental work will be measurements of the nitrogen pressure over PuN(s) + Pu(ℓ). The necessary equipment is being designed for glove-box operation.

Materials are being obtained for continuing experiments on formation of fine-particle dispersions in UN.

4. Nondestructive Test Development

We are developing new techniques and equipment for the nondestructive evaluation of materials and components. Major emphasis has been on eddy-current, ultrasonic, and penetrating-radiation methods.

Our analytical work on electromagnetic phenomena is being directed to preparation of programs for use on a time-sharing computer to evaluate the integrals for closed-form solutions which we developed. To simplify construction and maintenance of the portable phase-sensitive instrument, printed circuit boards were developed.

A portion of the ultrasonic program has been directed toward development of equipment for measurement of the frequency spectrum in ultrasonic pulses. Preliminary application has shown that some commercial transducers are not providing the expected output. A closed-circuit television system was coupled to our optical system for viewing ultrasonics. This addition eases viewing problems and allows faster study of parameters.

5. Sintered Aluminum Products Development

Our program has been to investigate the problems and parameters related to primary billet fabrication of SAP. After the preparation of specifications for atomized powder, ball-milling of these powders to produce flake, and selection of a billet consolidation process, we fabricated several large billets using the selected parameters. The conclusion of this phase of our program will be the evaluation of these billets. Our nondestructive testing effort has been concerned with the development of alternate techniques for determination of flake thickness and oxide content of aluminum powders.

Since the properties of the end product are influenced by the manner in which the consolidated billet is reduced, we have initiated a program to evaluate the secondary metalworking of SAP.

The results of our program to produce a primary billet fabrication specification were successful in producing a reproducible product but have indicated that this phase of SAP preparation does not significantly alter the low creep ductility. We have selected several alloying approaches to improve the creep ductility. Currently we are preparing these alloys using the industrially oriented billet process specification that was developed last year.

6. Zirconium Metallurgy

The yield strength of Zircaloy tubes tested in torsion is directly related to crystallographic texture. When most of the basal poles are oriented radially, low torsion yield strength is found. Material with tangentially oriented basal poles has a torsion yield greater than its axial tensile yield strength.

We observed noncircular cross sections in Zircaloy tube specimens tested in tension. This led to the discovery that circumferential texture gradients exist in these materials. We believe we can explain these gradients in terms of certain details of the fabrication procedure.

A computer program was developed to calculate Schmid factors for slip and twinning in zirconium specimens oriented in any position and

subjected to any combination of three orthogonal stresses. Texture diffractometer study of rolled zirconium single crystals has confirmed our preliminary results on texture development.

Corrosion tests of zirconium and zirconium alloys in 360°C water (2700 psi) have been started to test further the inhibiting effect of preanodizing in H_3PO_3. Preliminary results are encouraging. We have also begun examination of the oxide-metal epitaxial relationship in air-oxidized zirconium single crystals. Study of a 2000-A film on the basal plane showed that the (0001) of the metal is oriented very strongly parallel to the (100) of the monoclinic oxide.

The phosphorus concentration in anodic zirconium oxide films formed in H_3PO_4 was found to vary from 1 to 7% (by weight), depending on the anodizing conditions. Both high concentration of H_3PO_4 in the anodizing solution and high current density promote a high concentration of phosphorus in the anodic film.

7. Weldability of Nickel-Bearing Alloys

We are accumulating data on the effects of minor elements, individually and combined, upon the cracking behavior and mechanical properties of several special heats of Incoloy 800. Our VARESTRAINT results on high-purity heats containing controlled amounts of aluminum and titanium show that both these elements increase susceptibility toward hot cracking. Hot-ductility studies with the Duffer's Gleeble show a lowering of the zero-strength temperatures with increasing aluminum and titanium content; this is probably associated with melting-point depression. In addition, there is the surprising indication that sulfur and phosphorus additions to titanium- and aluminum-doped alloys have no apparent systematic effect on hot ductility. It is postulated that the titanium and aluminum combine with the sulfur and phosphorus in these alloys to neutralize their effects.

[redacted]

PART II. REACTOR CHEMISTRY DIVISION

Fission-Gas Release and Physical Properties of Fuel Materials During Irradiation

A fine-grain UO_2 specimen was used to obtain fission-gas release measurements at temperatures up to 1700°C. At 1700°C definite signs of structure change was implied by increased gas release and sudden small bursts of gas. When the specimen was cooled quickly, a very large burst of gas was measured; also some spontaneous bursts of gas were emitted after the specimen was cooled. The bursts are believed to be caused by microcracks in the specimen. The high-temperature run had a beneficial effect on the fission-gas retention of the specimen at lower temperatures. After the 1700°C run the gas-release rate at lower temperatures was only about half of the value just before the 1700°C run.

Postirradiation examination of a single-crystal UO_2 specimen irradiated to a high burnup (about 9×10^{19} fissions/cm^3) and high temperature (1700°C) shows collection of gas bubbles on subgrain boundaries and regions of high stress probably caused by the collection of interstitials into large defect traps.

PART III. SOLID STATE DIVISION

Irradiation Effects on Alloys and Structural Materials

The radiation embrittlement of weld heat-affected-zone (HAZ) samples and base-plate samples of ASTM A-212B pressure-vessel steel is being investigated as a function of radiation dose and temperature. The increase in ductile-brittle transition temperature is sharply reduced for irradiation temperatures above 300°C. Preliminary results indicate no systematic differences in dependence on irradiation temperature for HAZ samples as compared to base-plate samples. Samples shielded with cadmium exhibited the same degree of embrittlement as unshielded ones, thus suggesting that the embrittlement is relatively insensitive to thermal neutrons. Quantitative measurements of the relative amounts of

[redacted]

shear and cleavage fracture appearance were made; the fracture appearance indicates a narrower transition from ductile to brittle behavior than the fracture energy, but the two properties are in essential agreement.

Tensile tests, electrical resistivity measurements, and internal friction measurements were conducted on unirradiated and irradiated vacuum-melted iron with and without the addition of 20 wt ppm of nitrogen. Annealing experiments following irradiation at −50 to −95°C showed an annealing stage at 35°C in the Fe–20 wt ppm N material that is not present for the nitrogen-free iron. This is attributed to the trapping of nitrogen at radiation-produced defects. The tensile samples indicated an increase in yield stress upon irradiation, followed by a further increase upon annealing in the range −35 to 100°C. However, this was observed for samples of both nitrogen contents.

Defect clusters and dislocation channeling were observed in neutron-irradiated niobium for the first time; a dose of 2×10^{18} neutrons/cm^2 ($E > 1$ MeV) produced a spot density of approximately 5×10^{15}/cm^3. The spot size distribution showed a peak at a spot diameter of about 80 A.

As a result of resistivity and internal friction measurements, the post-irradiation annealing stage in niobium at 150°C ("Stage III" annealing) was shown to be due to the motion of oxygen to radiation-produced defects. The activation energy was 1.19 eV. No Stage III annealing was observed after cold work for a low-oxygen niobium sample.

The temperature dependence of the yield stress in single-crystal niobium was virtually unchanged by neutron irradiation, in agreement with previous results from iron. This indicates that the mechanism for the thermal activation of flow is not affected by the radiation-produced defects. A mechanism of radiation hardening in bcc metals by contact interaction between dislocations and damage clusters is formulated and is compared with the experimental results on irradiated niobium.

The stress dependence of dislocation velocity was measured directly by etching techniques for unirradiated niobium as a function of temperature and number of zone passes and for irradiated single-zone-pass niobium at room temperature. In all cases, the equation $\bar{v} = (\tau/\tau_o)^{m^*}$

[redacted]

was obeyed. For decreasing test temperatures in the range 300 to 77°K, m^* is not greatly changed and τ_o is greatly increased. Preliminary results at room temperature indicate a decrease in m^* and an increase in τ_o upon irradiation. Indirect measurements of m^* by change-in-strain rate tests and stress-relaxation tests did not agree with m^* determined by the etching technique.

[redacted]

[redacted]

PART I.

METALS AND CERAMICS DIVISION

[redacted]

[redacted]

[redacted]

[redacted]

1. DEVELOPMENT AND TESTING OF SOL-GEL OXIDE FUEL FOR LMFBR

A. L. Lotts

The development and testing of sol-gel-derived PuO_2-UO_2 fuel are being done to assess the potential of the fuel for use in liquid-metal-cooled fast breeder reactors and the Fast Flux Test Facility. The effort involves (1) the preparation of PuO_2-UO_2 fuel by the sol-gel process, (2) out-of-reactor testing to characterize the sol-gel product, (3) the development of fabrication procedures for incorporating the mixed oxide fuel into a suitable fuel rod component, and (4) the irradiation testing of the fuel.

The program was initiated in late fiscal year 1967; and, accordingly, our activities have necessarily emphasized those tasks that provide the facilities, experimental design, and equipment to accomplish a broad spectrum of work. The activities have included (1) the construction of a pilot-scale facility for the preparation of PuO_2-UO_2 products by the sol-gel method; (2) the addition of equipment to the plutonium laboratories for out-of-reactor characterization of material and for additional fabrication methods; (3) the development of procedures for sphere packing of UO_2-PuO_2 microspheres and the development of a method for making UO_2 and UO_2-PuO_2 pellets from sol-gel-derived material; and (4) the irradiation of noninstrumented capsules in the ETR to test the Sphere-Pac UO_2-PuO_2, the initiation of the design of an instrumented capsule for the ORR, and preliminary work in preparation for transient testing and fast flux testing of sol-gel materials.

Preparation of $(U,Pu)O_2$ Sol-Gel Material

R. W. Horton[1]

The sol-gel work reported in this section is part of a larger program on sol-gel process development and demonstration supported at ORNL. The work reported here is that being carried out in the Chemical

[1]Chemical Technology Division.

[redacted]

Technology Division Pilot Plant. An alpha-contained and shielded facility for producing 200 g/day of plutonia sol by a precipitation-peptization process has been installed in the pilot plant. The facility also provides for blending urania and plutonia sols, forming them into microspheres, and drying and firing them to dense, homogeneous oxide spheres at the rate of 1 kg/day of final mixed oxide. The equipment, shown in Fig. 1.1, is currently being checked out with plutonium.

Plutonium Ceramics Facilities

J. D. Sease E. S. Bomar
M. K. Preston[2] W. H. Pechin

Plutonium facilities are being developed in support of both the sol-gel and mixed-nitride fuel programs and are located in laboratory space in Buildings 4508 and 3019. Together the two locations will accommodate about 35 glove boxes. Building 3019 already contains a variety of experimental work with plutonium-bearing fuels, including pilot-plant operations; therefore, it satisfies the needs of secondary containment. A single laboratory, previously used for research on beryllium oxide in Building 4508, was modified to meet the needs of secondary containment there.

The boxes in Building 3019 will contain most of the equipment for fabrication of fuel rods and irradiation capsules, metallography, and microradiography and for some fuel-preparation procedures. The design of some of the boxes will permit the use of an inert atmosphere. The equipment in Building 4508 will be directed mainly toward the development of fuel-preparation techniques and the characterization of the structure, composition, and thermal properties of fuels. All of the boxes planned for the Building 4508 laboratory were designed to contain an inert atmosphere of high purity. The atmosphere will be provided initially by a one-pass purge system, but this will be replaced eventually with a closed loop and purifier. Twenty-two glove boxes either have been delivered or are in various stages of construction, inspection, and shipment. The status of work in the two buildings follows.

[2]General Engineering Division.

Fig. 1.1. A Front View of the Alpha-Contained Plutonia Sol Preparation and Microsphere-Forming Facility in the ORNL Pilot Plant.

Building 3019 Facilities

A design for equipment to extrude sol-gel pastes was completed. Freeze-drying and tray-drying apparatus was designed and fabricated. The drying units have been placed in a 6 × 3 ft glove box along with a "Shatterbox" grinder and a sigma mixer to prepare powders for making sol-gel mixed-oxide pellets.

Some progress was made on the distribution station, which will provide an argon atmosphere for the metallography box complex, the ultrasonic drill, the centerless grinding, and the plutonium storage boxes.

The glove box and furnaces for sintering and heat treatment have been installed and are being checked. Two of the furnaces have platinum-rhodium windings, and the other will use either a carbon or tungsten heating element. The equipment description, operating procedures, and hazards review have been prepared for the approval of the Radiochemical Plant Committee.

Seven of the nine metallography glove boxes fabricated by Stainless Equipment Company of Denver, Colorado, were received. Leak testing of the transfer boxes containing plexiglas windows was not completed because of outgassing problems with the plexiglas.

Installation and checking of the centerless grinder and its glove box have continued. A number of modifications were made, such as extension of the grinder shaft and relocation of the motor-driven workhead, and we are now making the final alignment and check of this device.

Detailed design was started on the bellows, alpha seal, camera support, and lens-adjusting system for the glove-box macrocamera installation.

Building 4508 Facilities

An initial design of components for a glove-box gas-purge and pressure-compensating system were completed. Since the pressure compensator, which was intended to maintain a subatmospheric pressure by compensating for pressure surges caused by glove movement, did not function satisfactorily, we are considering using with some modification

a regulating system devised by Harwell, one by Mound Laboratory, or a combination of the two.

The 6-in. diffusion pump was installed under the compatibility glove box, and the induction-heated vacuum furnace was fabricated.

Modification of the "Shatterbox" grinder glove box did not satisfactorily reduce vibration, and a new arrangement will be tried as soon as additional components are fabricated.

A conceptual design was prepared for an induction-heated hot press with a capacity of 10 tons, and a detailed design now is being made.

Conceptual designs and layouts for the bell-jar mounting and the lifting mechanism for the thermal conductivity equipment were completed and approved and the overall configuration of the glove boxes was determined. The design of the glove boxes is under way, and detailed design of the bell-jar lifting equipment was started.

Fabrication of ten boxes to house equipment in the laboratory is progressing at the Stainless Equipment Company. We have boxes on hand to contain the following equipment and processes: compatibility rig, powder conditioning, "Shatterbox" grinder, small hot press, differential thermal analysis and thermogravimetric analysis, nitride synthesis and sintering, and decontamination and preparation of x-ray diffraction samples.

A specification was compiled for a tungsten resistance element furnace having a 4-in.-diam, 6-in.-long heated chamber, and the bids received from four vendors are being evaluated.

Development of Sol-Gel $(U,Pu)O_2$ Fabrication Techniques

J. D. Sease R. L. Hamner
A. R. Olsen

The sol-gel process as developed at ORNL will yield four products each suitable for a different fabrication process. These products include microspheres for Sphere-Pac, dense angular particles for Vi-Pac, a concentrated sol for extrusion, and a sinterable powder for pelletization. Each of these four fabrication processes is being developed for application to the fabrication of $(U,Pu)O_2$ fuel rods for LMFBR application.

The current status of sol-gel fuel fabrication procedure development and a preliminary economic analysis of the various processes were reported recently.[3,4]

Sphere-Pac Development (R. B. Fitts, A. R. Olsen)

The Sphere-Pac fabrication process utilizes sol-gel microspheres and employs a sequential loading procedure with low-energy vibration as the compaction force. The initial process[5] was developed using two sizes of microspheres. The large size fraction was 500- to 420-μ-diam spheres from the sphere-forming column, and the fine fraction was less than 44-μ-diam spheres from the stirred-pot process. This technique, which produces fuel loadings of 83 to 84% volume packing in cylindrical rods, has been used to fabricate our initial $(U,Pu)O_2$ irradiation test rods. Since the final smear density required for high-burnup LMFBR oxide fuels has not yet been established but may be as low as 80% or as high as 90%, we are continuing our Sphere-Pac development. Our current program is aimed at establishing the practical maximum volume loading percentage.

There are two possible approaches to the production of 88 to 92% volume packing fractions by the Sphere-Pac technique. In one, the binary bed may be reinfiltrated with a third size fraction to obtain a theoretical density of about 93%. However, this requires a total size spread of 77:1 between the largest and the smallest size fraction and because of production and handling limitation appears to be the more difficult technique. The second approach, on which we have just begun our investigation, is to use a two-size coarse fraction, which can be blended before loading, and a single infiltration with a fine fraction having a diameter only one-seventh of the smallest diameter in the coarse mixture.

---

[3]A. R. Olsen, J. D. Sease, R. B. Fitts, and A. L. Lotts, Fabrication and Irradiation Testing of Sol-Gel Fuels at Oak Ridge National Laboratory, ORNL-TM-1971 (September 1967).

[4]T. N. Washburn, A. L. Lotts, and F. E. Harrington, Comparative Evaluation of Sol-Gel Fuel Fabrication Costs, ORNL-TM-1979 (September 1967).

[5]A. R. Olsen and J. D. Sease, Metals and Ceramics Div. Ann. Progr. Rept. June 30, 1966, ORNL-3970, p. 220.

Preliminary results indicate that microspheres may be mechanically mixed in size ratios up to about 4:1 without gross segregation. Such mixtures raise the coarse packing fraction from 62.5% for a single size to about 72.5% for the mixture. This would give a theoretical final packing of slightly over 89%. We have not yet achieved this packing fraction, but we are continuing to investigate the effects of using different initial coarse and fine microsphere sizes and the amount and mode of energy input in an effort to optimize the process.

Sol-Gel UO_2 and $(U,Pu)O_2$ Pellet Development (R. L. Hamner, J. M. Robbins)

Pelletized, mixed oxides of plutonium and uranium are currently strong candidate fuels for fast reactors.[6] In the past, these have been prepared from either co-precipitated or mechanically mixed oxides.[7–10] We are investigating an alternate source material for pelletizing: powders derived from sol-gel materials, which are amenable to the recycling of fuels and can be produced as homogeneous mixtures of fissile and fertile materials.

Stradley and Robbins[11] showed that sol-gel $(Th,U)O_2$ powders can be pelletized to densities ranging from 78 to 95% of theoretical. We have extended this technology to the pelletizing of sol-gel UO_2 powders, and we hope to extend it further to the pelletizing of urania-plutonia sol-gel powders.

---

[6] J. H. Kittel, E. L. Zebroski, A. Strasser, L. R. Kelman, W. E. Baily, and J. H. Handwerk, Plutonium Fuel Development for Fast Reactors in the U.S., CONF-661003-13 (October 1966).

[7] C. N. Craig, C. M. Ryer, and M. L. Thompson, Plutonium-Uranium Mixed Oxide Fuel Pellet Fabrication Development for the Southwest Experimental Fast-Oxide Reactor, GEAP-5285 (October 1966).

[8] A. T. Jeffs, R. R. Boucher, and L. R. Norlock, Fabrication of UO_2-PuO_2 and ThO_2-PuO_2 Experimental Fuel, AECL-2675 (February 1967).

[9] K. H. Peuchl, "PuO_2-UO_2 Fabrication," Nucleonics 24(1), 6–7 (January 1966).

[10] N. H. Brett and L. E. Russell, The Sintering Behavior and Stability of $(Pu,U)O_2$ Solid Solutions, AERE-R-3900 (1962).

[11] J. G. Stradley and J. M. Robbins, Metals and Ceramics Div. Ann. Progr. Rept. June 30, 1967, ORNL-4170, pp. 219–220.

In our preliminary studies we worked with sol-gel UO_2 materials, but we expect most of the processing information gained to be applicable to plutonia-bearing materials.

We made powders for pelletizing by grinding dried microspheres or shards to −325 mesh size and by freeze drying a 0.7 M sol. The source materials are described in Table 1.1.

Table 1.1. Description of Sol-Gel Materials Used for Pelletizing

Preparation Variables	Physical Form			
	Gel Spheres	Sol	Gel Shards[a]	Gel Shards[b]
Drying Temperature, °C	185		90–95	90–95
Drying Atmosphere	Ar-H_2O		Argon	Argon
Sol Compositions				
Uranium, M	~ 0.6	0.71	0.71	0.915
U(IV), mole/mole U	0.89	0.89	0.89	0.896
NO_3^-, mole/mole U	~ 0.18	0.183	0.183	0.093
$COOH^-$, mole/mole U	~ 0.3	0.38	0.38	0.41

[a]Crystallite size: 55 A.

[b]Crystallite size: 35 A.

Freeze drying is a common process for commercial preparation of medical products and dehydrated foodstuffs.[12] This generally involves freezing the wet material, placing it under vacuum, and supplying enough heat to sublime the frozen moisture out of the structure without melting it. In our preliminary experiments involving freeze drying, we first poured the sol into a shallow tray to a depth of about 1/2 in. and froze it with liquid nitrogen. We then put the frozen sol into a vacuum desiccator and kept the system under a dynamic vacuum of 25 torrs for drying. From this point, we varied the procedures as follows:

(a) The moisture was evaporated completely from the frozen state in about 4 hr. This resulted in a very fluffy powder which we rejected as

[12]E. W. Flosdorf, Freeze-Drying, Reinhold Publishing Corporation, New York, 1949.

being unsatisfactory for pelletizing because of its poor die-loading properties and its tendency to laminate during forming.

(b) The moisture was evaporated from the material in 3 1/2 hr as it was cycled between freezing and thawing. This produced a somewhat coarser powder, but 70% of it could be vibrated through a 325-mesh sieve; the rest was reduced to this size by light crushing.

(c) The moisture was evaporated as the material was allowed to thaw gradually over a 24-hr period. About 90% of the powder produced could be vibrated through a 325-mesh sieve, and we selected this powder for our sintering experiments.

We processed all of the materials in air except a portion of the shards. We processed some of the powders from shards in argon, but we exposed some of these powders to air before pelletizing for comparison of sintering behavior. During a two-day exposure to air, the oxygen-to-uranium ratio in one batch of powder increased from 2.288 to 2.512 and in the other batch from 2.470 to 2.494. We produced 0.2-in. right-cylindrical pellets from all of the powders and from whole microspheres by a number of fabrication schemes shown in Fig. 1.2. We found in our previous studies[13] that when sol-gel microspheres are sintered in Ar–4% H_2 the presence of steam is necessary to remove carbon during heating to 1000°C, but we had no information as to whether steam treatment was necessary for removal of carbon at higher temperatures. Consequently, we sintered some specimens in dry gas at 1430°C and steam treated others at 1000°C before final sintering in a dry gas at 1430°C. We also reheated some of the pellets to 1600°C to determine whether their densities could be increased.

The history and the densities of the pellets obtained by our various fabrication schemes are shown in Table 1.2. A summary of our observations and results follows.

We had no difficulty in pelletizing the powders or the whole microspheres, and we produced by various fabrication schemes pellets ranging in density from 68.7 to 92.9% of theoretical after sintering at 1430°C.

---

[13]H. Beutler and R. L. Hamner, Metals and Ceramics Div. Ann. Progr. Rept. June 30, 1967, ORNL-4170, pp. 224–226.

ORNL-DWG 67-12991

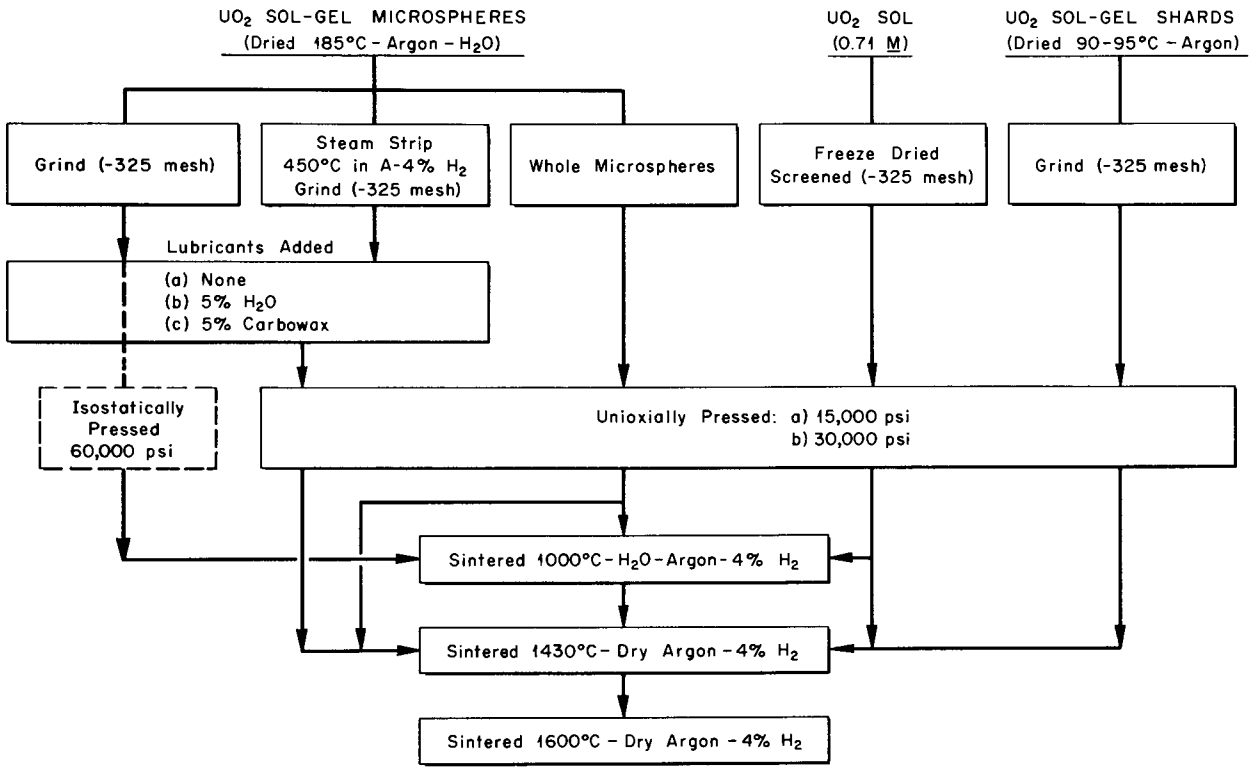

Fig. 1.2. Flowsheet for Fabrication of UO_2 Sol Gel.

[redacted]

Table 1.2. History and Densities of Pelletized UO_2 Sol-Gel Materials

Material Description[a]	Forming Pressure (psi)	Average Sintered Densities[b] % of Theoretical, at Temperature, °C		
		H_2O–Ar–4% H_2	Ar–4% H_2	
		1000	1430	1600
	$\times 10^3$			
Dried sol-gel shards[c] ground (–325 mesh)	40		92.9	
	30		92.6	
	15		86.8	
Dried sol-gel shards[c] ground (–325 mesh); processed in argon	30		89.8	
	15		81.8	84.4
Dried sol-gel shards[d] ground (–325 mesh)	40		92.3	
	30		90.3	
	15		82.5	
Dried sol-gel shards[d] ground (–325 mesh); processed in argon	40		91.5	
	30		88.3	
	15		79.9	80.8
Sol freeze dried to –325 mesh powder	30		e	
	15	78.7	82.2	84.6
As-received microspheres ground to –325 mesh	60[f]	87.5	90.3	
	30	73.5	79.9	82.0
	15	68.1	72.7	
As-received microspheres ground to –325 mesh; Carbowax added	30		77.5	
	15	68.1	71.2	74.9
Microspheres oxidized and reduced at 700°C, ground to –325 mesh	30		75.8	
	15		69.9	
Microspheres oxidized and reduced at 700°C, ground to –325 mesh; water added	30		76.1	
	15		70.4	
Microspheres oxidized and reduced at 700°C, ground to –325 mesh; Carbowax added	30		75.0	
	15		69.1	
Microspheres steam-stripped in Ar–4% H_2 at 450°C, ground to –325 mesh	30	70.0	75.7	77.5
	15	64.9	69.4	72.5
Microspheres steam-stripped in Ar–4% H_2 at 450°C, ground to –325 mesh; Carbowax added	30		73.2	76.4
	15	62.3	67.0	72.4

[redacted]

[redacted]

Table 1.2 (continued)

Material Description[a]	Forming Pressure (psi)	Average Sintered Densities[b] % of Theoretical, at Temperature, °C		
		H_2O–Ar–4% H_2	Ar–4% H_2	
		1000	1430	1600
	$\times 10^3$			
Microspheres steam-stripped in Ar–4% H_2 at 450°C, ground to –325 mesh; water added	30	67.2	76.9	
	15	61.4	70.4	73.2
Whole microspheres	30	71.1	78.7	
	15	63.1	68.7	70.1

[a]All powder processing done in air except where noted otherwise.

[b]Values obtained at more than one temperature were obtained on the same pellets.

[c]Crystallite size: 55 A, oxygen-to-uranium ratio 2.512 (air), 2.288 (argon).

[d]Crystallite size: 35 A, oxygen-to-uranium ratio 2.494 (air), 2.470 (argon).

[e]All pellets cracked.

[f]Isopressed.

[redacted]

[redacted]

We obtained the highest densities from powders derived from the two batches of shards. For each batch of this material, slightly higher densities resulted from the material exposed to air than from the material protected by argon, but densities were not significantly affected by the difference in crystallite sizes of the two batches (55 and 35 A).

Powder obtained by freeze-drying UO_2 sol was less sinterable than the powdered shards but was more sinterable than powdered microspheres. All of the pellets pressed at 30,000 psi from freeze-dried powder, however, cracked during sintering. We have no explanation for the cracking of the pellets, but we are now trying to determine whether calcination of the powders at low temperatures ($\leq$ 200°C) will alleviate this problem. We are also making further studies of freeze-drying to determine what effects the drying conditions have on the powder produced.

Pellets pressed from whole microspheres were almost as dense as those prepared from powdered microspheres after sintering at 1430°C and had the outward appearance of consolidated microspheres stuck together by a porous matrix.

We obtained the lowest densities on pellets derived from microspheres that either had been steam-treated in Ar–4% H_2 at 450°C or oxidized and reduced at 700°C before being ground to a powder.

The densities of pellets sintered in dry Ar–4% H_2 at 1430°C were comparable to those of pellets derived from the same powder and presintered at 1000°C in steam–Ar–4% H_2 before sintering at 1430°C. The steam treatment, however, will probably be necessary to keep the carbon content low; for example, pellets subjected to the steam treatment retained only 50 ppm of carbon, whereas pellets from the same batch of powder sintered in dry gas retained 380 ppm of carbon after a final sintering at 1430°C.

For the same material, sintered densities increased with increase in uniaxial forming pressure, as expected. Isostatic pressing at 60,000 psi, of course, had a strong influence on density, but we prefer to avoid this operation if possible.

Lubricants such as Carbowax or water did not significantly affect the density of pellets pressed at $\leq$ 30,000 psi, but the use of much higher pressures might require the use of a lubricant to prevent laminations.

[redacted]

We have selected powders derived from dried shards and from freeze-dried sols as being the best candidates for further studies of pelletizing; for reference, however, we shall continue to pelletize powdered microspheres. Our immediate plans are to investigate further means of increasing the densities of the candidate materials.

We expect to process plutonia-bearing sol-gel oxide powders in a similar manner in the very near future.

Characterization of Sol-Gel $(U,Pu)O_2$ Fuels

A. R. Olsen

The development of the various sol-gel fuel fabrication processes includes a series of characterization tests to establish the effects of process variations on basic fuel characteristics. In addition to the usual chemical and metallographic evaluations, we are planning to investigate various mechanical and physical properties that influence the irradiation behavior of the resulting fuel bodies.

These tests will be an extension of the work being done on sol-gel thoria-base fuels.[14] They will employ similar techniques and equipment, but under glove box protection. Included in these tests are:

1. thermal conductivity measurements in both comparative axial and radial apparatus with low differential temperatures and radial high differential temperature apparatus,
2. mechanical property measurements of the stress-strain relationships as a function of temperature at both low and high strain rates,
3. thermal shock characterization,
4. adsorbed and absorbed gas determination,
5. compatibility studies.

Pending availability of the equipment required for these characterization studies, we are conducting literature searches to establish the base-line information.

---

[14]A. R. Olsen, J. D. Sease, R. B. Fitts, and A. L. Lotts, Fabrication and Irradiation Testing of Sol-Gel Fuels at Oak Ridge National Laboratory, ORNL-TM-1971 (September 1967).

[redacted]

Thermodynamic Evaluations of the $(U,Pu)O_2$ System (K. E. Spear, J. M. Leitnaker)

Because of the greater experience in working with oxide fuels and the consequent advanced technology, a uranium-plutonium oxide will almost certainly be the fuel choice in near-term fast-breeder reactors. Our present effort on the $(U,Pu)O_2$ system uses available thermodynamic data in helping to understand and predict the compatibility of mixed-oxide fuels with cladding materials. These predictions give limits of behavior and do not include possible kinetic factors, such as the formation of an impermeable oxide layer on the cladding that may drastically reduce the rate of oxidation. However, the thermodynamic predications tell whether or not it is possible for the cladding to be oxidized by the fuel. Details of our present analysis of mixed-oxide fuels will be reported at a later date. A general outline of this work is, however, given below.

We have assumed a closed system with boundaries defined by the fuel cladding; in other words, we have assumed that material does not diffuse through the cladding. This assumption may or may not be a good approximation of reality, depending upon factors such as the nature of cladding material, temperature, the diffusing species, and the atmosphere surrounding the cladding.

We calculated thermodynamic compatibility of fuels of $Pu_xU_{1-x}O_{2\pm y}$ ($x = 0.10 - 0.30$ and $y = 0.15$) with Li, Na, K, Al, Ti, Zr, V, Nb, Ta, Cr, Mo, W, Re, Fe, Co, Ni, Ru, Rh, Pd, and 18/8/1 stainless steel at temperatures between 600 and 1900°C.

Lithium can reduce the oxides of uranium and plutonium to the metals at temperatures of 1000–800°C – for uranium at approximately 1000°C and lower and around 800°C and lower for plutonium. The metals Al, Zr, Ti, and V will reduce the mixed oxides to the state where all of the plutonium is trivalent and the uranium is tetravalent. The corresponding oxide-to-metal ratio is equal to

$$O/M = x(1.50) + (1-x)(2.00) ,$$

where $x = N_{Pu}/(N_{Pu} + N_U)$. The metals Ta, Nb, Na ($t < 1100°C$), Cr, K ($t < 800°C$) and 18/8/1 stainless steel will partially reduce mixed oxides with oxide-to-metal ratio equal to or greater than 2.000.

[redacted]

Hypostoichiometric mixed oxides will not oxidize Mo, W, Fe, Co, Ni, Re, Ru, Rh, or Pd. Graphs showing the relative oxidation potentials of the various metals and fuels are being prepared.

We looked briefly at literature calculations of changes in the oxide-to-metal ratio across fuel pins caused by the existance of large temperature gradients and of changes in overall oxide-to-metal ratio due to burnup of the fuel. An analysis by Rand and Markin[15] indicates that for both hypo- and hyperstoichiometric fuels, the oxide-to-metal ratio will be approximately 2.00 at the cooler temperatures near the cladding and will show the largest deviations from stoichiometry at the hot center of the fuel pin. Their analysis of $(Pu_xU_{1-x})O_{2\pm y}$ fuel burnup indicates an increase in the oxide-to-metal ratio with burnup for initial ratios equal to or less than 2.

The possibility of significant vapor phase transport of plutonium, uranium, and cladding metals by means of gaseous metal oxides was briefly considered. At temperatures of 2000°K and higher, pressures of uranium and plutonium containing gaseous species are about 10^{-7} atm and greater. Such pressures are high enough to cause significant transport of material to the cooler portions of a fuel pin. Fuels with O/M = 2.000 in contact with Mo, W, or Re metals up to about 2000°K will cause only negligible amounts ($P < 10^{-10}$ atm) of gaseous oxides of these latter metals.

Irradiation Testing of Sol-Gel $(U,Pu)O_2$ Fuels

A. R. Olsen

The final evaluation of the sol-gel-derived $(U,Pu)O_2$ fuel will be based upon their irradiation performance. The irradiation testing program includes comparative tests of all the fabrication forms, Sphere-Pac, Vi-Pac, extrusions, and pellets under a variety of irradiation conditions. The program includes both thermal reactor and fast reactor irradiation

[15] M. H. Rand and T. L. Markin, "Some Thermodynamic Aspects of $(U,Pu)O_2$ Solid Solutions and Their Use as Nuclear Fuels," paper presented at the IAEA Symposium on Thermodynamics of Nuclear Materials with Emphasis on Solution Systems, Vienna, Austria, September 4–8, 1967.

tests. Thermal flux irradiations permit the use of instrumented capsules in the achievement of high burnup levels in relatively short periods of time for screening type irradiations. These are being used to supplement the fast-flux irradiations where the fission rate distribution and fuel temperature profiles are more typical of the anticipated LMFBR operating conditions. The development of mathematical models of fuel behavior and the necessary computer programs for doing the manifold calculations are an integral part of the irradiation test program.

Noninstrumented Screening Type Irradiation Tests (A. R. Olsen, R. B. Fitts)

Thermal flux irradiation testing of the sol-gel $(U,Pu)O_2$ fuels in noninstrumented capsules has been initiated recently. The first five capsules using the design shown schematically in Fig. 1.3 were irradiated in the Engineering Test Reactor (ETR). This capsule design permits the testing of four fuel rods simultaneously. Each fuel rod is approximately 7.5 in. long and contains approximately 3 in. of fuel. The design is such that the fuel claddings operate in the temperature range of 400 to 600°C, depending upon the linear heat rating of the fuel. The axial flux variation in the ETR is such that of the four fuel rods in the capsule, two operate at the peak linear heat rating and the other rods at lower values down to approximately one-half the peak. Table 1.3 lists the fuel compositions and test conditions for the first five capsules.

Two of the five capsules in this series were removed after one cycle of ETR operation. Experiments ORNL 43-99 and 43-100 were duplicates, each containing two fuel specimens of sol-gel $(U,Pu)O_2$ and two of $(Th,Pu)O_2$. All rods were fabricated by the Sphere-Pac technique. Table 1.4 lists the fuel composition and other preirradiation parameters for each of the eight rods in the two capsules. Table 1.5 lists some of the sol-gel fuel characteristics. The urania-plutonia fuel was originally prepared for fast reactor irradiation tests to be conducted by Argonne National Laboratory. Since this material was available, we included it in our first two irradiation tests.

Capsule 43-99 failed near the scheduled end of a reactor cycle. The reactor operation prior to the failure included 16 continuous days of full-power operation, a short reactor shutdown caused by reactor

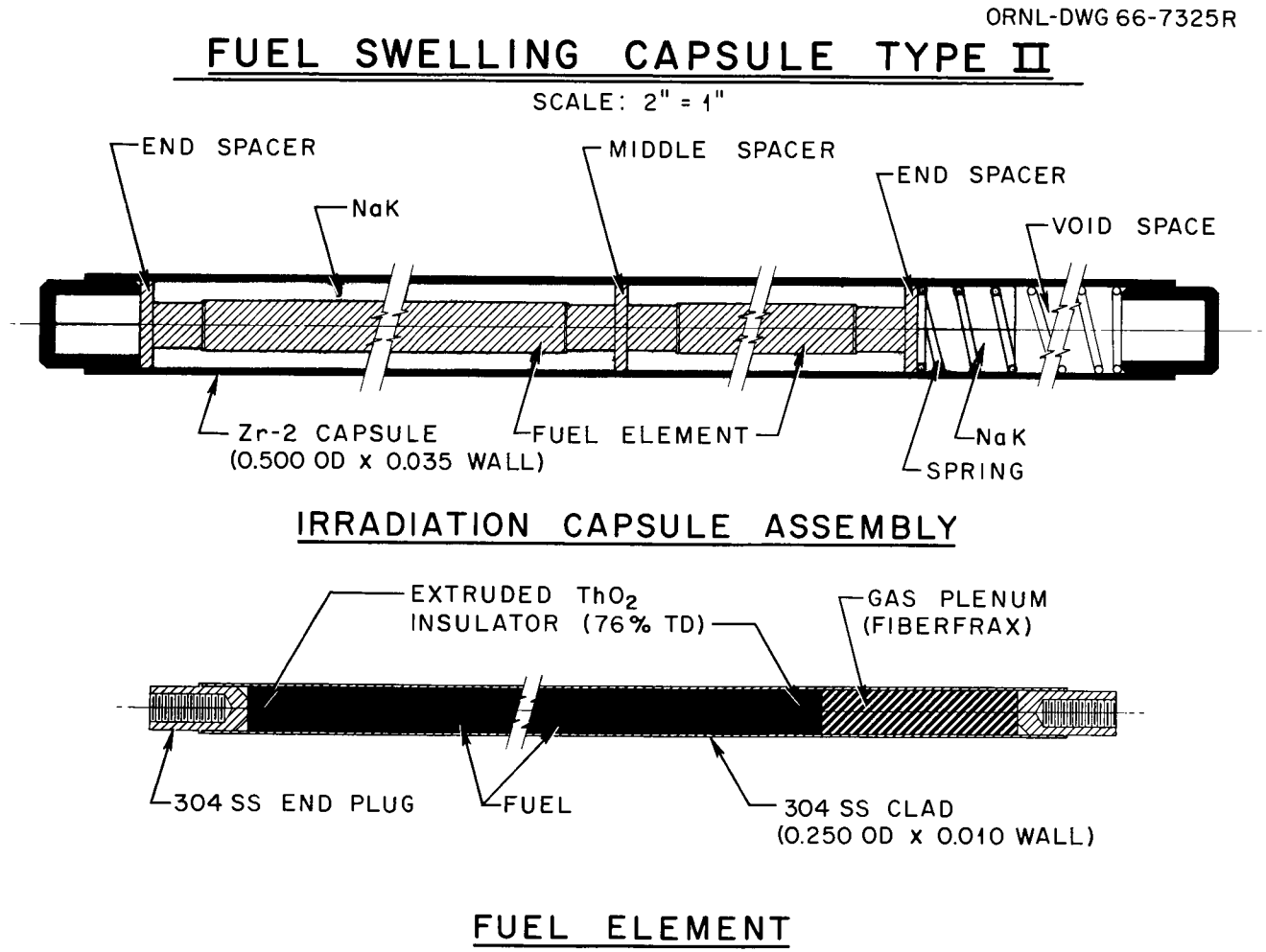

Fig. 1.3. Experimental Test Reactor Irradiation Capsule for Screening Irradiations.

Table 1.3. Noninstrumented Irradiation Screening Tests of Sol-Gel-Derived Urania-Base Bulk Oxide Fuels

Experiment	Fuel		Number of Rods	Peak Target Burnup (% FIMA)	Peak Linear Heat Rating (w/cm)	Test Objective
	Form	Composition				
43-99	Sphere-Pac	(80% ^{235}U, 20% Pu)O_2	2	5[a]	650[a]	Thermal reactor test of fast-reactor test fuel
43-100	Sphere-Pac	(80% ^{235}U, 20% Pu)O_2	2	10[a]	650[a]	Same as 43-99
43-103	Sphere-Pac Pellet	UO_2(20% ^{235}U) UO_2(20% ^{235}U)	3 1	2	540	Test Sphere-Pac fabrication with low-density microspheres
43-112	Sphere-Pac	(85% ^{238}U, 15% Pu)O_2 UO_2(20% ^{235}U)	3 1	0.5	550	Compare mixed-oxide performance with UO_2
43-113	Sphere-Pac	(85% ^{238}U, 15% Pu)O_2	3	10	550	Same as 43-112 with high burnup

[a]These are preirradiation calculated values. Rods failed in reactor from overpowering at a peak burnup of 1.5% FIMA.

[redacted]

Table 1.4. Vibratorily Compacted Fuel Rods for Irradiation Capsules 43-99 and 43-100

Rod Number	Irradiation Capsule and Position[a]	Fuel Material	Fuel Height (in.)	Average Fuel Density[b] (g/cm^3)	Fuel Density Variation[c] (%)
2	43-99-2	(Th–5% Pu)O_2	3.15	8.40	± 2
3	43-99-4	(Th–5% Pu)O_2	3.16	8.38	± 1
4	43-100-2	(Th–5% Pu)O_2	3.13	8.45	± 1
5	43-100-4	(Th–5% Pu)O_2	3.15	8.39	± 1.5
7	43-99-3	(U–20% Pu)O_2	3.14	8.38	± 1
8	43-99-1	(U–20% Pu)O_2	3.13	8.41	± 4
9	43-100-1	(U–20% Pu)O_2	3.14	8.39	± 1
10	43-100-3	(U–20% Pu)O_2	3.13	8.39	± 1

[a]Last number indicates position in capsule numbered from bottom up.

[b]Calculated from height, weight, and inside diameter.

[c]Determined by transmission gamma scan along length of fuel rod.

Table 1.5. Sol-Gel Fuel Characteristics for Capsules 43-99 and 43-100

Material	Sphere Size (μ)	Density (g/cm^3)	Density (% of Theoretical)	Surface Area (m^2/g)	Carbon (ppm)	Gas Release at 1200°C (cm^3/g)
(Th–5% Pu)O_2	420–590	9.84	97.7	0.015	< 10	0.04
(Th–5% Pu)O_2	< 44	NA[a]		0.17	NA[a]	0.24
(U–20% Pu)O_2	420–590[b]	10.54	95.3	0.02	< 10	0.15
(U–20% Pu)O_2	< 44	8.99	81.3	0.03	< 10	0.42

[a]NA – Data not available.

[b]Rod 10 contained a coarse size fraction of 85.5% of 420–590-μ spheres and 14.5% of 290–420-μ spheres.

[redacted]

instrument problems, and a return to full-power operation for 2 hr before the capsule failure. Reactor coolant analysis indicated a loss of the NaK and fission products including some indications of thorium. Since these were the first two capsules of this design, experiment 43-100 was also removed even though there was no evidence of this capsule having failed.

The postirradiation examination of these two capsules is not complete; however, in the preliminary examination it has been found that the $(U,Pu)O_2$ fuel rods located at the peak flux region in both capsules have failed. The cause of failure in the Zircaloy-2 capsule wall of 43-99 has not been determined. The failure of the fuel rods, however, has been clearly identified with an overpower operating condition. The linear heat rating for these rods calculated by the means used for low-enrichment fuels in the past was 650 w/cm. Burnup analyses of the fuel indicate that the actual time average heat rating was greater than 1400 w/cm (approx 50 kw/ft).

The NaK-water reaction in 43-99 has made the postirradiation evaluation of this fuel rod failure very difficult. However, based on the examination of the duplicate fuel rod in 43-100, the following failure sequence is postulated. During the 16 days of continuous full-power operation, the central core of the $(U,Pu)O_2$ fuel was molten and reacted with the center of the 0.250-in.-long, thoria-insulator pellets at each end. During the reactor shutdown, this molten core froze at the bottom of the 3-in. fuel column. The increased heat generation rate at the bottom of the fuel column on the subsequent return to full-power operation increased the molten radius, thus releasing additional fission gas. This gas release caused the expulsion of molten fuel through the central hole in the top thoria insulator. The fuel that was expelled melted a hole through the cladding in the gas-plenum region approximately 1.25 in. above the top of the original fuel column. Since the postirradiation gamma scans indicate essentially no change in the original fuel column height, and metallographic section analyses indicate that 90% of the fuel is still located in the original fuel region, this postulate appears to be the only logical explanation.

Concurrently, with the start of these irradiation tests, we initiated the development of an improved calculational procedure for highly enriched fuels and particularly for plutonium-containing fuels in thermal flux irradiations. The procedure involved the use of an existing code called ANISN.[16] This procedure predicts heat ratings which closely match those derived from the burnup analysis of both the $(U,Pu)O_2$ and $(Th,Pu)O_2$ fuels in experiments 43-99 and 43-100. Consequently, this calculational procedure was used to establish the operating conditions for experiments 43-103, 43-112, and 43-113.

Experiment 43-112 is scheduled to be removed from the reactor early in October after one cycle of operation. This short exposure will provide verification of the operational procedure and preliminary data on the sintering kinetics of $(U,Pu)O_2$ Sphere-Pac fuels at the proposed fast reactor linear heat rating level.

Oak Ridge Research Reactor Instrument Irradiation Tests (R. B. Fitts, V. A. DeCarlo[17])

A series of instrumented capsule irradiation tests is planned to define the effects of fuel composition, fuel stoichiometry, density, fabrication form, and burnup on the in-reactor characteristics of sol-gel-derived urania-plutonia fuels as a function of irradiation temperature. The primary characteristics affected by temperature are thermal conductivity, fuel structural changes, and fission-gas release rate. The data from these instrumented tests will be invaluable in the postirradiation evaluation of the noninstrumented fast-flux irradiation tests.

The design of a capsule for use in the ORR poolside facilities,[18] where the flux level can be adjusted during the irradiation by adjusting the capsule position, has been initiated. The capsule will incorporate a stainless steel-clad fuel rod with a central thermocouple, cladding

---

[16]W. W. Engle, Jr., A Users Manual for ANISN: A One Dimensional, Discrete Ordinates, Transport Code with Anisotropic Scattering, K-1693 (Mar. 30, 1967).

[17]Reactor Division.

[18]D. B. Trauger, Some Major Fuel-Irradiation Test Facilities at the Oak Ridge National Laboratory, ORNL-3574 (April 1964).

thermocouples, and a calorimeter. The central fuel temperature will be maintained constant during any one test at a predetermined level in the 1200 to 2100°C range. The cladding surface temperature will be 600 ± 100°C, and the capsule will be suitable for operation with fuel linear heat ratings up to approximately 20 kw/ft. The design is based on a modification of the experimental gas-cooled reactor capsule. Irradiation of the first capsule is expected to start early in 1968. The initial test will be irradiated for only one ORR cycle to minimize the effects of temperature cycles on microstructural changes. The burnup per cycle will vary, depending upon the fuel linear heat rating up to approximately 2% fissions per initial metal atom.

Transient Testing of Sol-Gel-Derived $(U,Pu)O_2$ Fuels (C. M. Cox)

An important phase in the evaluation of the irradiation characteristics of a fuel involves its behavior under power transient characteristics. Since this behavior will have a marked influence on both safety analysis and fuel element design, we are planning a series of tests to evaluate this transient behavior. The program includes two phases — first, a series of tests to be conducted in the TREAT on sol-gel-derived fuels for comparison of different fabrication forms and comparison with similar tests on other $(U,Pu)O_2$ fuels; and secondly, a series of small capsules to be irradiated in a rabbit facility to investigate the sintering kinetics of the fuel compacts.

A literature survey of transient reactor test results on $(U,Pu)O_2$ fuels is essentially completed, and existing capsule designs of other installations have been requested. As soon as these designs have been reviewed, a letter of intent will be sent to the TREAT operators.

Fast-Flux Irradiation Tests of Sol-Gel $(U,Pu)O_2$ Fuels (A. R. Olsen)

We are presently planning a series of fast-flux irradiation tests. We have contacted the EBR-II operations group and have obtained the necessary design drawings and heat generation information to begin the design of such tests. A test program and preliminary proposal are being prepared for submission to the EBR-II Experiment Review Committee.

Gas-Cooled Fast Reactor Program (C. M. Cox)

A proposal was submitted for a program of irradiation testing to evaluate the performance of sol-gel-derived $(Pu,U)O_2$ fuels and various fabrication techniques under irradiation conditions proposed for gas-cooled fast reactors. The initial phase of the program will concentrate on obtaining compatibility data for a variety of potential cladding materials irradiated at the elevated temperatures typical of gas-cooled reactors. The effects of high external pressure and extended burnup on fuel rod performance will be included in a later portion of the program when the results of the compatibility tests and the results of studies of the free-standing cladding versus the vented fuel pin concepts are available.

[redacted]

2. FUEL ELEMENT FABRICATION DEVELOPMENT

G. M. Adamson, Jr.

Factors affecting plate fabrication and irradiation performance for research reactor fuel plates are being investigated. These studies should lead to the fabrication of plates with increased fuel loadings; permit the use of cheaper fuels; provide assurance that a given fabrication practice will produce satisfactory plates; reduce the development work and lead time necessary for long-range, new-generation fuels; and generate data with which to solve the problems that arise from time to time in the shops of industrial fuel element fabricators. During the recent reporting period we have concentrated on the fabrication of miniature fuel plates to be irradiated in the ETR. Other efforts have been devoted to evaluation of fuel homogeneity in the final plate and to improved ultrasonic nonbond detection.

We have continued at a reduced effort the direct conversion of fissionable halides to refractory fuel compounds by chemical vapor deposition (CVD). The advantage of such a system using the flame reactor concept is the production of submicron-size powders of excellent homogeneity. Not only has the process applicability for production of $(U,Pu)O_2$ fuels but also for processing other compounds to be used for high-temperature bearings and control rods. Presently we are studying the process using the conversion of UF_6 to UO_2, which has direct application to the "Aquafluor" process in fast reactor fuel recycle. A feasibility study on the conversion of PuF_6 to PuO_2 is in progress.

Fabrication of Miniature Fuel Plates to Evaluate Cheaper and Better Fuels

M. M. Martin J. H. Erwin
W. R. Martin

Our present effort has been devoted primarily to examining the feasibility of fuel plates that contain high fuel loadings of two basic types of fuels: U_3O_8 and U_xAl_y. An initial product of these efforts

[redacted]

will be miniature fuel plates to be irradiated in the ETR. Postirradiation examination of these plates will give us significant data on high fuel loadings of HFIR-type U_3O_8, a cheaper type of U_3O_8, U_xAl_y, and a preliminary evaluation of irradiation swelling as a function of fuel particle size.

Table 2.1 presents the chemical and physical properties of the core components prepared for fuel plate manufacture. The "hi-fired" U_3O_8 is identical to the oxide being used in HFIR. The less expensive "burned" U_3O_8 is a prior stage material in the preparation of hi-fired U_3O_8. Its low toluene density of 7.6 g/cm^3 indicates particles of considerable internal voids and/or cracks. To prepare stoichiometric UAl_3 powders, we reacted uranium hydride with high-purity aluminum and then crushed the sintered mass to the desired size fractions. The fines from the crushing operation were then melted by the arc-casting technique, ground, and designated "arc-cast" U_xAl_y. Undoubtedly, the latter material contains some UAl_2, as indicated by the uranium analysis of 75.2% instead of 74.5% for stoichiometric composition. Photomicrographs of the four fuels are shown in Fig. 2.1.

The dimensional requirements for the test plates, as summarized in Table 2.2, were established by Idaho Nuclear Corporation.[1] Two types of miniature plates were designed: an 0.050-in.-thick conventional sample fuel plate and an 0.150-in.-thick instrumented fuel plate. The instrumented plate contains two fuel cores separated with an 0.100-in.-thick aluminum spacer, which provides an inactive portion of the plate in which thermocouples are inserted between the cores. Important dimensions that are identical for the two types of plates are the 5.750 in. length, the 1.250 in. width, the 0.125-in.-wide inactive edge of aluminum, the 0.109-in.-minimum end cladding, and the 0.015-in. cladding thickness.

The general fabrication techniques for the two types of test plates have been reported.[1] The essential steps are (1) weighing and blending the component powder for each fuel core, (2) pressing the fuel compacts, (3) degassing the compacts, (4) assembling the cores into frames and

[1]M. M. Martin, W. J. Werner, and C. F. Leitten, Jr., Fabrication of Aluminum-Base Irradiation Test Plates, ORNL-TM-1377 (February 1966).

Table 2.1. Characterization of Fuel Core Components

	Type of Material and Powder Blend Designation							
	Burned U_3O_8 FA	Hi-Fired U_3O_8 HFA	Arc-Cast U_xAl_y AA	Solid-State Reaction UAl_3 HA	HB	HC	HD	Matrix Aluminum 101 T1
Uranium, wt %	84.51	84.66	75.20	73.70	73.70	73.70	73.70	
^{235}U in uranium, wt %	93.22	93.16	93.15	93.15	93.15	93.15	93.15	
Toluene density, g/cm^3	7.60	8.22	7.10	6.70	ND[b]	6.70	ND[b]	2.696
Surface area,[a] m^2/g	0.35	0.04	0.11	0.08	ND[b]	0.10	ND[b]	0.22
Sieve analysis, wt %								
−140 +170 mesh	11.1			100.0				
−170 +200 mesh	24.5	24.2	22.5		33.3		22.5	
−200 +230 mesh	18.7	24.2	22.5		33.3		22.5	0.1
−230 +270 mesh	24.5	24.2	22.5		33.3	50.0	22.5	1.5
−270 +325 mesh	18.2	24.2	22.5			50.0	22.5	8.6
−325 +dust	3.0	3.1	10.0				10.0	89.8

[a]Static krypton BET determination.

[b]Not determined.

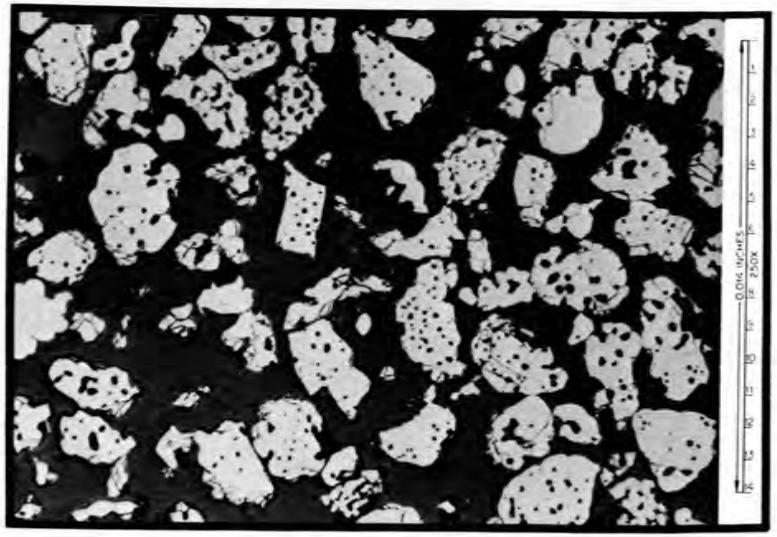

TYPICAL "DEAD BURNED" U_3O_8 PRODUCED AT Y-12 FOR HFIR

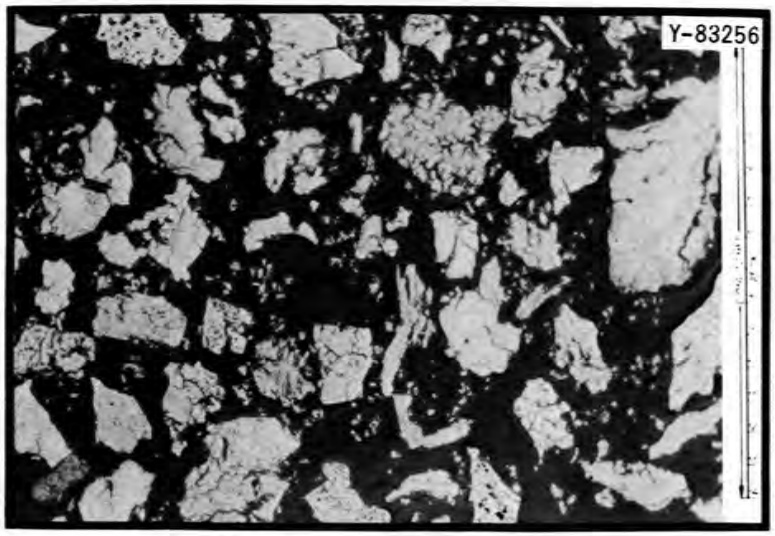

U_3O_8 FORMED BY BURNING URANIUM TURNINGS

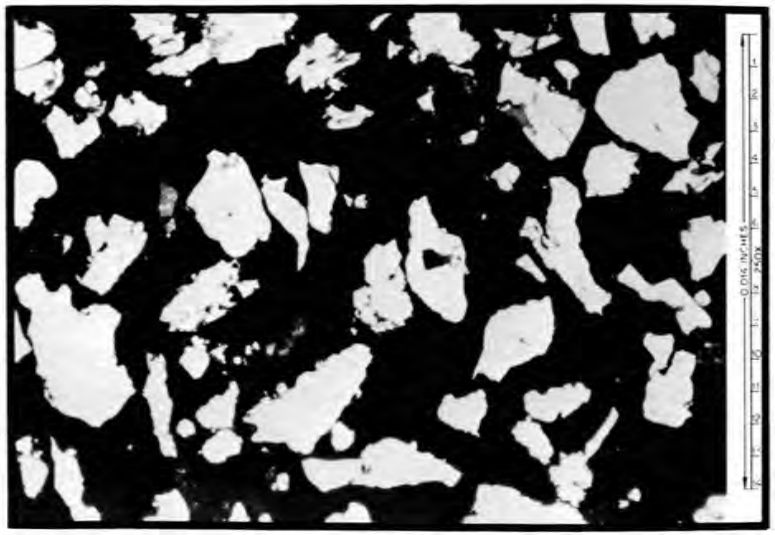

UAl_3 PRODUCED BY ARC MELTING

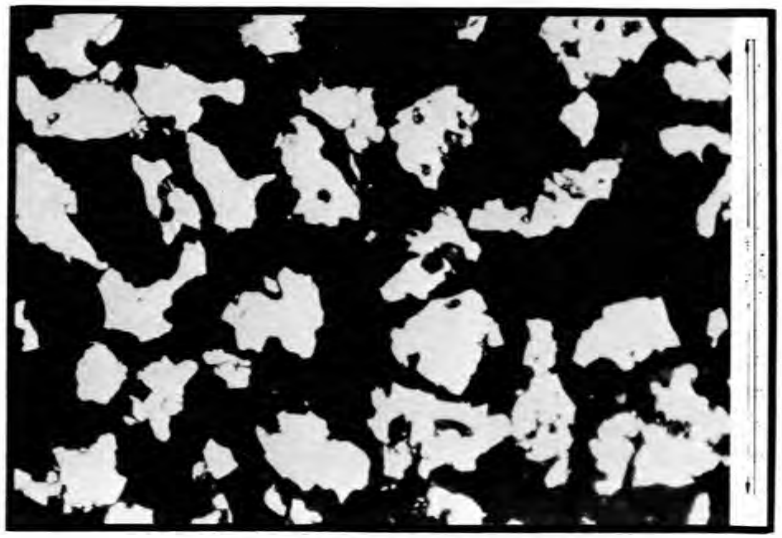

UAl_3 PRODUCED BY ORNL HYDRIDING PROCESS

Fig. 2.1. Typical Photomicrographs of the Four Types of Fuel.

[redacted]

Table 2.2. Summary of Pertinent Design Data

	Miniature Plates	
	Uninstrumented	Instrumented
Dimensions, in.		
Plate length	5.750±0.003	5.750±0.003
Plate width	1.250±0.003	1.250±0.003
Fuel core length	5.469±0.062	5.250±0.250
Fuel core width	1.000±0.031	1.000±0.031
Cladding thickness	0.015±0.003	0.015±0.003
Spacer thickness		0.100
Fuel core thickness	0.020±0.003	0.010±0.002
Total plate thickness	0.050±0.003	0.150±0.003
Materials[a]		
Cladding		
Type of aluminum	6061	6061
Frame		
Type of aluminum	6061	6061
Fuel core		
Number of cores per fuel plate	1	2
^{235}U content per fuel plate, g	2.205±0.022 2.756±0.028	2.205±0.022 2.756±0.028
Fissile compounds	U_3O_8, UAl_3	U_3O_8, UAl_3
Aluminum matrix	101	101

[a]No Alclad material is used.

welding the billets, (5) cladding by roll bonding, (6) annealing to soften and also test for blistering, (7) cold rolling to specified thickness, (8) heat treating to the "O" temper, (9) marking and shearing the plate to finished length and width dimensions, and (10) inspecting and final cleaning. Recent developments have eliminated the need for Alclad cover plate and frame materials.[2] We have also modified the fabrication of the instrumented plates. Our technique, which is cheaper and less time-consuming, employs a five-layer billet (cover plate/cored frame/spacer/cored frame/cover plate) cross section that is evacuated prior to roll bonding.

[2]J. H. Erwin, Metals and Ceramics Div. Ann. Progr. Rept. June 30, 1967, ORNL-4170, pp. 179–181.

[redacted]

[redacted]

The irradiation performance of aluminum-base dispersion-type fuel plates is believed to depend somewhat upon the amount of void volume initially present in the cladding core. The void concentrations of the various fuel compacts prepared for the irradiation study are listed in Tables 2.3, 2.4, and 2.5. Figure 2.2 summarizes these data for the sample fuel compacts. We note from Fig. 2.2 that the two dispersions that contained the cheaper fuels of burned U_3O_8 and arc-cast UAl_3 grew more during degassing at 500°C than hi-fired U_3O_8 and solid-state reacted UAl_3. Obviously, all four fuel compounds are chemically incompatible with aluminum and reacted to various degrees to form lower density products. This swelling presents problems in billet assembly but can be accommodated if reproducible. On the other hand, it may also generate additional fabrication voids in the rolled plates. We reported earlier[3]

[3] M. M. Martin, Metals and Ceramics Div. Ann. Progr. Rept. June 30, 1967, ORNL-4170, pp. 177–179.

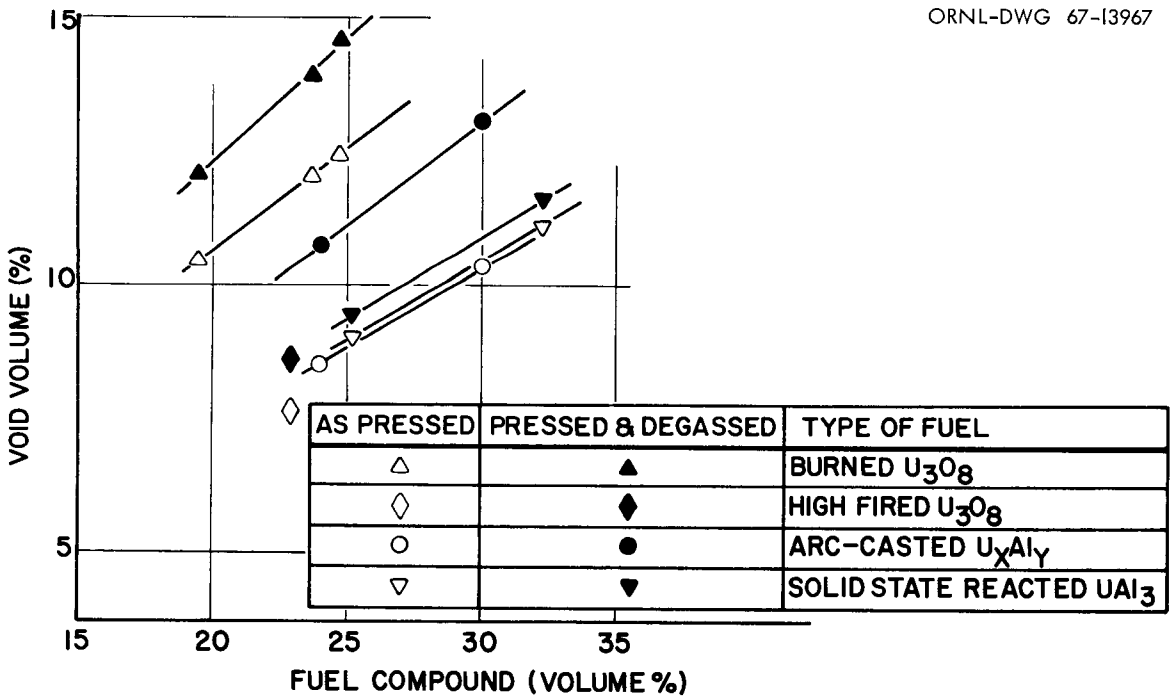

Fig. 2.2. Effect of Fuel Compound Concentration on Void Volume.

[redacted]

Table 2.3. Void Concentration of U_3O_8-Bearing Fuel Dispersions for Sample Test Plates[a]

Compact Identification Number	Fissile Compound Concentration, %		Theoretical Density (g/cm^3)	Void Concentration, vol %, of Compact	
	By Weight	By Volume[b]		Pressed	Degassed
			Burned U_3O_8 – FA		
860-1	43.79	19.3	3.7578	10.70	12.19
869-1	44.80	20.0	3.7933	10.46	12.23
869-2	44.80	20.0	3.7933	10.38	12.21
863-1	51.05	23.7	4.0203	12.03	13.96
870-1	52.83	25.0	4.0920	12.28	14.35
870-2	52.83	24.5	4.0920	12.74	14.81
			Hi-Fired U_3O_8 – HFA		
878-1	50.16	22.9	4.0668	7.74	8.94
878-2	50.16	23.0	4.0668	7.61	8.59
878-3	50.16	22.9	4.0668	7.69	8.33
878-4	50.16	23.0	4.0668	7.38	8.50
878-5	50.16	22.9	4.0668	7.72	8.55
878-6	50.16	23.0	4.0668	7.58	8.55
878-7	50.16	22.9	4.0668	7.67	8.47

[a]See Table 2.1 for characterization of fuel.

[b]Values apply only to pressed compacts.

Table 2.4. Void Concentration for Type UAl_3-Bearing Fuel Dispersions for Sample Test Plates[a]

Compact Identification Number	Fissile Compound Concentration, %		Theoretical Density (g/cm^3)	Void Concentration, vol %, of Compact	
	By Weight	By Volume		Pressed	Degassed
			UAl_3 – AA		
861-1	48.73	24.1	3.8654	8.92	12.03
871-1	48.60	24.1	3.8607	8.43	10.11
871-2	48.60	24.1	3.8607	8.36	10.14
864-1	56.94	29.8	4.1701	10.59	13.66
872-1	57.35	30.3	4.1866	10.22	12.77
872-2	57.35	30.3	4.1866	10.21	12.86
			UAl_3 – HD		
862-1	48.64	25.2	3.8010	8.83	9.35
862-2	48.64	25.1	3.8010	9.12	9.48
865	58.46	33.0	4.1436	8.33	8.76
873-1	57.42	31.2	4.1046	11.18	11.52
873-2	57.42	31.2	4.1046	11.18	11.43
			UAl_3 – HC		
866	58.46	32.0	4.1436	11.43	11.92
874-1	58.86	32.3	4.1588	11.71	11.91
874-2	58.86	32.2	4.1588	11.88	12.55
			UAl_3 – HB		
867	58.46	32.0	4.1436	11.32	11.75
875-1	58.85	32.4	4.1585	11.31	11.58
875-2	58.85	32.5	4.1585	10.96	11.54
			UAl_3 – HA		
868-1	58.85	32.4	4.1585	11.25	11.76

[a]See Table 2.1 for characterization of fuel.

[b]Values apply only to pressed compact.

Table 2.5. Void Concentration of Fuel Dispersions for Instrumented Test Plates[a]

Compact Identification Number	Fissile Compound Concentration, %		Theoretical Density (g/cm^3)	Void Concentration, vol %, of Compact	
	By Weight	By Volume[b]		Pressed	Degassed
			U_3O_8 – HFA		
857-1	42.44	18.2	3.7717	6.76	7.68
857-2	42.44	18.2	3.7717	6.56	7.06
876-1	42.90	18.4	3.7880	6.86	7.36
876-2	42.90	18.5	3.7880	6.76	7.53
876-3	42.90	18.4	3.7880	6.76	7.68
876-4	42.90	18.4	3.7880	6.95	8.25
876-5	42.90	18.4	3.7880	7.09	7.99
876-6	42.90	18.3	3.7880	7.43	8.01
858-1	50.33	23.2	4.0739	6.64	7.73
858-2	50.33	22.8	4.0739	8.83	9.65
877-1	50.36	22.8	4.0752	8.61	9.57
877-2	50.36	22.9	4.0752	8.41	9.37
877-3	50.36	23.1	4.0752	7.67	9.35
877-4	50.36	22.8	4.0752	8.73	9.95
877-5	50.36	22.8	4.0752	8.78	9.86
877-6	50.36	22.8	4.0752	8.50	9.02
			UAl_3 – HD		
859-1	57.56	31.1	4.1095	11.71	12.11
859-2	57.56	31.2	4.1095	11.18	11.47
859-3	57.56	31.2	4.1095	11.28	11.78
859-4	57.56	31.3	4.1095	11.26	11.66
			UAl_3 – HJ		
879-1	58.74	32.2	4.1542	11.59	12.18
879-2	58.74	32.2	4.1542	11.58	12.00
879-3	58.74	32.2	4.1542	11.27	11.79
879-4	58.74	32.3	4.1542	11.23	11.95

[a]See Table 2.1 for characterization of fuel.

[b]Values apply only to pressed compacts.

that the void volume in the final rolled plate can be altered significantly by the type of fuel in the compact.

Presently we have rolled many plates, each of which is being evaluated for dimensional control, fuel homogeneity, and final density. After this evaluation is completed, 12 plates representing the specifications given in Table 2.6 will be transferred to be irradiated in the ETR. A more complete evaluation of the plates in the unirradiated condition will be given in the next reporting period.

Reduction of Swelling in U_xAl_y Compacts by Alloying (J. T. Venard)

One of the problems associated with the use of the U_xAl_y intermetallics as a fuel is the swelling of UAl_3-Al fuel compacts during vacuum degassing. The results of Gregg, Crouse, and Werner[4] suggest that alloy additions that suppress the UAl_3-to-UAl_4 transformation would limit compact swelling. Thurber and Beaver reported[5] some years ago that Picklesimer suggested additions of Si, Zr, Ge, or Sn to suppress the transformation. Thurber and Beaver confirmed that silicon additions to UAl_3 could stabilize the compound during fabrication. We have initiated a program that will further investigate both the swelling behavior during degassing and the workability of these compounds. The mechanical behavior of the fuel will be an important parameter governing the distribution of fuel in the rolled plate. Therefore, the hot hardness of UAl_aX_b-Al compacts will be examined over the temperature range from 20 to 600°C. The suppressant, X, will vary over the range 0 to 10 at. %.

Preparation of the UAl_aX_b pellets begins with master alloy buttons of uranium or UX_b which are hydrided. The hydrided master alloys are blended with aluminum powder, pressed, and sintered. The resultant UAl_aX_b alloy pellets will be studied to determine their swelling and hot-hardness characteristics.

---

[4]J. L. Gregg, R. S. Crouse, and W. J. Werner, Swelling of UAl_3-Al Compacts, ORNL-4056 (January 1967).

[5]W. C. Thurber and R. J. Beaver, Development of Silicon-Modified 48 wt % U-Al Alloys for Aluminum Plate-Type Fuel Elements, ORNL-2602 (March 9, 1959).

Table 2.6. Miniature Test Plates for ETR G-12 Loop Irradiations

Tier in G-12 Loop	Reference Plate Number	Type Designation	Method of Fuel Fabrication	Maximum Size (μ)	Fines <44 μ (wt %)	Uranium Loading (g/plate)	Expected Fissions/cm^3 for 600-hr Irradiation	Nominal Heat Flux (Btu hr^{-1} ft^{-2})
							$\times 10^{21}$	$\times 10^{6}$
5	1	U_3O_8	Burning	88	3.0	2.205	1.4	1.5
	2[a]	U_3O_8	Hi-firing	88	3.1	2.205		
	3	U_xAl_y	Arc casting	88	10.0	2.205		
	4	UAl_3	Solid-state reaction	88	10.0	2.205		
1	5	U_3O_8	Burning	88	3.0	2.756	1.0	1.0
	6[a]	U_3O_8	Hi-firing	88	3.1	2.756		
	7	U_xAl_y	Arc casting	88	10.0	2.756		
	8	UAl_3	Solid-state reaction	88	10.0	2.756		
3	9[a]	UAl_3	Solid-state reaction	88	10.0	2.756	2.1	2.3
	10	UAl_3	Solid-state reaction	63	None	2.756		
	11	UAl_3	Solid-state reaction	88	None	2.756		
	12	UAl_3	Solid-state reaction	105	None	2.756		

[a]Instrumented test plate.

The master alloys containing Ge, Sn, and Zr have been successfully hydrided and crushed. These alloys are being pressed and sintered into pellets. The master alloy containing 12.4 wt % Si did not hydride, so melt orders were written to prepare a series of uranium-silicon alloys ranging from 5 to 12 wt % Si. These buttons were hydrided and the results show that about 9 wt % Si in uranium is the maximum that will hydride to a fine powder.

Evaluation of Fuel Homogeneity in Blends, Compacts, and Rolled Plates
(B. E. Foster, S. D. Snyder, W. R. Martin)

The "pilot" model x-ray attenuation homogeneity scanner that was used for the early HFIR fuel plate inspection became available for our use in fuel materials homogeneity studies. We are presently making a few modifications for added versatility so that the equipment can be used to study the homogeneity of powder blends and fuel compacts as well as finished experimental fuel plates. This machine has been located in the Powder Metallurgy Laboratory.

We have recently completed the scanning of 20 experimental fuel plates. Each plate has the same dimensions as the present HFIR design. Six of these plates have HFIR outer annulus fuel contours, six have HFIR inner annulus fuel contours, and the remaining eight are flat-core ATR type plates. For each of the HFIR contours there are two plates with U_3O_8-Al cores, two plates with UAl_3 intermetallic cores, and two plates with $UAl_3Si_{0.4}$ cores. In each of the core materials, one plate contains the nominal HFIR uranium loading and the other contains a 25% increased uranium loading. The ATR type flat-core plates are all U_3O_8-Al cores, six nominal and two 25% increased uranium loading.

The 12 plates with HFIR-contoured cores were made to allow calibration of the x-ray attenuation scanning technique for the new materials and higher loadings. The eight plates with flat cores are being used for studies to determine capabilities and limitations of radiography for the determination of fuel inhomogeneity.

In addition to the complete scanning of these plates, specific 0.078- × 2-in. sections in all the HFIR type plates were scanned for calibration of both x-ray scanning and radiographic techniques. These

sections were subsequently machined from the plates and are being processed for density determinations and later uranium content by analytical chemistry methods.

The higher uranium loaded plates attenuated the 50 kvcp x-ray beam to levels beyond our prior calibration so we determined the new conditions for correlation of uranium content versus attenuation. A change to 55 kvcp with adjustments to the system electronics was adequate for a return to recorder "on-scale" operation. The final results of this work will be uranium content versus attenuation calibrations for plates with U_3O_8-Al, UAl_3, and $UAl_3Si_{0.4}$ cores and with uranium loadings of approximately 31, 37, 43, and 50 weight percentages.

High-contrast radiographs were also made on each of the plates so that densitometric studies can be made using the analytical chemistry data above. Quantitative evaluation can then be made on the radiographic techniques for determination of fuel homogeneity.

We have very recently scanned seven miniature flat-core irradiation test plates prior to their exposure to neutron bombardment. No homogeneity evaluation can be made until we have determined the new calibrations previously mentioned.

Ultrasonic Nonbond Detection in Experimental Fuel Plates (K. V. Cook)

The HFIR-core fuel plates and miniature irradiation test plates described above were evaluated by the through-transmission ultrasonic technique to determine the bond quality and to ascertain whether the reference standards used for the inspection of HFIR fuel plates were valid for the plates containing new materials and higher loadings. We found that nine of the fuel plates and four of the miniature specimens would be considered acceptable when compared to the response from the 1/16-in.-diam reference hole in the HFIR nonbond standard. Three of the HFIR outer annulus plates (HC-2050, -2051, and -2053) and three of the miniature plates (0-3-875, -876, and -880) were not acceptable when compared to the old HFIR standard. At this stage we do not know whether the six questionable plates contain poor quality bonds or whether the attenuation characteristics of the new materials are sufficiently

different to demand the establishment of new reference standards. Further investigation is needed.

Investigation of Surface Films on Aluminum Fuel Plates (J. V. Cathcart)

The buildup of thick oxide layers on the surface of aluminum fuel elements during a fuel element cycle is of concern. These corrosion products, which are principally Boehmite, can interfere seriously with the removal of heat from a fuel element. Large thermal gradients develop across the corrosion layer, resulting in higher fuel plate temperatures, which will eventually govern the lifetime of fuel plates if the fuel loading is increased. In this area, the thickness of the oxide and its thermal conductivity are important.

Previous efforts at solving this problem for relatively high-temperature research reactors involved the selection of the more corrosion resistant alloys, X8001 and 6061, or the application of a metallic coating such as nickel to the fuel element surfaces. However, in a reactor such as the HFIR, substantial corrosion problems still remain, and the metallic coatings tend to spall off during high heat flux conditions.

We believe that the best hope for overcoming these difficulties lies in developing a more adherent anti-corrosion coating for the fuel elements. One method, suggested by some of our previous oxidation studies, involves the formation of an anodic film on the aluminum surfaces. Anodic films on aluminum develop a variety of film morphologies and structures depending on the anodizing bath used. By choosing conditions that lead to the incorporation of bath constituents in the films, it is even possible to generate an "alloy" oxide film. It is hoped that the selection of the correct combination of factors will lead to the formation of anodic films whose transformation to Boehmite will be either retarded or prevented. It is also possible that the thermal conductivity of such films will be larger than that of Boehmite.

Initial results of isothermal tests of anodic coatings on high-purity aluminum have been promising. For example, in a 100-hr test at 200°C, no attack was observed on a 99.999% Al specimen which had been anodized in an oxalic acid solution. An unanodized specimen was completely converted to oxide in a similar test.

Conversion of UF_6 to UO_2 with a Flame Reactor

J. I. Federer

Operation of the flame reactor and characterization of the product have continued. In the flame reactor, hydrogen, oxygen, and metal fluoride react in the high-temperature flame generated by combination of hydrogen and fluorine to produce metal oxides and other compounds in the form of powder. This device has the capability of experimentally producing submicron-size powder of many compounds of interest to the nuclear industry. Presently we are using the device to convert UF_6 to UO_2. The powder product is being characterized in both the as-prepared and annealed conditions by x-ray diffraction for phase identification, chemical analysis, electron microscopy for particle size determination, and fabricability. Modifications have been made to the flame reactor system to improve safety of operation and efficiency of powder collection. The flame reactor is shown schematically in Fig. 2.3.

Experiments have been conducted at the conditions shown in Table 2.7 in search of a single-phase UO_2 product. The principal variation in these conditions was the volumetric oxygen-to-UF_6 ratio, which ranged from about 1 to 16. In addition, WF_6 was added to the reacting gases in experiment 6 in order to obtain a tungsten-bearing UO_2 powder. The results of x-ray and chemical analyses are shown in Table 2.8. Uranium dioxide was a major constituent in the product of every experiment.

Several batches of powder were annealed at 1000°C in flowing hydrogen for 16 hr. Annealing caused the powders to change color from gray or black to reddish-brown and also produced the results shown in Table 2.9. The oxygen-to-uranium ratios after annealing ranged from 2.0031 to 2.1247, and the fluorine content was reduced to less than 10 ppm. Uranium dioxide was the only phase revealed by x-ray diffraction except for small amounts of other phases in the powder from experiments 1 and 6.

The high fluorine content of the as-deposited material must be absorbed as HF or fluorine, since the amount is greatly reduced by annealing at 1000°C in hydrogen. Of course, if all of the fluorine were

[redacted]

ORNL-DWG 67-10621

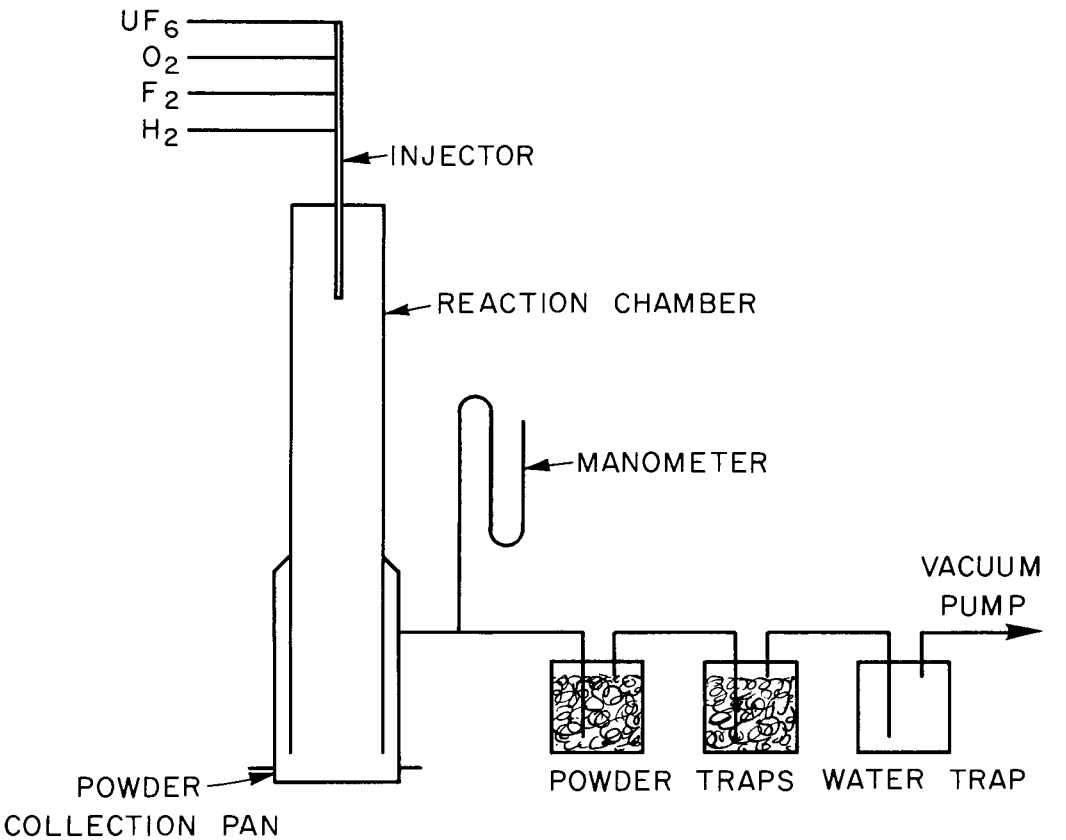

Fig. 2.3. Schematic Drawing of Flame Reactor Used to Convert UF_6 to UO_2.

Table 2.7. Deposition Conditions[a]

Experiment Number	Gas Flow Rates, cm^3/min			
	H_2	F_2	O_2	UF_6
1	2500	600	500	50
2	3600	670	1000	100
3	3600	670	700	100
4	3000	670	200	100
5	3000	670	150	125
6	3000	670	150	125[b]
7	2500	600	500	50
8	3600	670	200	100
9	3600	670	440	100
10	2500	600	500	50
11	3600	670	1600	100

[a]Flame temperature estimated to be greater than 2000°C, pressure 3 to 10 torr.

[b]WF_6 added at a flow rate of 12 cm^3/min.

[redacted]

[redacted]

Table 2.8. Results of Deposition Experiments

Experiment Number	Chemical Analysis, wt %				X-Ray Analysis[a]			
	U	F	OH^-	O	UO_2	U_3O_8	UF_4	Other[b]
1[c]	d				M	S	NF	W
1	d				S	M	NF	W
2[c]	d				S	S	NF	NF
3[c]	75.7	10.00	12.56	1.74	S	S	W	NF
3	81.0	4.65	6.32	8.02	S	M	W	NF
4[c]	75.9	9.78	11.75	2.58	M	S	NF	NF
4	82.4	10.70	0.00	8.74	S	M	W	NF
5[c]	d				S	S	W	NF
5	70.1	11.92	17.90	0.00	NF	NF	NF	S
6[c,e]	69.3	11.68	13.82	0.00	S	S	W	NF
6[f]	d				S	S	W	S
7[c]	77.6	6.50	13.07	2.85	S	NF	NF	W
7	77.0	6.32	14.06	2.67	S	NF	NF	NF
8[c]	68.8	9.26	17.03	0.00	W	NF	NF	S
8	73.9	11.51	13.16	1.47	S	NF	NF	M
9	79.6	5.08	9.59	5.69	S	NF	NF	W

[a]Amount of phase estimated from intensities of lines on x-ray powder patterns. S — strong, M — medium, W — weak, NF — sought, not found.

[b]Unidentified compounds.

[c]Sample from wall of reaction chamber; all others from dry traps.

[d]Analyses not obtained.

[e]3.8 wt % W.

[f]4.8 wt % W.

[redacted]

Table 2.9. Chemical and X-Ray Analysis of Powder[a] Annealed in Hydrogen at 1000°C for 16 hr

Experiment Number	Chemical Analysis		X-Ray Analysis[b]		
	Oxygen-to-Uranium Ratio	F (ppm)	UO_2	U_3O_8	Other
1	2.0317	< 5	S	NF	W[c]
2	2.0239	< 5	S	NF	NF
3	2.0935	< 10	S	NF	NF
4	2.0292	< 10	S	NF	NF
5	2.0031	< 5	S	NF	NF
6	2.1247	< 10	S	W	W[d]

[a]All samples from dry traps.

[b]Amount of phase estimated from intensities of lines on x-ray powder patterns. S — strong, W — weak, NF — sought, not found.

[c]Unidentified compound.

[d]Tungsten metal.

present as fluorides or oxyfluorides, the x-ray diffraction patterns would indicate these as major phases. The x-ray results, however, indicated that contaminants of the as-prepared powder were present in small quanitites. The material from several experiments showed only UO_2 lines in the diffraction patterns even though the fluorine content was high. The UF_4 identified in some as-deposited material possibly was converted to an oxyfluoride during the hydrogen anneal by reaction with H_2O from decomposition of $U(OH)_4$, then reduced to UO_2. Uranium tetrafluoride is neither reduced by hydrogen nor sublimed at 1000°C.

To improve the powder collection process, an electrostatic precipitator has been installed in the bottom of the reaction chamber. We have also begun a formal economic evaluation of the flame reactor processes, and these results will be discussed in the next reporting period.

[redacted]

Preparation of PuO_2 Powder from PuF_6 by Chemical Vapor Deposition

W. C. Robinson, Jr.

The assembly of the apparatus inside the glove boxes has finally been completed. Verbal premission to operate "cold" using UF_6 as a substitute for PuF_6 has been obtained after modifications to the apparatus. Sodium fluoride-activated aluminum traps have been installed on the outlets to the boxes on the recommendation of the Health Physics Division. This was accomplished and the overall system was helium leak checked by the building crafts.

The initial experimental heatup revealed that the cooling line on the injector assembly had been ruptured during setup. Further investigation revealed a stoppage in the fluorine line between the internal fluorine tank and the PuF_4 fluorination chamber. The injector has been repaired. The fluorine line will be repaired when the glass is removed from the alpha box.

This feasibility study will be completed within the next reporting period.

[redacted]

[redacted]

3. MIXED NITRIDE FUELS DEVELOPMENT

J. L. Scott

Mixed (U,Pu)N offers promise as fuel for advanced liquid-metal-cooled fast breeder reactors. Its major attributes are its high metal density (13.5 g/cm^3), which is about 30% greater than that of mixed oxide; its good thermal conductance; and its stability at high temperatures. In comparison with mixed carbides, which have similar attributes, mixed nitrides offer greater ease of control of stoichiometry and, probably, superior strength at high temperatures (since the melting point is higher). Perhaps the optimum fuel is not carbide or nitride but rather a solid solution of the two, but information must first be obtained on the terminal compounds.

Major problems associated with mixed nitrides are these:

1. lack of low-cost fabrication methods, particularly from a fuel-cycle standpoint,
2. lack of data on basic properties and the effects of impurities on these properties,
3. lack of information on compatibility with potential cladding materials,
4. lack of irradiation test data,
5. helium and boron production from (n,α) reactions in a fast-neutron flux.

The purpose of our program is to provide the needed information as soon as possible. Although we can produce nitrides from sol-gel feed, we have decided to postpone their use and to concentrate now on studies of basic properties and compatibility, using high-purity material produced from metallic uranium and plutonium. We plan to control carefully the nitrogen pressure over materials when making property measurements or compatibility tests, because such tests with undefined nitrogen activity in the (U,Pu)N are often misleading. Irradiation tests, including assessment of the (n,α) problem, are being deferred for lack of funds.

[redacted]

The existing facility described in the preceding chapter is being converted for the sol-gel mixed-oxide and mixed-nitride studies. Until the facility is ready, we will continue to measure properties of UN and U(C,N) and analyze literature data on mixed nitrides.

Fabrication of Mixed Nitrides

J. Y. Chang E. S. Bomar

We surveyed the literature related to the synthesis, fabrication, and properties of PuN and (U,Pu)N. Several of the more important points are given below.

Synthesis

There are two approaches to the preparation of PuN from metal. The first method[1,2] is direct reaction of plutonium during arc melting under nitrogen. The second method is hydriding the plutonium either partially[3–5] to $PuH_{0.036}$ or to a higher[3,4,6,7] hydrogen content, such as $PuH_{2.7}$, and then nitriding it.

There are also two approaches[2] to the preparation of (U,Pu)N solid solution using powders as the starting material: uranium nitride and

---

[1]D. F. Carroll, "PuN and the Refractory Nitrides," pp. 30–33 in A Seminar on Groups V and VI Anions held at Argonne National Laboratory February 26 and 27, 1964, ANL-6856 (March 1964).

[2]W. M. Pardue et al., Synthesis, Fabrication, and Chemical Reactivity of Plutonium Mononitride, BMI-1693, pp. 5–7 (Sept. 15, 1964).

[3]J. A. Leary et al., "Preparation and Properties of Plutonium Mononitride and Uranium Mononitride–Plutonium Mononitride Solid Solutions," paper presented at the American Ceramic Society Meeting in Portland, Oregon, October 26–29, 1966.

[4]J. A. Leary and R. L. Nance, Method of Preparing Plutonium Mononitride (to U.S. Atomic Energy Commission). U.S. Patent 3,279,898 Oct. 18, 1966.

[5]F. Anselin, Preparation and Study of the Nitrides and Mixed Carbide-Nitride of Uranium and Plutonium, CEA-R-2988 (June 1966); see translation by G. L. Boiswert, ORNL-tr-1722, p. 50.

[6]W. M. Olson, and R.N.R. Mulford, J. Phys. Chem. 68(5), 1048–1051 (1964).

[7]F. Brown, M. Ockenden, and G. A. Welch, J. Chem. Soc. 1955, 4196–4201.

plutonium nitride powders can be synthesized separately from the pure metals and then blended and sintered to high density and homogeneity, or an alloy of uranium and plutonium can be prepared, reduced to a powder, and then nitrided. Separate preparation of uranium and plutonium nitrides may utilize the conditions best suited for hydriding and nitriding either uranium or plutonium. This greater flexibility in choosing the nitriding conditions allows the preparation of fine powder and avoids having to change the nitriding conditions for different uranium-plutonium alloys.

Thermal cycling of plutonium metal before hydriding improved response to the hydriding treatment.[2]

Powder Consolidation

A green density of approximately 70% was obtained on cold pressing at 60 tsi (U,Pu)N powder, 70% of which was particles less than 8 μ in size.[8]

Mixed nitride powder with a particle size of about 270 mesh seems not to sinter appreciably at 1500 to 1600°C, and UAl_2 and U_3Si_2 were unsuccessful as sintering aids for mixed nitride.[9] Fine nitride powder ball-milled for more than 100 hr to obtain 70% of the material less than 8 μ sintered to 90 to 95% of theoretical density,[8] depending on pressing in the range 40 to 80 tsi, sintering temperature 1600 to 1900°C, and sintering time 1 to 4 hr. A density greater than 95% of theoretical was obtained by uniaxial hot pressing at 5 tsi at approximately 1500°C for 3 hr for uranium mononitride[10] or 10 tsi at 1850°C for 5 min for mixed nitride.[11]

---

[8]M. W. Sharpe et al., Quarterly Status Report October 1–December 30, 1966, Advanced Plutonium Fuels Program, LA-3650-MS 807-2–807-16.

[9]M. U. Goodyear et al., Progress Relating to Civilian Applications During October through December 1966, BMI-1791, pp. A-1–A-3.

[10]E. O. Spiedel and D. L. Keller, Fabrication and Properties of Hot-Pressed Uranium Mononitride, BMI-1633 (EURAEC-706), p. 21 (May 30, 1963).

[11]R. A. Smith, W. M. Pardue, and D. E. Kizer, Progress Relating to Civilian Applications During June 1966, BMI-1778, p. C-1.

In our opinion, the problem of obtaining high density during sintering will be solved more quickly by development of a technique for grinding powder to a size of about 2 μ within a short time rather than by searching for a suitable sintering aid. Alternate techniques to sintering are uniaxial hot pressing or isostatic hot pressing.

There is evidence that the higher concentration of oxygen associated with fine (< 5 μ) powder results in a lower density of sintered fuel,[12] but with larger powder size (−80 mesh) the presence of oxygen as PuO_2 may help in sintering. However, the finer powder sinters to densities of 90 to 95% of theoretical,[11,12] while the coarser powders sinter to only 70 to 75% of theoretical.[9]

Pellets of high density probably cannot be made from coarse powders except by uniaxial hot pressing or isostatic hot pressing. Thus we must exclude oxygen during ball-milling as much as possible. Moreover, small amounts of contaminant oxygen have often been responsible for what little attack of the cladding has previously been observed.[13] Thus oxygen must be eliminated during hydriding and other steps in the fabrication process.

A sintering atmosphere of nitrogen or argon offers the most promise; neither hydrogen nor vacuum proved successful for PuN in earlier work.[2]

Psuedobinary System UN-PuN

No research on this system has been reported beyond lattice parameter measurement as a function of the concentration of PuN.[1,3,6,14,15]

---

[12] W. E. Roake, Pacific Northwest Laboratory Monthly Activities Report, July 1966, Division of Reactor Development and Technology Programs, BNWL-303, p. 30. OFFICIAL USE ONLY.

[13] B. J. Thamer, The Use of (U,Pu)N Fuel with a Sodium Bond: A Summary of Existing Data, LA-364, p. 6 (March 1967).

[14] J. Williams and R.A.J. Sambell, J. Less-Common Metals 1, 156 (1959).

[15] E. K. Storms, A Critical Review of Refractories, LA-2942, p. 231 (Aug. 13, 1964).

Nitride Fuel Cycle Studies

T. B. Lindemer

We are determining kinetics of the synthesis of uranium carbides, nitrides, and carbonitrides from sol-gel UO_2 in an effort to determine those factors that control the conversion reactions. This knowledge is fundamental to the eventual design of a fuel cycle for the production of the desired reactor fuel material. We are undertaking two related programs in this study.

The first program involves the conversion of sol-gel UO_2 to "UC_2" by solid-state reaction with powdered graphite in an argon atmosphere. This study, which was done as a part of the Gas-Cooled Reactor Project, showed that when a continuous layer of "UC_2" is formed on the surface of the microsphere, the reaction is apparently controlled by the diffusion of oxygen through the carbide from the UO_2 core to the surface. A typical conversion time for 420-μ (40-mesh) microspheres is 70 hr at 1600°C; if a discontinuous layer of UC_2 is formed, the time is reduced to approximately 10 hr. Conversion of the "UC_2" produced by the above reaction to the U(C,N) solid solution by reaction with nitrogen is the next step, which we will study.

The second program will be done in cooperation with the Chemical Technology Division. Sol-gel microspheres of UO_2 plus carbon will be converted to carbides and nitrides, and the kinetics of the reactions will be studied.

Thermodynamics of Plutonium Nitride

K. E. Spear J. M. Leitnaker

We are surveying and evaluating the thermodynamic information presently available on the plutonium-nitrogen system. This evaluation is necessary to define the critical areas in which thermodynamic data are lacking. A summary of the literature data and plans for research on the plutonium-nitrogen system are reported here. An analysis of the

thermodynamic properties of this system is in progress and will be reported later. In particular, we are evaluating the vapor pressure, enthalpy, entropy, and heat capacity data and are also analyzing the vaporization behavior of this system.

Phase Data

The only intermediate phase reported[15] for the plutonium-nitrogen system is the NaCl-type mononitride PuN. In contrast, the thorium-nitrogen system[16] exhibits three phases: ThN, Th_3N_4, and Th_2N_3, although recently the Th_2N_3 phase has been suspected[17] to be Th_2N_2O. The uranium-nitrogen system[18] contains UN, U_2N_3, and UN_2. In phase behavior, the plutonium-nitrogen system more closely resembles the systems of nitrogen with the rare earths than those with the actinides thorium and uranium. The rare-earth metals, scandium, and yttrium each form only one intermediate nitride phase, the NaCl-type mononitride.[19]

Congruent melting of PuN was not observed[20] at pressures up to 24.5 atm N_2. Two values are reported for the melting temperature at 1 atm N_2: 2584 ± 30°C (ref. 20) and 2556 ± 15°C (ref. 21).

The PuN solid solution range is reported[20] to be small, since the lattice parameters of samples annealed under various temperatures and nitrogen pressures were practically identical. Exposure of PuN to air[20] increased its cubic lattice parameter from 4.9055 A to as high as 4.9099 A (approx 4 at. % O).

---

[16] S. Aronson and A. B. Auskern, J. Phys. Chem. 70(12), 3937–3941 (1966).

[17] R. Benz, C. G. Hoffman, and G. N. Rupert, J. Am. Chem. Soc. 89(2), 191–197 (1967).

[18] R. Benz and M. G. Bowman, J. Am. Chem. Soc. 88(2), 264–268 (1966).

[19] G. V. Samsonov, High Temperature Compounds of Rare-Earth Metals and Nonmetals, Consultant Bureau, New York (1965).

[20] W. M. Olson and R.N.R. Mulford, J. Phys. Chem. 68(5), 1048–1051 (1964).

[21] D. F. Carroll, "PuN and the Refractory Nitrides," pp. 30–33 in A Seminar on Groups V and VI Anions held at Argonne National Laboratory February 26 and 27, 1964, ANL-6856 (March 1964).

Vaporization

Olson and Mulford[20] report decomposition pressures for the reaction

$$PuN(s) \rightleftharpoons Pu(\ell) = \tfrac{1}{2}\, N_2(g)$$

in the temperature range of 2290 to 2770°C. They represent their data by the equation

$$\log P_{N_2}(\text{atm}) = 8.193 - 29.54 \times 10^3/T + 11.28 \times 10^{-18} T^5 \ .$$

The last term in the equation corrects for the variation in the solubility limit of nitrogen in liquid plutonium with temperature.

Thermodynamics

Olson and Mulford[20] give an approximate value for $\Delta H^\circ_{f,298}(PuN)$ of −70 kcal/mole, based upon a limit determined from their decomposition pressure measurements. Campbell and Leary[22] found $\Delta G^\circ_{f,700}(PuN) = -60 \pm 1$ kcal/mole from electromotive force measurements and estimated entropy and heat capacity data to obtain $\Delta H^\circ_{f,298}(PuN) = -76$ kcal/mole. They estimate $\Delta S^\circ_{f,298}(PuN) = -22 \pm 1$ eu.

Experimental

From the literature analysis, we conclude that the stability of PuN is uncertain, perhaps by greater than 6 kcal/mole, the difference of the two values of the heat of formation. This uncertainty results in an uncertainty of more than a factor of 15 in the pressure of nitrogen over PuN(s) + Pu(ℓ). Since stabilities of potential intermetallic compounds of plutonium seem to be completely unknown, any estimates of PuN compatibility are of limited validity.

Thus, we should first measure pressures of nitrogen over PuN(s) + Pu(ℓ). Later, the pressures of nitrogen measured over multicomponent systems will yield definitive data for compatibility studies. For these reasons we are beginning design of a system to measure these

[22] G. M. Campbell and J. A. Leary, J. Phys. Chem. 70(8), 2703–2705 (1966).

nitrogen pressures. A similar apparatus not capable of glove-box operation has been described by Inouye and Leitnaker.[23] In addition to the problems encountered in the U-UN study,[23] two additional problems are expected in the Pu-PuN system. First, plutonium must be contained in a glove box, and the equipment must be designed accordingly. Second, plutonium is much more volatile than uranium, and some may evaporate during the long times necessary to attain equilibrium. We believe a microbalance to be a necessary adjunct.

We have obtained a Cahn microbalance and have ordered a mass-spectrometric residual-gas analyzer. The furnace arrangement has been designed and constructed. We are beginning design of the vacuum system, the last major problem before assembly of the equipment can begin.

We plan to operate the system without plutonium until sufficient experience is obtained to be sure that all major problems have been solved. Once plutonium is introduced into the system, replacing or repairing components will become much more difficult.

Synthesis of Uranium Nitride and Production of Fine Precipitates in It

T. G. Godfrey J. M. Leitnaker
R. A. Potter

Swelling of fuels during irradiation might be reduced through provision of nucleation and pinning sites for fission-gas bubbles. We are trying to provide these sites in uranium nitride through precipitation from a saturated solution of molybdenum in UN and through formation of second-phase particles by internal oxidation of a thorium-uranium nitride solid solution. We have needed a suitable facility for the reproducible synthesis and fabrication of UN of high quality and in adequate quantities, both for the study of introduction of dispersed precipitates and for other needs of this program and others. Recently our emphasis has been on the operation of our new facility for this purpose.

---

[23]H. Inouye and J. M. Leitnaker, "Equilibrium Nitrogen Pressures and Thermodynamic Properties of UN," accepted for publication by the Journal of the American Ceramic Society.

New Synthesis Facility

We have recently put into operation a new synthesis facility, shown in Fig. 3.1, that can routinely produce a high-quality UN powder. It consists of an Inconel retort heated by a resistance furnace that is mounted on horizontal tracks.

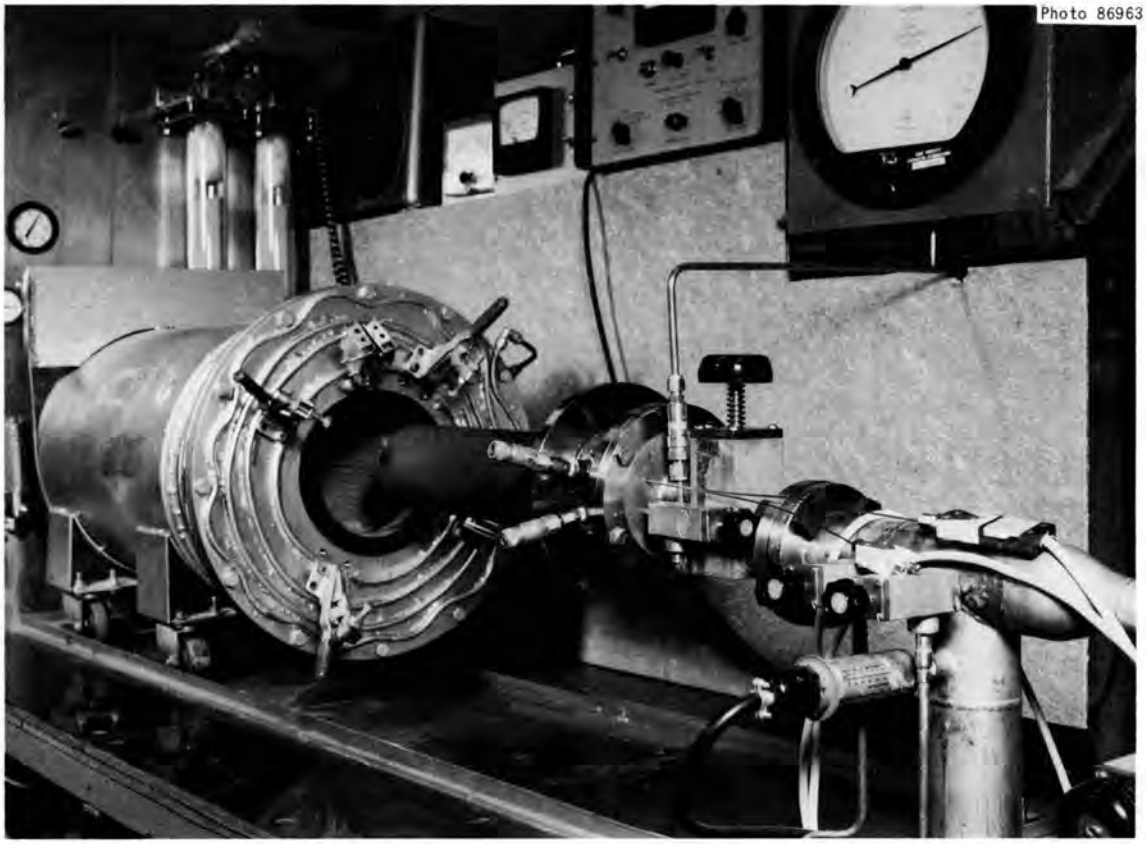

Fig. 3.1. Uranium Nitride Synthesis Apparatus. The furnace is retracted to show the Inconel retort.

The retort is loaded with the uranium metal sample within an argon atmosphere glove box capable of evacuation for cleanup. The flange is bolted on, and the brass block valve is closed. The assembly is transferred from the glove box to the synthesis station, where it is flanged to the vacuum-gas header. The furnace is moved into position, enclosing the retort. A second flange on the retort seals to the furnace and provides a means of blanketing the heated retort with argon.

[redacted]

We have chosen to use as the starting material massive uranium metal rather than the chips or shavings that are normally used. The cleaned and pickled metal is supported on a stainless steel screen over an Inconel boat. During the hydriding and dehydriding steps, the metal spalls to a fine powder and falls through the screen into the boat.

We have not investigated thoroughly all of the variables in the synthesis scheme, nor have we necessarily optimized the procedures. However, we have established a procedure that produces a high-quality UN powder that sinters readily to greater than 95% of theoretical density. Before the hydriding step, we heat the system under vacuum to 900°C to outgas the uranium, the retort, and all of the hardware. Purified hydrogen at 1 atm is introduced when the retort has cooled below 400°C. As the retort cools further and the hydrogen reacts with the uranium, hydrogen is added to maintain constant pressure. The retort is allowed to cool to about 150°C, and when the hydrogen uptake ceases the temperature is slowly increased to about 450°C. During the later stages of the heating the UH_3 decomposes, and the evolved hydrogen is vented to the atmosphere. This hydride-dehydride cycle is repeated about eight times to ensure that all of the uranium has been reduced to a very fine powder. After the final 450°C treatment, the hydrogen is displaced by argon, and the system is cooled to room temperature, evacuated, and backfilled to 1 atm with argon mixed with 20% purified nitrogen. The retort is slowly heated, and, as the nitriding reaction proceeds, nitrogen is added to maintain constant pressure until nitriding is complete at about 900°C. The U_2N_3 is then decomposed under a vacuum of 10^{-5} torr at 950°C until it is essentially UN. The retort is cooled, filled with argon, valved off, disconnected from the header, and transferred into the glove box for unloading.

The glove-box line contains all equipment necessary for sample preparation and pellet fabrication through the cold-pressing step. The UN is always exposed to a purified argon atmosphere except for the short interval during transfer to the sintering furnace. With our new procedures and equipment, we can routinely produce a sinterable powder that contains less than 400 ppm O.

[redacted]

Microstructural Variations in Sintered UN Arising from Synthesis of the Powder

We have often seen regions of cannibalistic grain growth in our sintered UN specimens made from both commercial and our own powders. We believe that these regions result from traces of uranium metal in the UN powder. During the nitriding step, the strongly exothermic reaction produces enough heat to fuse the fine uranium powder in some areas. This fused metal then resists nitridation. To eliminate this problem, we followed the nitriding step by a supplemental hydrogen treatment at 200°C. This reactivated the fused metal without affecting the UN. After the usual dehydriding step, the reactivated uranium was nitrided and denitrided during a repetition of the final steps of the synthesis scheme described in the previous section. Figure 3.2 compares the microstructure of material showing cannibalistic grain growth with that of a sintered specimen prepared from material that received this additional treatment. The latter shows no gross microstructural variations, nor have any specimens since we adopted the new procedure.

Preparation of Materials for Dispersion Studies

Now that we have confidence in our synthesis equipment and procedures, we will prepare nitride powders from uranium-molybdenum and uranium-thorium alloys. Uranium-molybdenum alloys containing from 0.1 to 10 at. % Mo have been arc-melted, and nitride specimens from these alloys will be used in sintering and annealing experiments to define the solid-solubility relationships that might lead to the formation of a finely dispersed precipitate.

Similarly, we have arc-melted a U–2% Th alloy and will prepare solid-solution nitride powders from it. With these powders, we will investigate the kinetics and equilibrium involved in the internal oxidation of the thorium by admixed UO_2 and the effect of additions of carbon on the process.

[redacted]

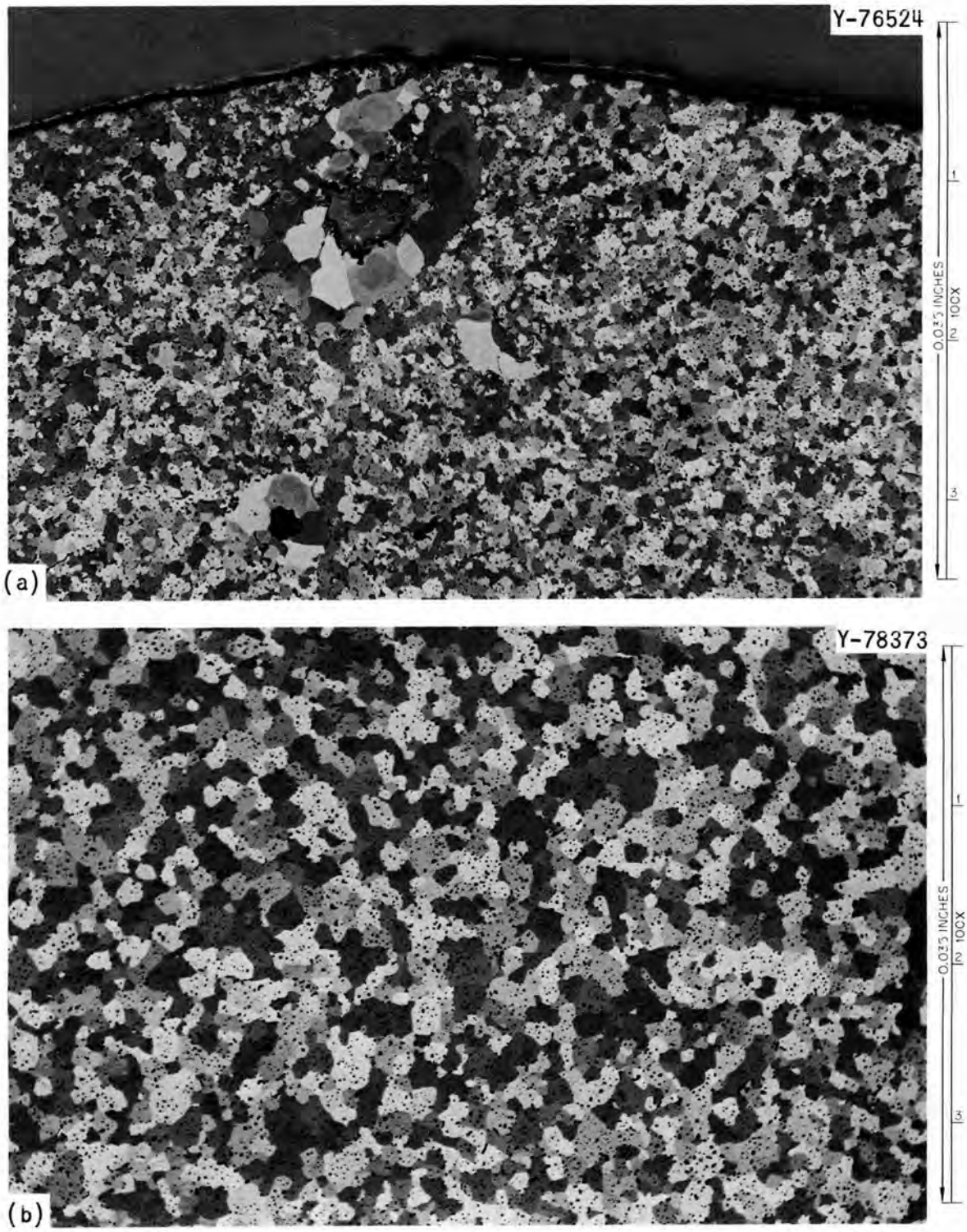

Fig. 3.2. Microstructures of Pressed and Sintered UN Prepared from ORNL-Synthesized Powder. (a) Specimen showing areas of cannibalistic grain growth. (b) Specimen from powder that had been given additional hydride-nitride treatment during synthesis. Etched: 30 lactic, 10 HNO_3, 1 HF.

[redacted]

[redacted]

4. NONDESTRUCTIVE TEST DEVELOPMENT

R. W. McClung

This program is intended to develop new and improved methods of nondestructively evaluating reactor materials and components. To achieve this we are studying various physical phenomena, developing instrumentation and other equipment, devising application techniques, and designing and fabricating reference standards. Among the methods being actively pursued are electromagnetics (with major emphasis on eddy currents), ultrasonics, and penetrating radiation. These and other methods are being evaluated for both normal and remote inspection.

Electromagnetic Test Methods

C. V. Dodd

Analytical Studies

We have continued research and development on both analytical and empirical bases. We previously had obtained a number of integral equations that represented solutions to various problems related to electromagnetic phenomena. We are now writing programs for time-sharing computers to evaluate these integrals.

A report[1] containing the derivation of these integral equations and other electromagnetic theory has been prepared and released. The abstract is presented below.

> This dissertation describes methods of solving electromagnetic induction problems by use of the vector potential. The differential equations for the vector potential are derived from Maxwell's equations, and cylindrical symmetry is assumed. This differential equation is then solved by two different basic techniques: a "closed form" solution and a relaxation solution.

---

[1]C. V. Dodd, Solutions to Electromagnetic Induction Problems, ORNL-TM-1842 (June 1967). Ph.D. Thesis, the University of Tennessee.

[redacted]

For the closed form solution, sinusoidal driving currents and linear, isotropic, and homogeneous media are assumed. The differential equation is solved for two different conductor configurations: (1) a rectangular cross-section coil above a plane with one conductor clad on another, and (2) a rectangular cross-section coil encircling a two-conductor rod. The solutions for both configurations are given in terms of integrals of Bessel functions.

The relaxation method is used for three different cases, the first being that for an applied current with a sinusoidal time dependence in a linear, isotropic, and inhomogeneous medium. The second case is a time sequential relaxation for an applied current with any type of time dependence in a linear, isotropic, and inhomogeneous medium. The third case is the same as the second, except the medium may be nonlinear.

In the relaxation method finite difference approximations are made for all terms in the differential equation, and the vector potential at every point is expressed in terms of the vector potential at neighboring points. The vector potential at every point may then be solved using a relaxation (iteration) technique for any particular configuration of coil and material.

Once the vector potential is determined, any physically observable electromagnetic phenomenon can be calculated from it. Equations are given for the eddy-current density, heating density, force density, induced voltages, and coil impedance for both perfect metals and metals with defects. Examples of the application of the relaxation technique to solve these problems and experimental verification of the answers are given. In most cases the agreement between calculated and measured values is good. These two techniques will allow the solution of a large number of electromagnetic induction problems.

Phase-Sensitive Eddy-Current Instrument

Work has continued on the portable phase-sensitive eddy-current instrument. We constructed printed circuit boards to simplify the maintenance problems and prepared templates so that the circuit boards can be constructed more economically. Photographs were made of the instrument and circuit board layout for external distribution through the ORNL Office of Industrial Cooperation.

Ultrasonic Test Methods

K. V. Cook

Ultrasonic Frequency Analysis

In an attempt to supplement or develop new variations of conventional ultrasonic testing, we assembled a system that analyzes the frequency spectra of individual packets or pulses of ultrasonic energy.

Figure 4.1 shows the block diagram of the frequency analysis system that we developed for use with immersed testing techniques. We are using conventional inspection instrumentation to generate and detect the pulses of ultrasonic energy. This type of instrumentation, Immerscope[2] or Reflectoscope,[3] and other similar units are used by a majority of nondestructive testing facilities. The frequency analysis equipment is attached to the basic inspection equipment and is used to monitor the frequency spectrum of ultrasonic pulses reflected from interfaces of interest.

The initial pulse and reflected signals detected by the transducer are connected into a preamplifier. The initial pulse of 500 to 1700 v saturates the amplifier and is effectively limited to a few volts at the output terminal. The reflected pulses, which arrive after the amplifier recovers from saturation, are amplified to a level more suitable for analysis and are fed into two successive mixers. Another input to the mixers is a rectangular pulse that allows the mixers to be used as pedestal-free gates. By proper synchronization of the gates with the reflected signals, any particular signal may be isolated and, after amplification, displayed on the spectrum analyzer. The analyzer displays the relative amplitudes of all frequency components in the range 0 to 25 MHz. A dual-trace oscilloscope is also utilized to monitor the detected signals and to select those of interest for analysis.

---

[2]Budd Company, Phoenixville, Pennsylvania.

[3]Automation Industries, Inc., Sperry Division, Danbury, Connecticut.

[redacted]

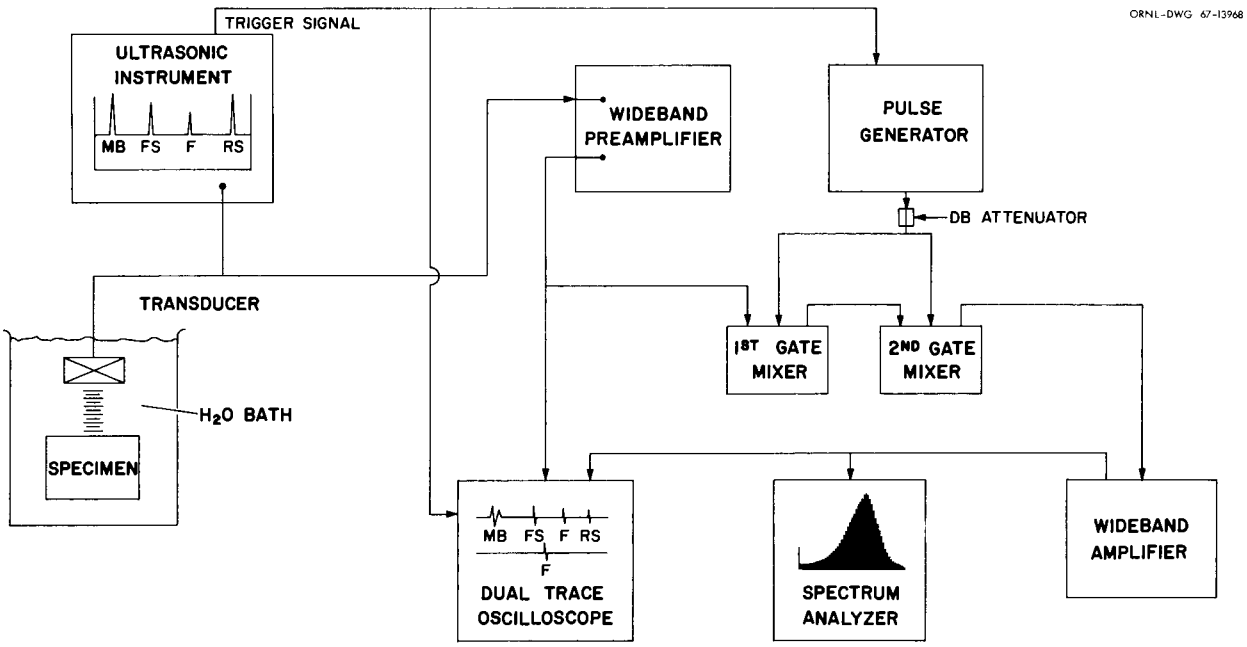

LEGEND

MB - MAIN BANG OR INITIAL SIGNAL

FS - REFLECTED SIGNAL FROM THE FRONT SURFACE OF THE SPECIMEN

F - REFLECTED FLAW SIGNAL

RS - REFLECTED SIGNAL FROM THE REAR SURFACE OF THE SPECIMEN

Fig. 4.1. Frequency Analysis System Used with Immersed Testing Techniques.

We are using this system to evaluate the frequency response of ultrasonic transducers when they are used in conventional testing situations. This evaluation is done by analyzing the signal reflected from the front surface of a test block. The frequency component of greatest amplitude is adjusted for full-scale deflection on the analyzer so that the relative amplitude of all components may be compared. Quartz transducers have a very sharply tuned response as shown in Fig. 4.2. In this figure the vertical lines, which are uniformly spaced and vary in amplitude, are frequency markers and the spacing between them represents a frequency change of 0.5 Mc. The first marker (reading from left to right) is at 0.5 Mc, the second 1 Mc, etc. Thus, as is evident from the photograph, a sharply tuned pulse at approximately 2.25 Mc is

[redacted]

Photo 88557

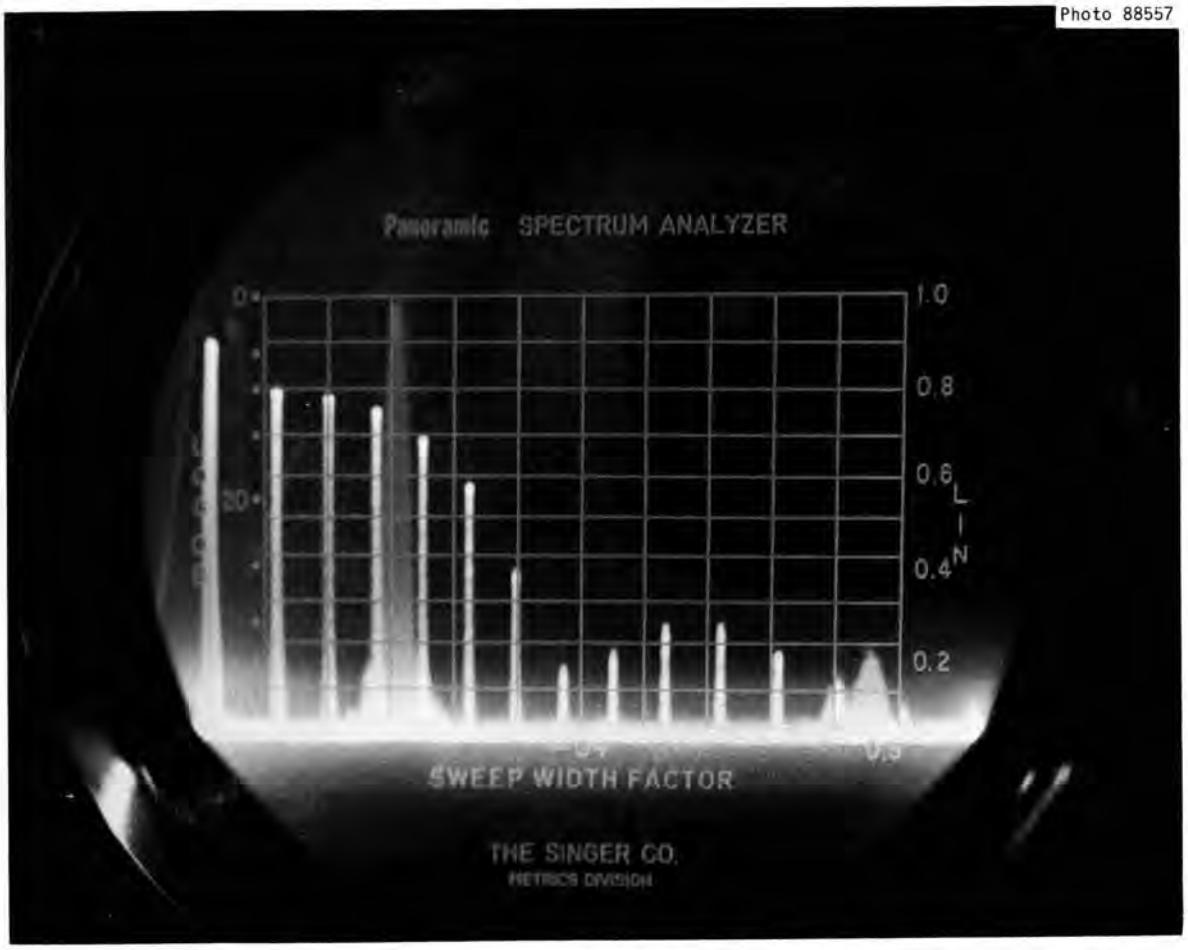

Fig. 4.2. Spectrum Display of 2.25 Mc Quartz Transducer Showing on a Vertical Log Scale the Amplitude Response at 2.25 Mc and at 6.75 Mc. The evenly spaced vertical lines are 0.5 Mc markers which begin with 0.5 Mc and increase from left to right.

generated by the quartz transducer which is labeled 2.25 Mc. There is also a smaller amplitude harmonic generated at approximately 6.75 Mc. We have noted that lithium sulfate and ceramic transducers are relatively broad-band crystals and do not always give the maximum response at the nominal (supplier labeled) frequency. We plan to continue these studies, as well as other promising uses, for the frequency analysis system.

Optical Visualization of Ultrasound (H. L. Whaley, K. V. Cook)

We made additional investigation of certain optical components for the schlieren system for viewing ultrasonic waves in transparent solids

and liquids. For the optical stop behind the second lens, four arrangements were compared. One is a simple, narrow slit (about 0.010 in. wide by 0.8 in. long) in an opaque sheet of material. In the plane of the slit, there is a single, central image of the light source before the ultrasound is propagated through the region of the collimated light. The diffraction of the light beam by an ultrasonic pulse causes light to be scattered from this central order into orders symmetrically arranged above and below the central order. Each order contains information necessary for the formation of an image of the ultrasonic pulse, but not identical images since acoustical intensity variations within a pulse cause light from different portions of the pulse to be scattered into different orders. Therefore, use of the narrow slit results in shaded detail within the pulse image as a function of intensity variations. This allows regions of different intensity to be evaluated by making vertical adjustment of the slit.

A simple knife edge may be used in place of the slit. The single jaw is set so as to block out the central order and admit all the orders above it to the second lens' image plane. This results in a uniformly bright pulse image after sufficient voltage has been applied to the transducer to scatter light from all regions of the pulse out of the central order. For a given ultrasonic intensity, the image of the ultrasonic pulse is brighter for use with the knife edge than for the slit since the orders all add to the formation of the image of the pulse in the focal plane of the second lens. However, contrast is not necessarily better since more light "noise" is admitted. At low ultrasonic intensity, shading is seen with the knife edge in use.

Use of a narrow, rectangular, opaque obstacle (i.e., effectively a double knife edge) is possible when a slit-type source is used. However, adjustment proved to be difficult, and the background of scattered light was somewhat brighter than for the slit or knife edge. Finally, a "circular slit" or annulus was employed with certain point light sources and also proved to be difficult to adjust properly. The optimum stop needed for each new setup will depend on such factors as the light source used, the ultrasonic frequency, and stray light.

[redacted]

The ground-glass viewing screen formerly used to display the schlieren image was replaced by a closed-circuit television camera. Viewing the image on the television monitor affords greater intensity, detail, and magnification, and thus makes it possible to work in subdued light instead of complete darkness.

Improvements in the system allowed us to observe several new phenomena. In one case as many as five reflections from the back surface of a thick steel block were visible as they emerged from the front surface of the block traveling toward the transducer. "Through-the-metal" reflections from machined grooves in a steel block were visually detected by us for the first time. A new technique employing two synchronized ultrasonic pulses which are successively intercepted by the light beam was devised. An interference pattern occurs superimposed on the image of a reference pulse due to the presence of the second pulse which is of such small intensity that, by itself, it is not visible. For example, the reference pulse is propagated in water while the second pulse is propagated in a medium like quartz. We have not been able to view a pulse inside quartz using a single transducer but have observed interference patterns appearing in the image of a reference pulse in water as the result of a second pulse entering the quartz block.

Several blocks for further studies with solids were ordered and received. These are about $3 \times 4 \times 2$ in. and are of optical glass, plexiglas, and polystyrene. Improvements in mechanical fixtures are planned to assure optimum setups and better reproducibility.

[redacted]

[redacted]

5. SINTERED ALUMINUM PRODUCTS DEVELOPMENT

W. R. Martin

Sintered aluminum products are powder-metallurgy-produced alloys that consist of aluminum oxide dispersed within an aluminum matrix. These alloys have a high strength-to-weight ratio, and this beneficial effect is stable up to temperatures approaching the melting point of aluminum.

Although these alloys are attractive for applications in several reactor systems, commercial SAP products lack the reproducibility of properties needed for many nuclear components. Our program was initiated to investigate the problems and parameters related to primary billet fabrication of SAP for HWOCR fuel rods and pressure tubes. General process steps involve feed-powder characterization, dispersion preparation, and consolidation.

Dispersion Preparation

G. L. Copeland

The experimental work on ball-milling SAP powder is complete and was reported in the previous quarterly report.[1] A topical report summarizing the investigation is in preparation.

We previously reported[1] that the gravity-fed magnetic filter was impractical for removing the included iron from the ball-milled slurry. Not so! The removal of 14 of the 21 magnetic grids from the filter and equidistant spacing of the remaining 7 grids have remedied our clogging problem. An 8 wt % oxide flake containing 0.70 wt % Fe passed through this filter arrangement without difficulty as a slurry with mineral spirits. Three successive passes produced iron contents, respectively, of 0.32, 0.25, and 0.25 wt %. A fourth pass with all 21 of the grids in place further reduced the iron content to 0.20 wt %. The starting

[1] G. L. Copeland, Fuels and Materials Development Program Quart. Progr. Rept. June 30, 1967, ORNL-TM-1941, p. 41.

[redacted]

atomized powder prior to ball-milling analyzed 0.24 wt % Fe. Thus, the tramp iron included during ball-milling can effectively and efficiently be removed by passing the slurry from the ball mill through a succession of magnetic grids.

Powder Consolidation

G. L. Copeland M. M. Martin

A draft of a detailed process specification has been prepared that includes all the steps involving powder and dispersion preparation in the production of SAP extrusion billets. We are completing several experiments that will establish more appropriate experimental data to support the specification.

Experiments are nearing completion from which we will determine the maximum permissible levels of the impurities Fe, C, and H; the duration of time required during the vacuum hot pressing and vacuum annealing of the billet; and the reproducibility of mechanical properties of material consolidated by this process in the larger billet size. These experiments are being performed with ORNL milled flake containing 10 wt % oxide. The laboratory work, including sampling of extrusions from seventeen 4-in.-diam billets, is completed. Our remaining task is the determination of mechanical properties from each of these billets. Evaluation of this concluding series of experiments will be based on the tensile properties at 450°C and 0.002 min^{-1} strain rate and the chemical composition of the extruded products.

In determining the oxide content of SAP rods, fast neutron activation analysis (FNAA) for oxygen is relatively inexpensive and less time-consuming than the standard gaseous HCl digestion wet chemistry method which determines oxide content. We established a correlation between the two techniques with a "least squares" fit of 42 paired data points. The linear relationship of oxygen content to oxide as determined by the two methods is given in Eq. (1) below:

$$x \pm 0.193 = 0.046 + 2.0529\ y\ , \qquad (1)$$

where

x = oxide, weight percent as given by the standard wet chemistry method,

y = oxygen, weight percent as determined by fast neutron activation analysis,

with

$2.66 \leq y \leq 4.07$,

$5.59 \leq x \leq 8.43$.

The above experimental coefficients closely approximate stoichiometric Al_2O_3. The maximum expected error in Eq. (1) is only ±7.2% of the value at a level of three standard deviations. A quadratic fit failed to significantly increase the quoted precision of the correlation. We conclude that oxide content is more efficiently determined from FNAA oxygen analysis and Eq. (1).

Mechanical Property Evaluation of SAP

D. G. Harman

The variability of mechanical properties of commercially available SAP material continues to be of interest. We are investigating the variation of ambient and elevated-temperature mechanical properties as measured parallel and normal to the extrusion direction.

The materials being investigated include SAP 895, SAP 930, and XAP-005. Properties have been obtained from the nose, center, and tail sections of commercially extruded 2-in.-diam, 18-ft-long solid rods.

Tensile specimens were machined parallel to the extrusion axis from positions near the outer circumference as well as from regions nearer the center. Transverse specimens were machined at 90° to the extrusion direction and intersecting the center line of the rod.

Tensile data were obtained at room temperature using a strain rate of 0.02 min^{-1} and at 450°C using strain rates of 0.02, 0.002, and 0.0002 min^{-1}.

The room-temperature data are included in Table 5.1. In all cases the room-temperature strengths were lower for the transverse direction.

[redacted]

Table 5.1. Room-Temperature Tensile Properties of Commercial SAP Extrusions at 0.02 min^{-1} Strain Rate[a]

Alloy Type	Specimen Location	Strength, psi		Elongation, %	
		0.2% Yield	Ultimate	Uniform	Total
SAP 895					
Nose Section	Longitudinal inside	34,980	44,480	7.6	10.9
	Longitudinal outside	35,570	44,300	7.2	11.0
	Transverse	28,520	37,860	5.6	6.4
Center Section	Longitudinal inside	30,250	40,250	7.8	11.6
	Longitudinal outside	32,670	42,520	9.1	13.9
	Transverse	31,420	42,350	6.2	6.3
SAP 930					
Nose Section	Longitudinal inside	20,440	30,340	13.3	15.1
	Longitudinal outside	20,520	30,690	12.6	16.3
	Transverse	17,630	26,620	11.7	11.7
Center Section	Longitudinal inside	21,890	28,830	13.7	16.8
	Longitudinal outside	20,020	30,520	12.2	15.3
	Transverse	17,730	26,380	14.0	14.3
Tail Section	Longitudinal inside	22,040	28,900	10.8	13.5
	Longitudinal outside	22,110	30,820	10.4	16.0
	Transverse	17,720	26,120	10.7	12.1
XAP-005					
Nose Section	Longitudinal inside	25,440	30,030	10.6	14.0
	Longitudinal outside	26,260	34,190	9.9	15.0
	Transverse	21,860	30,830	12.3	14.9
Center Section	Longitudinal inside	24,040	32,050	11.0	15.0
	Longitudinal outside	25,450	33,500	10.8	14.8
	Transverse	21,060	31,100	13.5	16.8
Tail Section	Longitudinal inside	21,440	31,600	11.9	15.5
	Longitudinal outside	24,090	31,630	12.1	15.0
	Transverse	21,170	29,120	14.6	17.4

[a]Specimens machined from 2-in.-diam × 18-ft extruded rod.

In the case of the parallel specimens, those representing material near the outside of the rod were consistently stronger than those nearer the center. The ductility differences between the two specimen directions varied with material. The XAP-005 showed better ductility in the transverse direction while SAP 895 and SAP 930 showed less. The alloy SAP 895 was most affected in this respect with total room-temperature elongation dropping from 10 to 12% longitudinally to 6% for the transverse direction.

[redacted]

[redacted]

The elevated-temperature tensile data are grouped according to testing strain rate in Tables 5.2, 5.3, and 5.4.

Table 5.2. Tensile Properties of Commercial SAP Extrusions at 450°C and 0.02 min^{-1} Strain Rate[a]

Alloy Type	Specimen Location	Strength, psi		Elongation, %	
		0.2% Yield	Ultimate	Uniform	Total
SAP 895					
Nose Section	Longitudinal inside	14,790	15,335	0.7	2.2
	Longitudinal outside	14,310	14,850	0.7	2.3
	Transverse	11,110	11,530	0.7	1.5
Center Section	Longitudinal inside	12,980	14,010	0.8	2.1
	Longitudinal outside	14,860	15,280	0.6	1.9
	Transverse	11,290	12,700	0.7	0.6
Tail Section	Longitudinal inside				
	Longitudinal outside	13,490	14,650		2.0
	Transverse	11,320	11,490		0.6
SAP 930					
Nose Section	Longitudinal inside	9,500	10,320	0.9	3.8
	Longitudinal outside	9,630	10,130	0.9	3.5
	Transverse	7,210	7,620	0.9	1.7
Center Section	Longitudinal inside	10,550	10,720	0.7	2.9
	Longitudinal outside	9,570	10,310	1.0	3.1
	Transverse	7,260	7,590	1.4	2.3
Tail Section	Longitudinal inside	9,050	9,610	0.9	4.6
	Longitudinal outside	9,070	9,520	1.0	3.4
	Transverse	6,340	7,150	1.2	1.7
SAP-005					
Nose Section	Longitudinal inside	10,040	10,700	0.9	2.4
	Longitudinal outside	10,170	10,730	1.0	3.1
	Transverse	9,220	9,220	0.2	0.7
Center Section	Longitudinal inside	10,490	11,060	1.1	2.6
	Longitudinal outside	9,400	10,310	1.0	3.1
	Transverse	7,660	8,440	0.9	1.3
Tail Section	Longitudinal inside	10,650	11,100	0.8	3.4
	Longitudinal outside	10,680	11,250	0.9	2.4
	Transverse	9,720	9,720	0.2	1.1

[a]Specimens machined from 2-in.-diam × 18-ft extruded rod.

[redacted]

Table 5.3. Tensile Properties of Commercial SAP Extrusions at 450°C and 0.002 min^{-1} Strain Rate[a]

Alloy Type	Specimen Location	Strength, psi		Elongation, %	
		0.2% Yield	Ultimate	Uniform	Total
SAP 895					
Nose Section	Longitudinal inside	12,920	14,030	0.7	1.3
	Longitudinal outside	12,900	13,760	0.6	1.3
	Transverse	9,260	9,510	0.6	0.8
Center Section	Longitudinal inside	12,610	13,150	0.8	1.5
	Longitudinal outside	14,130	14,380	0.5	1.3
	Transverse	11,110	11,160	0.6	1.1
Tail Section	Longitudinal inside				
	Longitudinal outside	12,410	12,900		1.4
	Transverse	9,080	9,240		0.9
SAP 930					
Nose Section	Longitudinal inside	8,340	9,450	1.0	1.6
	Longitudinal outside	9,120	9,620	0.6	1.8
	Transverse	6,240	6,490	0.7	1.6
Center Section	Longitudinal inside	8,680	9,770	1.0	2.3
	Longitudinal outside	9,340	9,830	0.8	2.2
	Transverse	6,470	7,050	0.9	1.6
Tail Section	Longitudinal inside	8,500	9,030	1.1	2.7
	Longitudinal outside	8,210	8,810	0.8	1.9
	Transverse				
XAP-005					
Nose Section	Longitudinal inside	9,590	10,080	0.7	1.6
	Longitudinal outside	9,040	9,810	1.1	1.8
	Transverse	7,480	7,930	0.4	0.7
Center Section	Longitudinal inside	9,810	10,670	1.2	2.1
	Longitudinal outside	8,790	9,700	1.0	1.6
	Transverse	6,930	7,220	0.8	1.1
Tail Section	Longitudinal inside	9,860	10,850	0.9	1.5
	Longitudinal outside	9,950	10,750	0.9	1.8
	Transverse	7,830	8,320	0.6	1.1

[a]Specimens machined from 2-in.-diam × 18-ft extruded rod.

The differences in longitudinal properties with respect to the cross-sectional location were not very large and showed no consistent relationship. Longitudinal properties did vary significantly, however, along

[redacted]

Table 5.4. Tensile Properties of Commercial SAP Extrusions at 450°C and 0.0002 min^{-1} Strain Rate[a]

Alloy Type	Specimen Location	Strength, psi		Elongation, %	
		0.2% Yield	Ultimate	Uniform	Total
SAP 895					
Nose Section	Longitudinal inside	11,680	12,550	0.4	0.9
	Longitudinal outside	11,110	11,940	0.5	1.0
	Transverse	7,230	7,440	0.6	0.8
Center Section	Longitudinal inside	11,320	11,530	0.6	0.9
	Longitudinal outside	11,740	12,510	0.6	0.8
	Transverse	7,770	8,510	0.5	1.0
Tail Section	Longitudinal inside				
	Longitudinal outside	10,720	11,390		1.1
	Transverse	6,690	7,430		1.0
SAP 930					
Nose Section	Longitudinal inside	8,080	8,660	0.6	1.1
	Longitudinal outside	8,440	8,990	0.4	1.2
	Transverse	5,090	5,300	0.4	1.7
Center Section	Longitudinal inside	8,280	8,760	0.6	1.5
	Longitudinal outside	8,510	9,160	0.6	1.5
	Transverse	5,570	5,740	0.4	1.5
Tail Section	Longitudinal inside	7,870	8,350	0.6	1.9
	Longitudinal outside	7,950	8,030	0.5	1.3
	Transverse	5,670	5,670	0.2	1.2
XAP-005					
Nose Section	Longitudinal inside	8,220	8,950	0.6	1.3
	Longitudinal outside	8,350	8,740	0.8	1.1
	Transverse	5,540	6,410	0.8	1.0
Center Section	Longitudinal inside	9,090	9,730	0.9	1.3
	Longitudinal outside	8,830	9,640	0.8	1.4
	Transverse		5,030		1.0
Tail Section	Longitudinal inside	9,010	9,670	0.8	1.2
	Longitudinal outside	8,860	9,590	0.5	1.4
	Transverse	6,720	7,050	0.6	1.3

[a]Specimens machined from 2-in.-diam × 18-ft extruded rod.

the length of each extrusion. Figures 5.1, 5.2, and 5.3 show the longitudinal properties as a function of extrusion length at the three strain rates. All three of the materials tested showed a variation in 450°C tensile strength of more than 10% and this depended on the strain

[redacted]

[redacted]

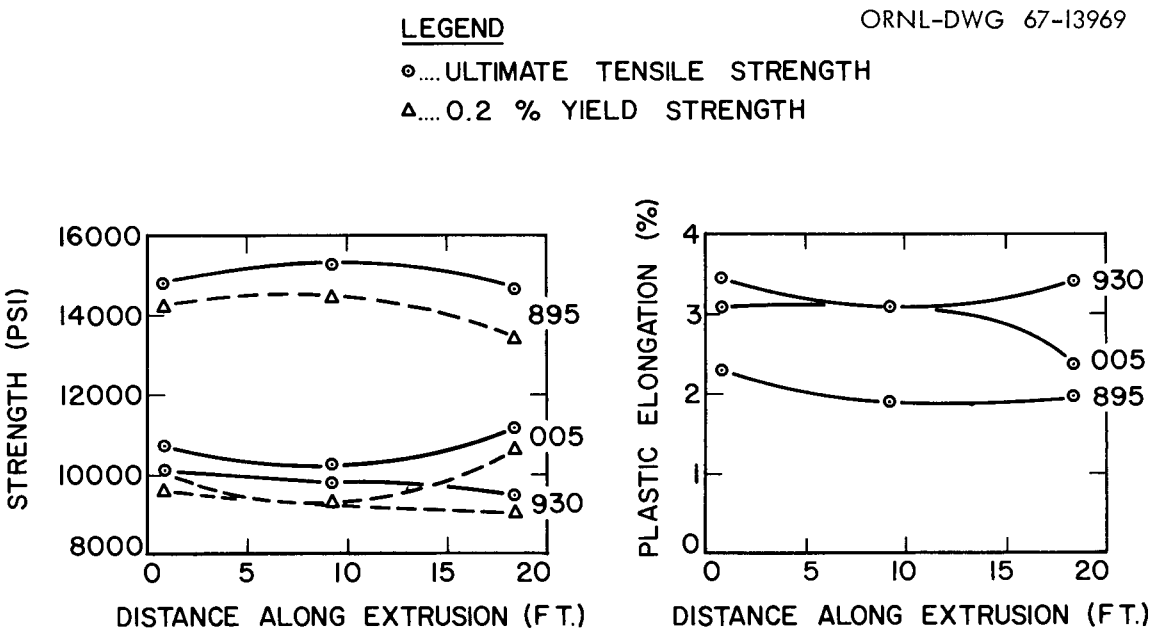

Fig. 5.1. Longitudinal Strength and Ductility of Three 18-ft Extrusions (SAP 895, SAP 930, and XAP-005) Tested at 450°C and 0.02 min^{-1}.

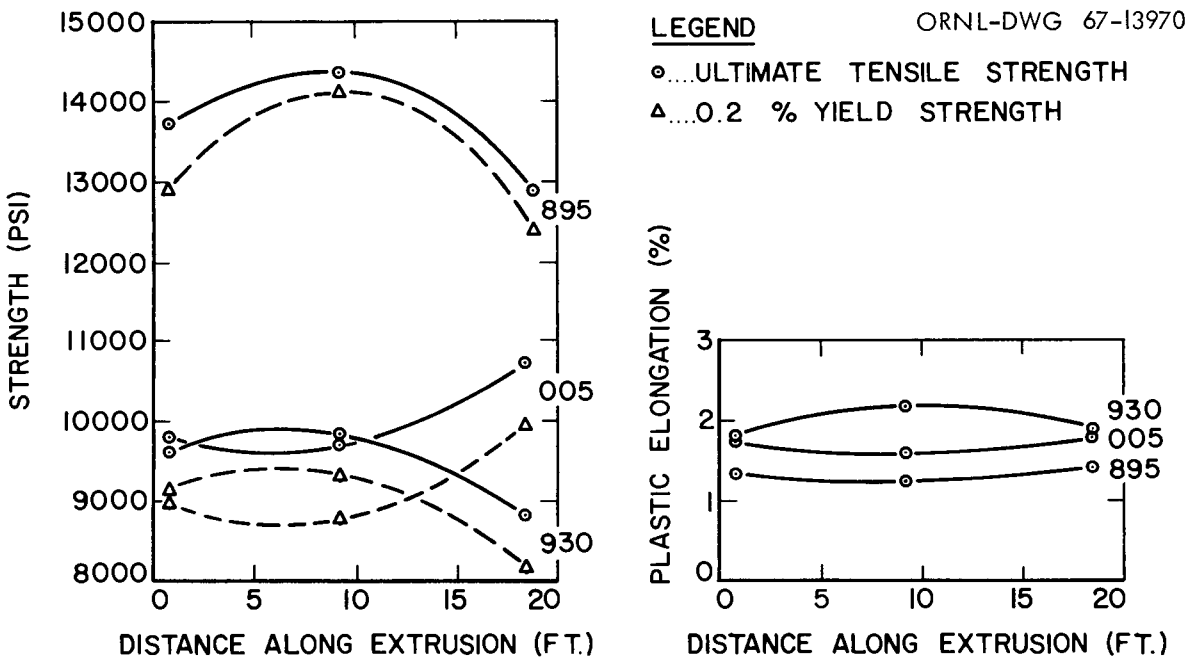

Fig. 5.2. Longitudinal Strength and Ductility of Three 18-ft Extrusions (SAP 895, SAP 930, and XAP-005) Tested at 450°C and 0.002 min^{-1}.

[redacted]

[redacted]

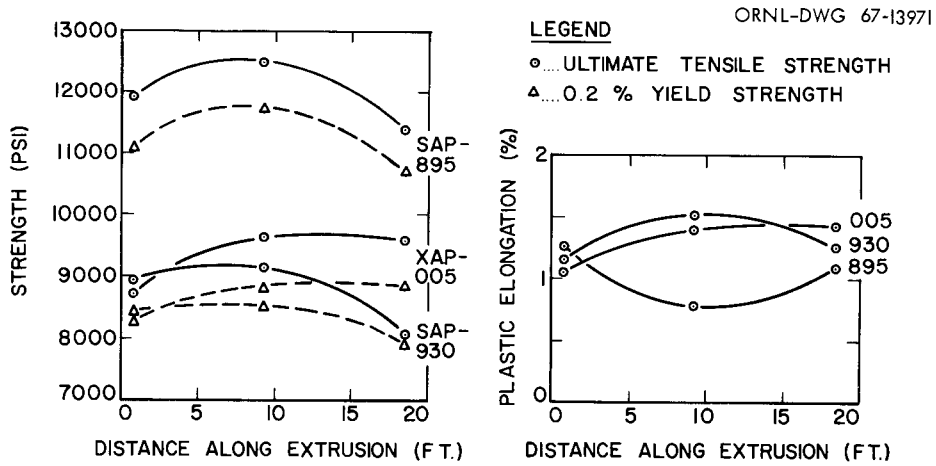

Fig. 5.3. Longitudinal Strength and Ductility of Three 18-ft Extrusions (SAP 895, SAP 930, and XAP-005) Tested at 450°C and 0.0002 min^{-1}.

rate. Table 5.5 shows the specific variation in strength for the various materials and testing conditions.

As expected, the lower oxide materials (XAP-005 and SAP 930) consistently showed better high-temperature ductility than the higher oxide SAP 895. Some variation in elongation values along the length of the extrusions can be seen in Figs. 5.1–5.3.

Table 5.5. Variation of 450°C Tensile Strength Along the Length of Commercial SAP Extrusions[a]

Strain Rate (min^{-1})	Orientation of Sample with Respect to Extrusion Direction	Variation in Tensile Strength, %		
		SAP 895	SAP 930	XAP-005
0.02	Longitudinal	4.1	6.3	9.3
	Transverse	10.4	5.6	15.5
0.002	Longitudinal	11.5	11.3	10.8
	Transverse	20.5	11.0	12.0
0.0002	Longitudinal	9.6	13.9	10.3
	Transverse	35.6	8.5	13.9

[a]Values given are from Tables 5.2, 5.3, and 5.4.

[redacted]

The elevated-temperature transverse properties are also included in Tables 5.2, 5.3, and 5.4. As is the case for the longitudinal specimens the strength is strain rate dependent. The transverse ductility, however, is relatively independent of strain rate. The alloy SAP 930 showed the highest values but all three materials exhibited 450°C transverse elongations of less than 2%.

The high-temperature transverse properties are shown as a function of extrusion length in Figs. 5.4, 5.5, and 5.6 at strain rates of 0.02, 0.002, and 0.0002 min^{-1}, respectively.

ORNL-DWG 67-13972

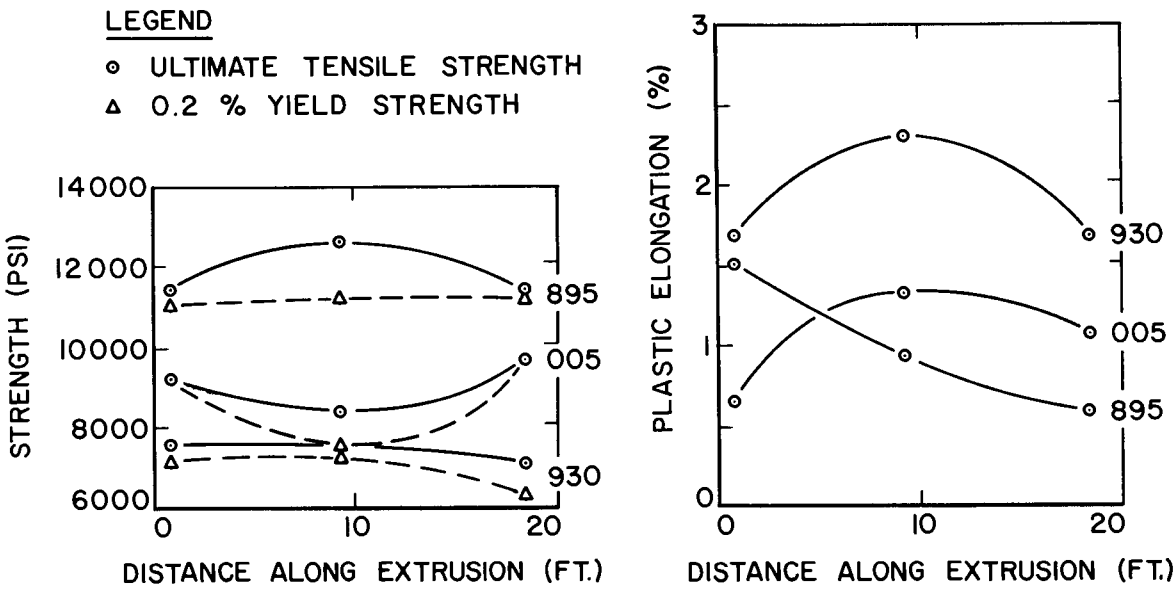

Fig. 5.4. Transverse Strength and Ductility of Three 18-ft Extrusions (SAP 895, SAP 930, and XAP-005) Tested at 450°C and 0.02 min^{-1}.

It is apparent from the figures that the transverse strength and, to some extent, the ductility of all three of these commercial SAP alloys is dependent upon the position along the extrusion. These variations of properties expressed as percentages are included in Table 5.5. The alloy SAP 895 showed the most variation in transverse strength, and this was most serious at the slower strain rates reaching 35.6% at 0.0002 min^{-1}; SAP 930 showed the least variation in transverse strength.

Considering the data presented it is not difficult to understand the large amount of scatter in mechanical property data that has been

[redacted]

ORNL-DWG 67-13973

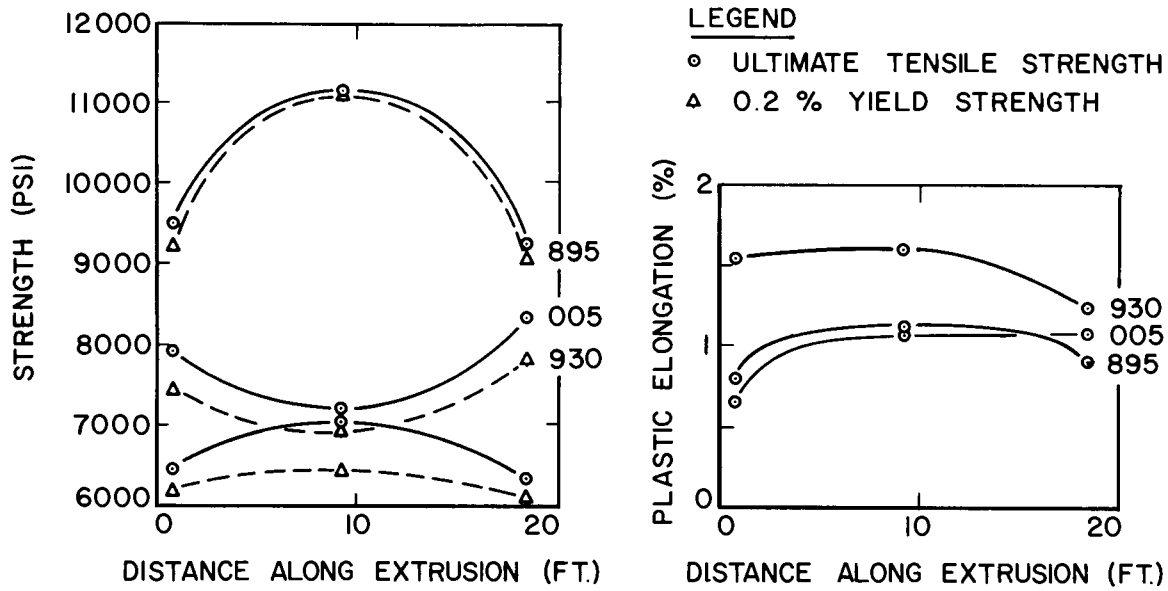

Fig. 5.5. Transverse Strength and Ductility of Three 18-ft Extrusions (SAP 895, SAP 930, and XAP-005) Tested at 450°C and 0.002 min^{-1}.

ORNL-DWG 67-13974

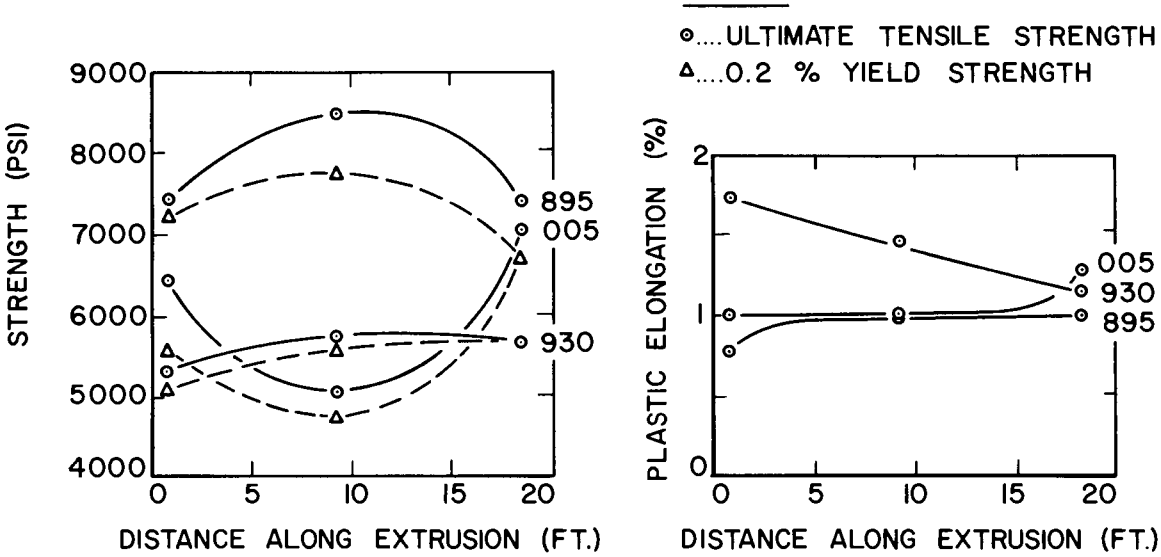

Fig. 5.6. Transverse Strength and Ductility of Three 18-ft Extrusions (SAP 895, SAP 930, and XAP-005) Tested at 450°C and 0.0002 min^{-1}.

reported for commercial SAP materials. Important considerations are testing conditions (e.g., strain rate and test-temperature control and distribution) and specimen location. Our transverse data can be extrapolated to the tube burst situation for extruded SAP tubing. Similar

[redacted]

dependence of properties on extrusion length would be expected from elevated-temperature tube burst test results of the three alloys. These data support the need for work on the effect of secondary working of SAP.

Secondary Working of SAP

T. M. Nilsson

A study has been undertaken investigating the effects of secondary working on the mechanical properties of SAP. The previous efforts for improvement of SAP properties have been concentrated on changes in initial aluminum powder, dispersion preparation, and consolidation procedure, with mechanical properties being evaluated after extrusions with a low reduction ratio. Little effort has been put into the determination of the effects of extrusion and further secondary working.

The microstructure of extruded SAP materials consists of a dispersion of fine Al_2O_3 particles in an aluminum matrix, divided into subgrains. Due to extrusion, the Al_2O_3 platelets are aligned and the subgrains are elongated in the extrusion direction.[2] This structure gives rise to the anisotropic behavior. Lower strength properties at high temperature are found if the tension axis is perpendicular to the extrusion direction instead of parallel as usual, the difference increasing with decreasing strain rate. This has been demonstrated by our recent work by Harman reported as Tables 5.1 through 5.4 of this section.

To study the anisotropy of the extruded product more thoroughly, we have cut specimens of SAP 895 at angles 0, 30, 45, 60, and 90° to the extrusion direction. Tensile specimens have been machined and will be tested at 21 and 450°C at different strain rates. Also, secondary working in a direction perpendicular to the original extrusion direction will be performed by extruding, swaging, and rod rolling. With such techniques it should be possible to break up the usual extruded structure. Already, extrusions in a direction perpendicular to the original direction

[2]M. Paganelli, Subgrain Size in 4, 7, 10 in 14% Al_2O_3 SAP Extruded Bars Thermal Treated at 600 and 650°C, EUR 1847·i (TT-64-26265) (1964).

have been made with reduction ratios from 1.5 to 15, using both conical and shear dies, and samples have been sent off for tensile specimen machining. The changes in microstructure will be followed by transmission electron microscopy.

In addition, the effects of large amounts of secondary working will be examined, since possible variations in properties are essential with respect to large-scale manufacturing of SAP. Extrusion, swaging, and rod rolling of SAP 895 at room temperature as well as at elevated temperature have been planned with reductions up to 2000. Evaluation of mechanical properties will be done by tensile testing, and changes in microstructure will be followed by optical and electron microscopy.

Nondestructive Evaluation of SAP

H. L. Whaley B. E. Foster

We have been concerned with the development of systems and techniques for determination of flake thickness and oxide content of the aluminum powders. An air-settling device has been developed for the flake-thickness measurements, and eddy-current conductivity measurements on fused compacts of SAP are being employed on the oxide content problem. The applicability of x-ray attenuation to billet homogeneity and oxide content determination is also being studied.

On the flake-thickness problem, two more powder samples of MD-3100 were dispersed and collected. A new method of measuring the width of the collected flake cross sections and a statistical analysis made on the time-sharing computer have allowed more realistic error limits to be included in the flake-thickness versus settling-position curves. A random sample of MD-3100 powder was prepared by depositing the flakes from a water solution onto a flat epoxy surface as the water evaporated. This sample was then sent to Metallography where it was processed in the same way as those collected by the air-settling device. This process allowed determination of the particle thickness range for the powder sample. After further data evaluation and confirmation, details of the interrelationship between the thickness range and the error limits will

be presented. Five samples of powder ball-milled by the Powder Metallurgy Group are also being examined to determine thickness ranges.

Eddy-current conductivity is being evaluated as a method for determining oxide content of small fused wafers. Analysis of the last three sets of fused SAP wafers for oxide content determination has led to the conclusion that the wafers cannot be made sufficiently homogeneous to give satisfactory results with the reflection-type eddy-current technique. Coils were wound and the necessary hardware constructed to build a rudimentary system to make through-transmission measurements on the wafers. Measurements were made for one set of 6.3% nominal oxide content wafers with a thickness range of 0.041 to 0.096 in. A similar test is to be performed at another oxide content to see how much separation due to oxide content change occurs by this technique. An x-ray method is being investigated as a backup technique.

An x-ray attenuation scanning technique is being evaluated as a means for determining the homogeneity of both pressed and extruded SAP billets. A variety of approximately 100% dense SAP billets with an oxide content range of 5.4 to 12.5% has been received. Specimens from these billets have been machined to desired thicknesses as shown in Table 5.6. These will allow a calibration curve for homogeneity evaluation to be established.

Advanced Sintered Aluminum Products

G. L. Copeland

The objective of this phase of the program is to improve the ductility of SAP products through alloying modifications. Our approach to the alloy development will be based on three mechanisms that may be responsible for the low ductility at elevated temperatures:

1. Lack of work hardening in the alloy allows deformation to occur locally with no uniform elongation once necking beings.

2. Gas collection at the incoherent oxide-matrix interface results in holes, which grow until failure occurs.

[redacted]

Table 5.6. SAP Specimen Thicknesses

Billet	Oxide Content (%)	Thickness (in.)
245, 247, 249	5.4	0.100
		0.200
		0.400
		0.700
		1.000
		2.000
244	6.5	0.100
		0.200
		0.400
		0.700
239, 240	8.1	0.100
		0.200
		0.400
		0.700
		0.900
		1.000
		2.000
261	9.9	0.100
		0.200
		0.400
		0.700
		1.000
		2.000
		3.000
SE48-V6U	10.5	0.100
		0.200
		0.400
		0.700
		0.800
		1.000
		2.000
		3.000
		4.000
256	12.5	0.100
		0.200
		0.400
		0.700
		1.000
		2.000
		3.000

[redacted]

3. Strain results in the soft matrix pulling away from the hard oxide particles. These voids grow by vacancy diffusion until failure occurs.

The first two mechanisms were suggested by the deformation and fracture characteristics observed during the process development of unalloyed SAP. The third mechanism has been suggested by Nilsson[3] in his thesis on the ductility of SAP.

Alloys of three types will be investigated:

1. Add solid-solution strengtheners to the aluminum matrix to provide work hardening. Magnesium is the most promising element for study because of its high solubility and its effective increase in the lattice parameter. The alloyed powder will be ball-milled to obtain the desired oxide content and particle shape.

2. Alloy the matrix with the compound-forming elements such as Mo, Zr, Fe, Ti, V, and Cr. Prealloyed powders produced by atomization contain these elements as a fine dispersion of intermetallic compounds. These compounds are relatively stable in the aluminum matrix and promote strength to quite high temperatures. Ball-milling to produce a fine particle size and introduce oxide to stabilize the fine structure may produce an alloy with excellent room-temperature and high-temperature strength even under creep conditions. The stronger matrix may allow a decrease in the oxide required, thus achieving a minor gain in ductility.

3. Blend fine aluminum powder with dispersoids. By blending the dispersoid particle with atomized aluminum powder, the dispersoid can be varied while keeping other processing parameters constant. It is hoped that a dispersoid can be found that is coherent with the matrix to a large extent for evaluation of the mechanism of gas collection at the oxide-matrix boundary. This will require a similar planar spacing along with a similar coefficient of thermal expansion. In addition, blending with softer particles will allow an evaluation of the effect of particle strength on ductility, which will test the differential strain mechanism for hole formation.

---

[3]T. M. Nilsson, Investigation of the Ductility of Dispersion Strengthened Aluminum-Aluminum Oxide Alloys, Ph.D. Thesis, the Technical University of Denmark, November 1965.

Alloy preparation following introduction of the dispersoid by ball-milling or blending will utilize the process parameters developed for unalloyed SAP and will be held constant for all alloys. This technique will allow a direct scale-up to production quantities similar to that used for the unalloyed SAP. Hansen[4] has previously shown that blended aluminum-aluminum oxide dispersions have properties very similar to those of conventional SAP.

We have previously concluded[5] that alloying elements must be added by atomizing liquid alloys so that a fine powder size with resulting rapid quenching is obtained, in order to keep the size of intermetallic compounds small. Since we could not find a vendor able or willing to produce fine alloyed powders, we had decided to atomize the powders at ORNL. However, the Illinois Institute of Technology Research Institute (IITRI) has contracted to modify their atomization process parameters for production of aluminum alloy powders in small batches with a significant −325 mesh size fraction. The Institute has about 10 years experience in the production of small quantities of alloyed powders of a larger size than we desire. The powders produced during their process development will be used in our program to increase the ductility of SAP. This approach will provide us with initial alloy powders and with the capability of producing our own powders more quickly than if we undertook the development of the atomization process with no previous experience.

The Institute is producing alloyed powders of both the solid-solution type and of the intermetallic-compound type. In addition, alloyed powders containing magnesium made by a spinning electrode-arc melt technique have been ordered from Whittaker Corporation, Nuclear Metal Division. These powders are larger in size and will provide information on the effect of powder size on milling characteristics and properties of the dispersion.

---

[4]N. Hansen, Trans. Met. Soc. AIME 230, 263 (1964).

[5]G. L. Copeland, Fuels and Materials Development Program Quart. Progr. Rept. March 31, 1967, ORNL-TM-1825, p. 42.

[redacted]

6. ZIRCONIUM METALLURGY

P. L. Rittenhouse

Zirconium-base alloys are used in the nuclear industry as fuel cladding and as pressure tubing. In many cases advanced power reactor design is limited by the properties of these alloys. Our primary concern is to improve the strength and corrosion resistance of alloys that are in use at present. We are sure that substantial increases in design strength can be realized by advantageous use of the anisotropy that exists because of preferred orientation. We are also encouraged by our finding that anodic films can inhibit corrosion.

Anisotropy in Zircaloy

P. L. Rittenhouse

Tubing Test Program

Internal pressure tests on Zircaloy tubing are scheduled to begin next quarter. Specimens are being machined from 15 lots of tubing. The redesigned grip system is completed and modifications have been made to the hydraulic system to improve internal pressure control. We also designed, built, and calibrated a strain gage for measuring diametral expansion.

Torsion Tests

We have completed torsion tests on 12 lots of Zircaloy tubing. A torsion test performed on thin-wall tubing defines a point on the plane stress yield surface in the quadrant bounded by axial tension (σ_{+z}) and tangential compression ($\sigma_{-\theta}$). The energy-of-distortion condition predicts that for z,θ plane stress:

$$\sigma^{\circ}_{+z}/\tau^{\circ} = \sigma^{\circ}_{-\theta}/\tau^{\circ} = 1.225 \ ,$$

[redacted]

[redacted]

where

τ° = yield strength in torsion,

σ°_{+z} = yield strength in axial tension,

$\sigma^\circ_{-\theta}$ = yield strength in tangential compression.

This is generally experimentally verified for ductile isotropic metals (i.e., metals with equal properties in all directions and in tension and compression).

Values of σ°_{+z}, τ°, and the ratio $\sigma^\circ_{+z}/\tau^\circ$ are given in Table 6.1. The value of the ratio ranges from about 0.8 to 1.2. These extremes relate to the yield surface in the tension-compression quadrant of the z,θ plane as shown in Fig. 6.1(a) and (b). Perhaps a more realistic ratio to examine is one that takes into consideration both σ°_{+z} and $\sigma^\circ_{-\theta}$. (The tangential compression yield strength was determined by the microhardness anisotropy technique described earlier).[1] The point at which

[1]P. L. Rittenhouse, Fuels and Materials Development Program Quart. Progr. Rept. March 31, 1966, ORNL-TM-1500, p. 28.

Table 6.1. Torsional Yield Relationships for Zircaloy Tubing

Material Code	σ°_{+z} (psi)	τ° (psi)	$\sigma^\circ_{+z}/\tau^\circ$	τ°_{min} (psi)	$\tau^\circ/\tau^\circ_{min}$
	$\times 10^3$	$\times 10^3$		$\times 10^3$	
W-2	58	50	1.16	48	1.04
W-3	60	66	0.91	50	1.32
W-4	58	47	1.23	46	1.02
W-5	55	46	1.20	44	1.05
W-6	60	60	1.00	49	1.22
W-7	61	57	1.07	49	1.16
U-1	60	62	0.97	50	1.24
U-2	62	65	0.95	51	1.27
U-3	54	52	1.04	44	1.18
Y-2	54	67	0.81	45	1.49
S-2	61	56	1.09	47	1.19
T-1	60	62	0.97	46	1.35

[redacted]

[redacted]

ORNL-DWG 67-10426

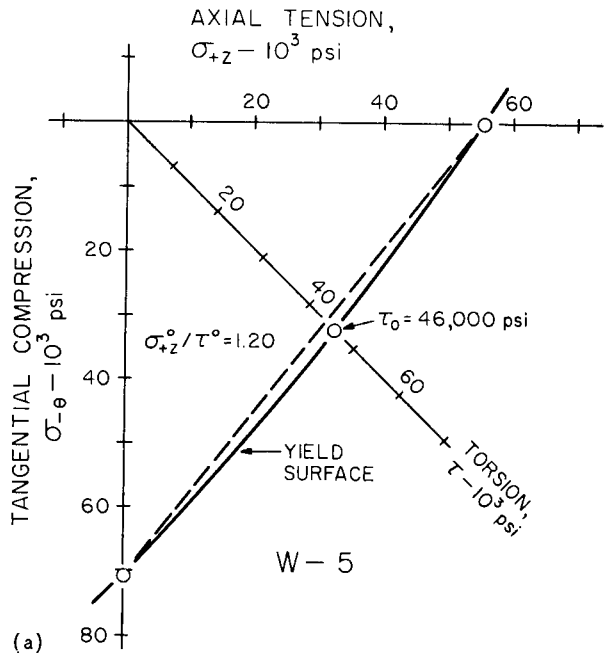

ORNL-DWG 67-10595

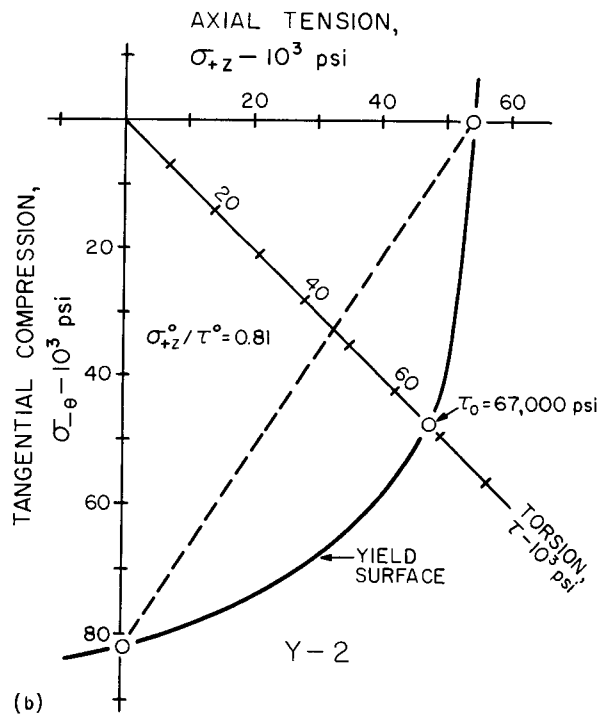

Fig. 6.1. Axial Tension – Tangential Compression Quadrant of the z,θ Plane Stress Yield Surface. (a) Zircaloy tubing with basal poles oriented radially. (b) Zircaloy tubing with basal poles oriented tangentially.

[redacted]

the dashed line joining σ°_{+z} and $\sigma^\circ_{-\theta}$ intersects the torsion yield coordinate (see Fig. 6.1) gives the minimum value of torsion yield strength, τ°_{min}, consistent with yield surface criteria (i.e., values less than τ°_{min} would result in a concave loading surface).[2] The value τ°_{min}, then, may be thought of as the value predicted by a maximum-shearing-stress theory that allows $\sigma^\circ_{+z} \neq \sigma^\circ_{-\theta}$. In Table 6.1, $\tau^\circ/\tau^\circ_{min}$ is shown to vary from 1.02 to 1.49. Values approaching unity are characteristic of Zircaloy tubing with the major fraction of its grains oriented with basal poles parallel to the tube radius (W-5). Neither the axial nor the tangential direction is texture strengthened so τ° is relatively small and $\tau^\circ \rightarrow \tau^\circ_{min}$. If, however, the texture is such that the majority of grains have basal poles parallel to the tangential direction (Y-2), the magnitude of τ° should be — and is — enhanced and $\tau^\circ > \tau^\circ_{min}$.

Circumferential Texture Gradients in Zircaloy Tubing

P. L. Rittenhouse D. O. Hobson

We have noticed that annealed Zircaloy tubes tested in tension deform to cross sections that range from circular to square. The shape of the cross section is constant within any given lot of material. This suggests that the significant variable may be preferred orientation (texture). A uniform texture affects the ratio of wall-to-diameter reduction ($\Delta t/\Delta d$) but the cross section should still be circular. If, however, the texture varied around the circumference, $\Delta t/\Delta d$ would also vary and noncircular cross sections could be formed on plastic loading.

A ring was cut from the shoulder of one of the tube specimens that showed a square cross section. Back-reflection Laue x-ray shots were taken at positions on the tube surface corresponding to the corners and edges of the square to determine the relative intensities of basal poles, $I_{(0002)}$, at these points. The value of the ratio $I_{(0002)corner}/I_{(0002)edge}$

[2] D. C. Drucker, Proc. 1st U.S. Congr. Appl. Mech. (ASME), 489 (1951).

was found to be 0.75. Therefore, when this tubing is tested in uniaxial tension, $\Delta t/\Delta d$ should be greater at the corner than at the edge position. This self-imposed restraint could lead to the cross-section shape observed.

We felt that a more accurate and complete method of examining the texture variation was needed. To satisfy this need, we rotated the ring about the tubing axis with the x-ray beam focused on the tube surface and diffraction conditions set for a constant 2θ. We were thus able to examine the variation in diffracted intensity of selected crystallographic planes around the entire circumference. Figure 6.2 shows the measured variation in intensity of the (0002), $\{10\bar{1}0\}$, and $\{10\bar{1}1\}$ parallel to the tube surface as a function of rotation about the tube axis. Four intensity peaks or cycles are seen. These are more clearly evident for $\{10\bar{1}0\}$ and $\{10\bar{1}1\}$ than (0002) and are, as expected, 90 deg out of phase with (0002). These data are consistent with the back-reflection Laue shots and with the shape of the cross section (shown schematically in Fig. 6.2).

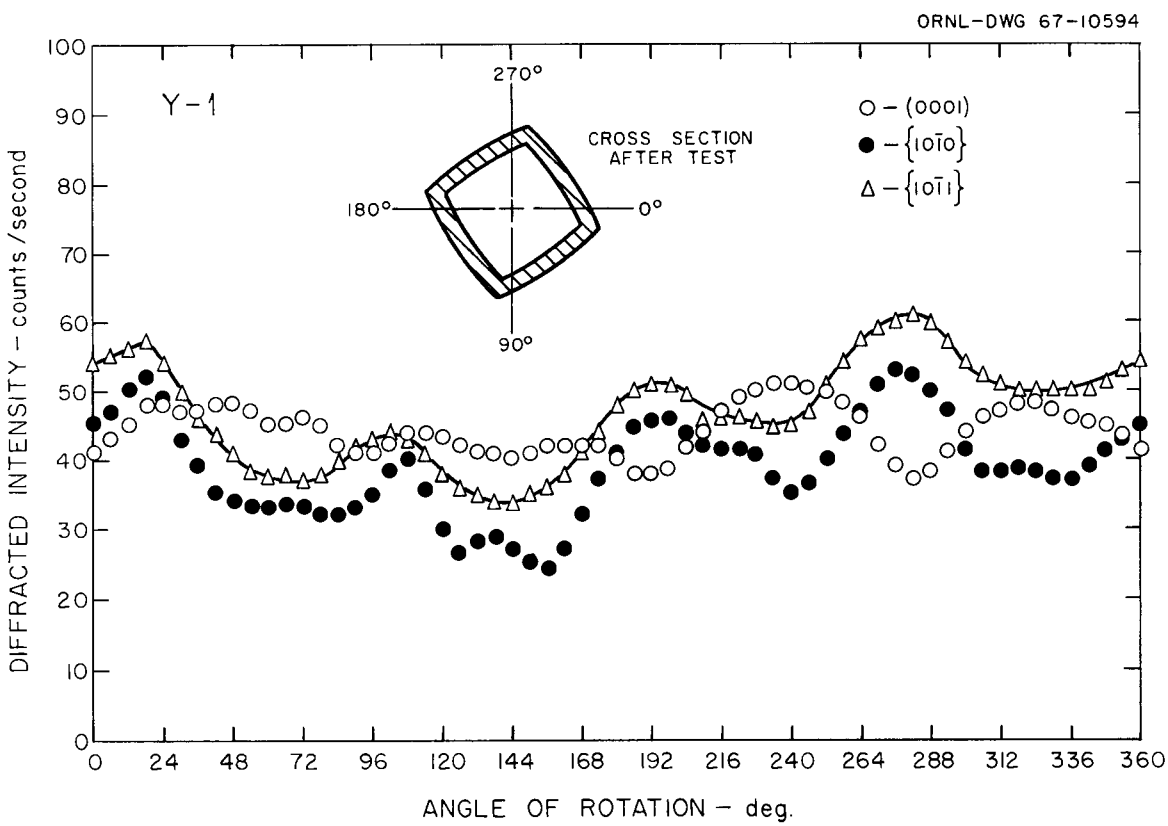

Fig. 6.2. Variation in Diffraction Intensity of (0002), $\{10\bar{1}0\}$, and $\{10\bar{1}1\}$ as a Function of Rotation Angle of the Tube in Y-1 Zircaloy Tubing.

A specimen with a circular cross section after test was examined next. The results for the (0002) and $\{10\bar{1}0\}$ are shown in Fig. 6.3. There is a small variation in texture around the circumference, but it is evidently insufficient to cause gross distortion of the cross-section shape. A third specimen was selected from a tube that had a cross section best described as polyhedral (a series of flats or low places). Figure 6.4 shows the five-cycle variation in (0002) and the ten-cycle variation in {1010} and {1011} for this material. The cross-section shape, shown schematically as a pentagon, was actually somewhat more complicated.

Texture gradients are often found through the thickness and from edge to center in rolled products. We have previously seen variation in texture through the wall in Zircaloy tubing.[3] We were still surprised, at least initially, to find these circumferential texture gradients. Perhaps the more easily explained of the gradients reported here is that which seems the more complicated. Material W-2 (Fig. 6.4) was an experimental lot produced by "tube reducing." In tube reduction the diameter and wall thickness are reduced by two reciprocating tapered dies and a tapered mandrel. The mandrel and tube remain stationary during the power portion of each reduction cycle but between power strokes they are rotated (indexed) and the tube is fed forward. This procedure might well result in variation of reduction around the circumference if the dies are not properly machined or if the indexing angle is too large. In fact, a "wrinkle" finish can be seen on the outside diameter of the as-fabricated tubing, but not to the extent seen in the machined gage section after testing. If the degree of reduction varies around the circumference, the texture produced will also vary. It is interesting to note that the tube was indexed 60 to 72 deg between each power stroke (the exact angle is not known) and that the variation in intensity of the (0002) is in a 72-deg cycle. We do not know why the variation in $\{10\bar{1}0\}$ and $\{10\bar{1}1\}$ is tenfold rather than fivefold.

---

[3]P. L. Rittenhouse, Fuels and Materials Development Program Quart. Progr. Rept. Sept. 30, 1966, ORNL-TM-1700, p. 35.

[redacted]

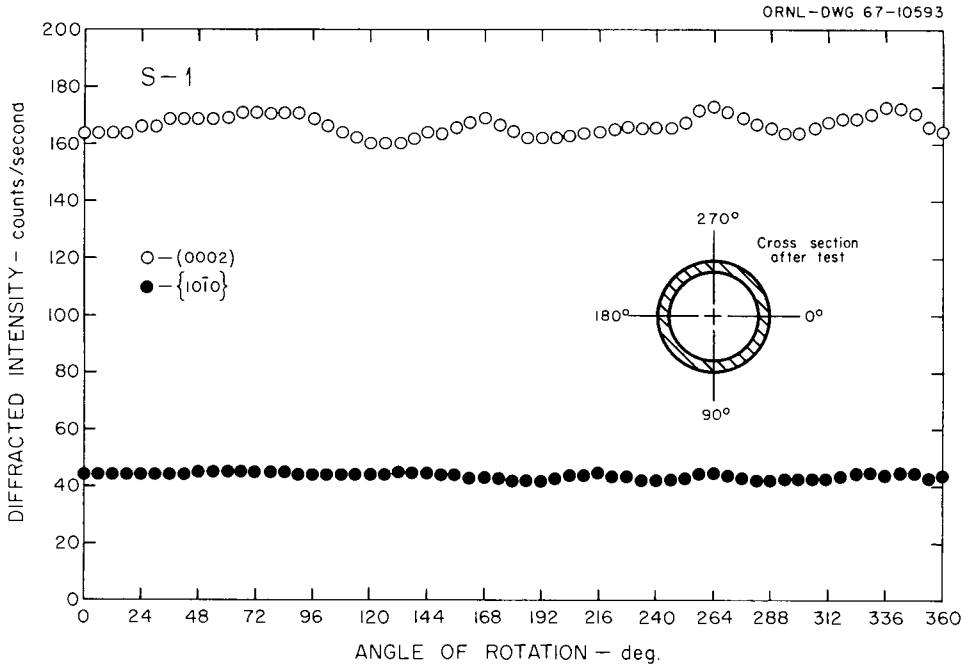

Fig. 6.3. Variation in Diffraction Intensity of (0002) and {10$\bar{1}$0} as a Function of Rotation Angle of the Tube in S-1 Zircaloy Tubing.

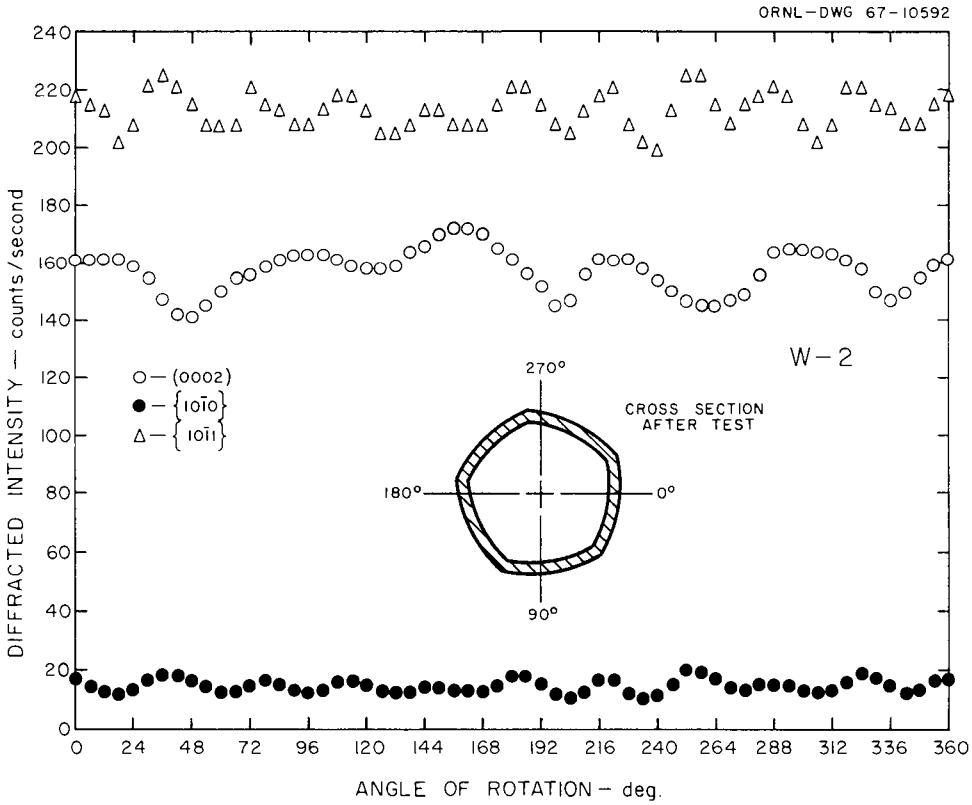

Fig. 6.4. Variation in Diffraction Intensity of (0002), {10$\bar{1}$0}, and {10$\bar{1}$1} as a Function of Rotating Angle of the Tube in W-2 Zircaloy Tubing.

[redacted]

The tubing that showed the square shape, Y-1, was not tube reduced. The fabrication procedure consisted of forging to a tube shell, piercing and machining, extrusion, and tube drawing. This procedure offers much less chance of the texture gradient being the result of variation in reduction around the circumference. Even with damaged or scored dies or variation in wall thickness of the extrusion, both of which could cause gradients, we would not expect the texture variation cycle to be regular. We propose that it is more likely that the variation in texture arises in the forged tube shell. Examination of a forging or compression specimen will show that regions of high deformation may alternate in a cruciform pattern with regions of relatively low deformation. These regions are represented by the shaded and unshaded areas on the tube shell in Fig. 6.5(a). The texture variation around the circumference would be like that in Fig. 6.5(b). Based on what we know of the deformation of zirconium alloys, we are certain that this variation will be reflected in the texture of the final product.

We believe that this is the first instance in which circumferential texture gradients have been reported for tubing. We are convinced that continued study is very important for these gradients must certainly influence the behavior of the tubing under operating stresses.

Texture Development in Single-Crystal Zirconium

D. O. Hobson

Schmid Factors

A portion of this report period has been used to develop, with the help of G. R. Love,[4] a computer program that calculates the orientation (Schmid) factors for the four major deformation systems in zirconium for any given crystal orientation in a three-axis orthogonal stress situation. The program was extended further to calculate the Schmid factors as the crystal orientation was incremented over an octant of the stereographic

[4]Group Leader, Superconducting Materials, Metals and Ceramics Division.

[redacted]

ORNL-DWG 67-10727

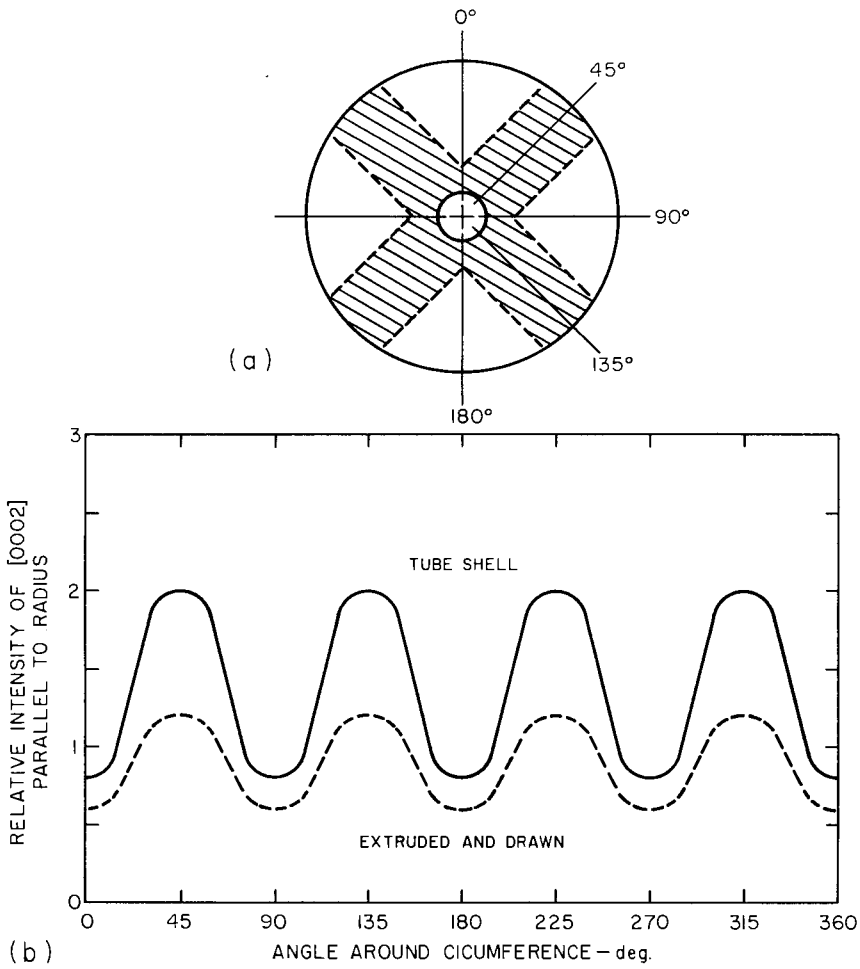

Fig. 6.5. Schematic Representation of Texture Variation in a Zircaloy Tube Shell. (a) Regions of high (shaded) and low (unshaded) deformation. (b) Relative intensity of (0002) around the circumference of the tube shell and the finished tubing.

sphere (approximately 600 orientations). The results of these calculations were analyzed for the biaxial stress state encountered in sheet rolling. This analysis allowed us to determine which deformation system has the greatest resolved shear stress in any specified position on the stereographic projection. Figure 6.6 shows the areas in the stereographic octant in which the basal pole should lie to allow the listed deformation system to operate. The Schmid factor is strictly a geometric entity and serves only as a guide in predicting the operative deformation system. For instance, according to the Schmid factor, both $\{10\bar{1}2\}$ and

[redacted]

[redacted]

ORNL-DWG 67-10726

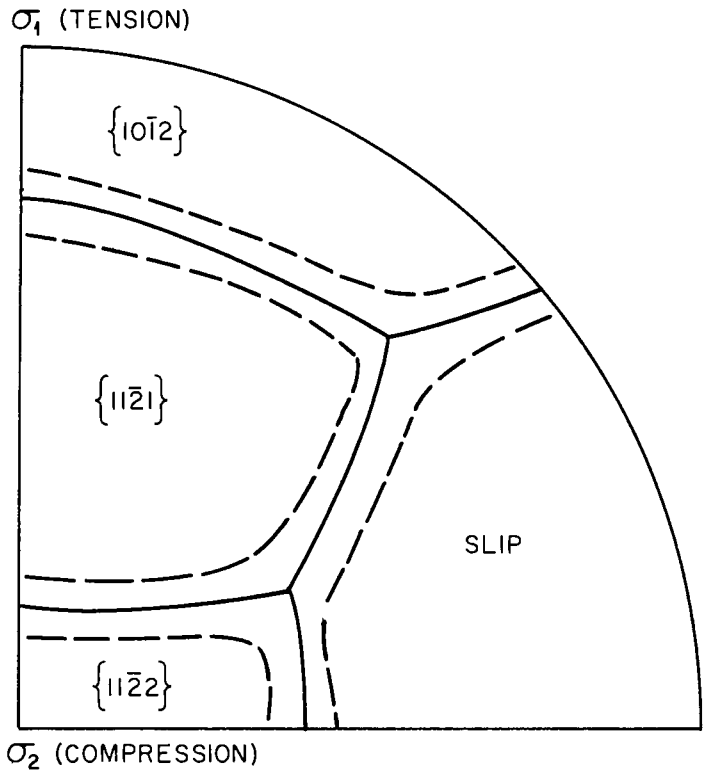

Fig. 6.6. Stereographic Octant Illustrating the Deformation Systems that will Operate when the Basal Pole is in the Labeled Regions. The area between the dotted lines is due to ambiguity caused by rotation of the crystal about the basal pole.

$\{11\bar{2}2\}$ twinning should act in compression along the basal pole. Twinning by $\{10\bar{1}2\}$, however, results in an expansion along the basal pole and will not occur on basal compression. Also, the Schmid factor gives only the resolved shear stress whereas the critical resolved shear stress must be known to give an exact prediction of the deformation system that will operate. It can be inferred that slip is much easier to initiate than twinning because slip is found to occur in some areas where the Schmid factor predicts twinning. In spite of the shortcomings enumerated, the Schmid factor is still valuable for roughly predicting the deformation systems that should operate for a given specimen strain.

[redacted]

Rolling Textures

In the previous report in this series,[5] we gave preliminary results of our single-crystal rolling studies. A texture diffractometer was received this quarter, installed, aligned and a number of specimens have been run. The new unit confirmed our findings that only a small amount of deformation is required to alter the original single-crystal texture into a completely new texture. The specimen with a $(11\bar{2}0)[0001]$ initial orientation was found to have twinned so that the (0001) poles were 30 deg on each side of the normal direction toward the transverse direction after only 20% reduction in thickness. The texture was quite sharp. Further rolling to 60% reduction in thickness tended to spread the texture toward the normal and the transverse directions. This study will be continued by studying specimens of other orientations and by studying the variation of texture through the thickness of the specimens by etching layers off the surface and rerunning the texture determinations.

Inhibition of Oxidation by Anodic Films

J. C. Wilson

We conducted corrosion tests in 360°C water (at 2700 psi, for 14 days) to see if preanodizing in H_3PO_4 would improve the oxidation resistance of zirconium under these conditions as it does in 500°C steam.[6] Most of the specimens were annealed and electropolished strips of arc-melted and rolled, crystal-bar zirconium. Anodized films were formed at 100 v in 14.7 M H_3PO_4 at a current density of 1 mA/cm^2. To assess the effects of possible contamination of unanodized specimens with phosphorus from the anodized films on other specimens, two autoclaves were used. The first contained both control and anodized specimens, the second only control (unanodized) specimens.

---

[5]D. O. Hobson, Fuels and Materials Development Program Quart. Progr. Rept. June 30, 1967, ORNL-TM-1941, p. 58.

[6]J. C. Wilson, Fuels and Materials Development Program Quart. Progr. Rept. June 30, 1967, ORNL-TM-1941, p. 66.

Although the weight gains of the groups of control specimens in the two autoclaves (9.4 and 9.0 mg/dm^2) differed by less than 5%, metallographic examination disclosed distinct differences in oxide color, incidence and morphology of localized grain-boundary oxidation, and other minor features.

In all cases the preanodized specimens showed lower weight gains in 360°C water than the control specimens. But if the total oxide weights (preanodized oxide plus oxide formed in water) are compared, the preanodized specimens gained up to 25% more weight than the controls. Longer exposures (in progress) will be necessary to judge the effectiveness of preanodizing treatments at 360°C. After oxidation in 360°C water the uniform film thickness of the preanodized specimens was measured by interference spectroscopy. This thickness was much less than indicated by the weight gain measurements. Therefore, most of the weight gain of the preanodized specimens in the water occurred as localized oxidation.

Preanodizing in H_3PO_4 did effectively reduce weight gains by factors of 3 and greater for as-rolled zirconium, particularly if the metal was in the chemically polished condition. The as-rolled metal gave weight gains of 30 to 300 mg/dm^2 depending upon the surface preparation. We do not know whether fluorine contamination in pickling or the state of the metal itself was responsible for the high weight gains. Whatever the reason, it appears that preanodizing in H_3PO_4 can, under certain conditions, drastically reduce oxidation in 360°C water. If the anodizing effects persist for longer times it is possible that otherwise unacceptable metal may be salvaged by preanodizing.

Oxidation data were obtained in 500°C air to compare with earlier results in steam at the same temperature. Preanodizing in H_3PO_4 has reduced the weight gains very little (about 20% after 900 hr) in tests still in progress. Attempts to incorporate more phosphorus in the anodized film by holding specimens at the anodizing voltage for periods of 2 and 69 hr apparently resulted in film breakdown. This was shown by visual appearance and leakage current. These specimens oxidized more rapidly than the control specimens in 500°C air.

Zirconium single-crystal plates of (0001), $(10\bar{1}0)$, $(11\bar{2}0)$, and $(10\bar{1}5)$ orientations were oxidized in air and steam for use in determining the

oxide-metal epitaxial relationships by x-ray diffraction. Preliminary data for a 2000-A film (formed in air at 423°C) on the basal plane showed that the (100) plane of the monoclinic oxide is strongly oriented parallel to the (0001) plane of the zirconium. There appears to be a large multiplicity of directional relationships that we have not yet sorted out.

Three new corrosion rigs for use in 400 to 600°C steam (15 psia) are under construction. These multiple facilities will enable us to ascertain the degree of contamination of corrosion specimens from phosphorus transferred from anodized films on other specimens during the oxidation process.

Phosphorus Concentrations in Anodic Films Formed in H_3PO_4

J. C. Banter[7]

The incorporation of phosphorus into zirconium oxide films formed anodically in H_3PO_4 was demonstrated earlier.[8] The fact that phosphorus slowed the dissolution rate of the oxide into the metal suggested that preanodizing might be effective in reducing the oxidation of zirconium. More recently it has been shown that preanodizing in H_3PO_4 does diminish oxidation in 500°C steam,[6] and the effect was found to depend on the acid concentration in the anodizing solution.

The following experiments were designed to measure the phosphorus contents of anodized films on zirconium as a function of two parameters, the current density and the H_3PO_4 concentration.

Cold-rolled chemically polished foils of arc-melted, crystal-bar zirconium were anodized at 60 v in 0.05 to 14.7 M aqueous solutions of phosphoric acid. Anodizing at the lower current density, 1 ma/cm^2, has been used for previous oxidation inhibition experiments. The process takes about 5 min. We shall refer to this as "slow" anodizing. "Fast" anodizing is done at a current density of 50 ma/cm^2 and is completed in

[7]Consultant from Florida Atlantic University, Boca Raton, Florida. Work performed at ORNL from Aug. 14 to 25, 1967.

[8]J. C. Banter, J. Electrochem. Soc. 114(5), 508–511 (1967).

a few seconds. The higher current density has been used in previous anodizing experiments where anodizing was used to delineate microstructures.

Windows of a single thickness of the anodically formed oxide were made by dissolving away the metal substrate in a solution of 20 vol % bromine in ethyl acetate. The absorbance of a constant area of stripped oxide film was measured (in transmission) in the absorption band (near 10 μ) characteristic of the phosphate ion in inorganic compounds. After calibrating the spectrophotometer with 0.084 and 0.147 M solutions of phosphoric acid in acetone (in a cell of known thickness), the amount of phosphorus in the films could be calculated. The thickness of the oxide films was estimated by visual color comparison with anodized standards of known thickness.

Figure 6.7 shows the results: the phosphorus concentration varies from 1% (by weight) for films formed in 0.05 M H_3PO_4 at 1 ma/dm^2 to 7% for films formed in 14.7 M H_3PO_4 at 50 ma/dm^2. Because the distribution of phosphorus in the anodized film is not uniform, as inferred earlier from film dissolution experiments,[8] the phosphorus concentration in the outer layer of the oxide is probably much higher than the bulk percentage calculated here. A similar dependence of phosphorus concentration of H_3PO_4 molarity has been found in anodic films formed on tantalum.[9]

The above results show: (1) that the phosphorus content of anodized films can be increased by anodizing at higher current densities than have been used for preanodizing corrosion specimens; and (2) that higher H_3PO_4 concentrations, as used in later oxidation experiments, also increase the phosphorus concentration in the films.

---

[9]J. J. Randall, Jr., W. J. Bernard, and R. R. Wilkinson, Electrochim. Acta 10, 183–201 (1965).

[redacted]

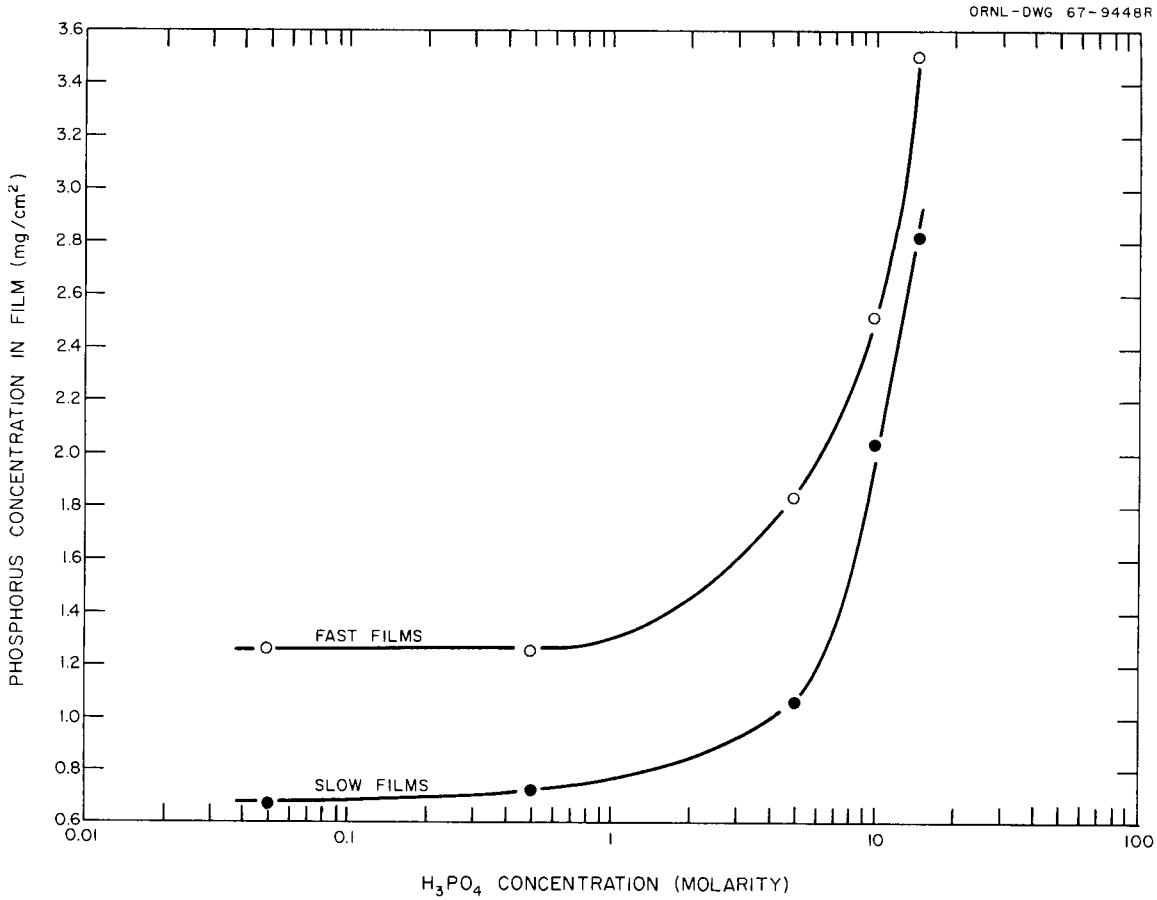

Fig. 6.7. Phosphorus Concentrations in Anodic Zirconium Oxide Films as a Function of Phosphorus Concentration in the Anodizing Solution. All films were formed at 60 v. The fast films were formed at a current density of 50 ma/cm^2, and the slow films at 1 ma/cm^2.

[redacted]

7. WELDABILITY OF NICKEL-BEARING ALLOYS

G. M. Slaughter

During this report period, we completed the preliminary weldability studies on the previously reported, special Incoloy 800 alloys.[1] Weldability results were obtained from Rensselaer Polytechnic Institute under subcontract, and high-temperature mechanical property results pertaining to weldability were obtained at ORNL. As expected, the preliminary data analyses pointed out the need for additional special heats of material to fill information gaps. Several special heats of Incoloy 800 are currently being processed for this purpose.

Special Alloy Fabrication

W. J. Werner R. E. McDonald
D. A. Canonico

Seven additional experimental Incoloy 800 alloys were formulated and are currently being processed for Gleeble[2] and VARESTRAINT[3] testing. The alloys for Gleeble testing are of the high-purity basic ternary composition but contain systematic additions of aluminum, titanium, sulfur, phosphorus, and sulfur plus phosphorus. VARESTRAINT alloys are also essentially pure ternaries; one contains an aluminum addition and the other a titanium addition.

---

[1]W. J. Werner, R. E. McDonald, and D. A. Canonico, Fuels and Materials Development Program Quart. Progr. Rept. June 30, 1967, ORNL-TM-1941, pp. 69–73.

[2]E. F. Nippes et al., Welding J. (N.Y.) 34(4), 183-s–196-s (1955).

[3]W. F. Savage and C. D. Lundin, Welding J. (N.Y.) 44(10), 433-s–442-s (1965).

Hot-Ductility Testing

D. A. Canonico W. J. Werner

Hot-ductility testing of the experimental Incoloy 800 alloys containing titanium plus aluminum, titanium plus aluminum plus sulfur, titanium plus aluminum plus phosphorus, and titanium plus aluminum plus sulfur plus phosphorus were conducted using the Duffer's Gleeble. This test is being used to determine the high-temperature mechanical properties of simulated weld heat-affected zones in our special alloys. By use of this test we can estimate the ability of a particular heat-affected zone microstructure to withstand stresses during a welding cycle without cracking. Two high-temperature properties were measured: strength and ductility. The temperatures at which these properties go to zero are the criterion for assessing weldability. In addition, the recovery of ductility is of equal importance. In general, the zero ductility temperature (ZDT) is lower than the zero strength temperature (ZST). This is because the ZST is associated with grain-boundary liquation. The ZST is probably the more important of the two since any strain imposed on the material at this temperature will result in hot cracking.

Figures 7.1 through 7.4 show the hot-ductility results compiled to date. The solid curves were obtained on heating and the dashed curves were obtained on cooling from the ZDT temperature. Quite surprisingly, the recovery of ductility on cooling of all the experimental Incoloy 800 alloys is very satisfactory from a weldability standpoint. In all cases, the ZDT is in the 2350 to 2450°F temperature range. It was quite surprising that the alloys containing sulfur and/or phosphorus additions were indistinguishable from the other alloys. It was because of this that the previously mentioned sulfur, phosphorus, and sulfur plus phosphorus doped ternary alloys were formulated. It is felt that the titanium and/or aluminum when present is tying up the sulfur and phosphorus and, thereby, masking their effects. Thermodynamic data are available that lend credibility to this postulate. Table 7.1 shows the available free energy of formation data on the sulfur compounds of interest. It is an established fact that manganese is commonly used to

[redacted]

ORNL-DWG 67-13975

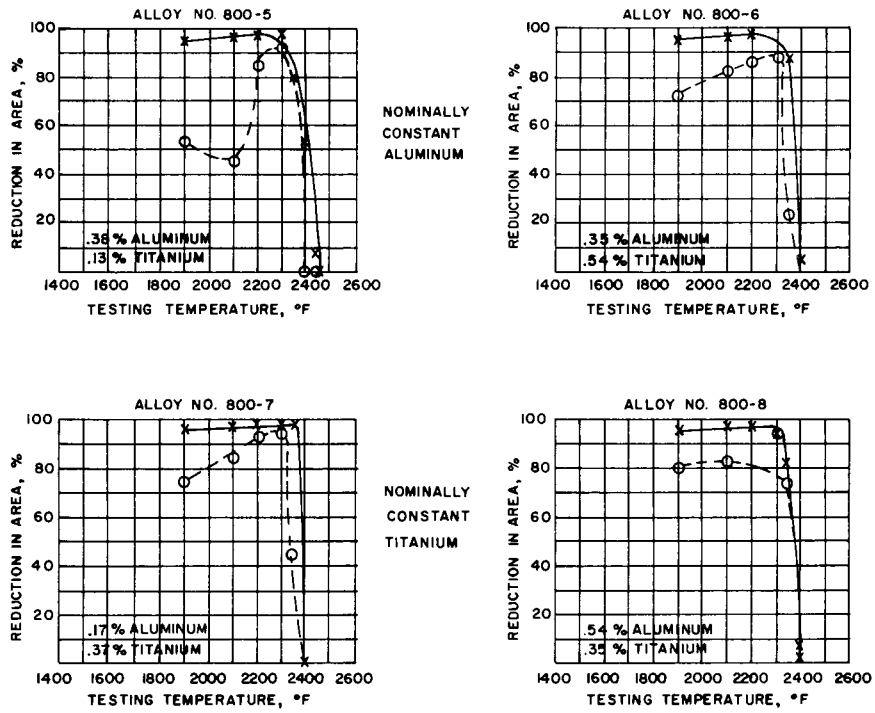

Fig. 7.1. The Individual Effect of Titanium and Aluminum on the Hot Ductility of the Experimental Incoloy 800 Alloys.

ORNL-DWG 67-13976

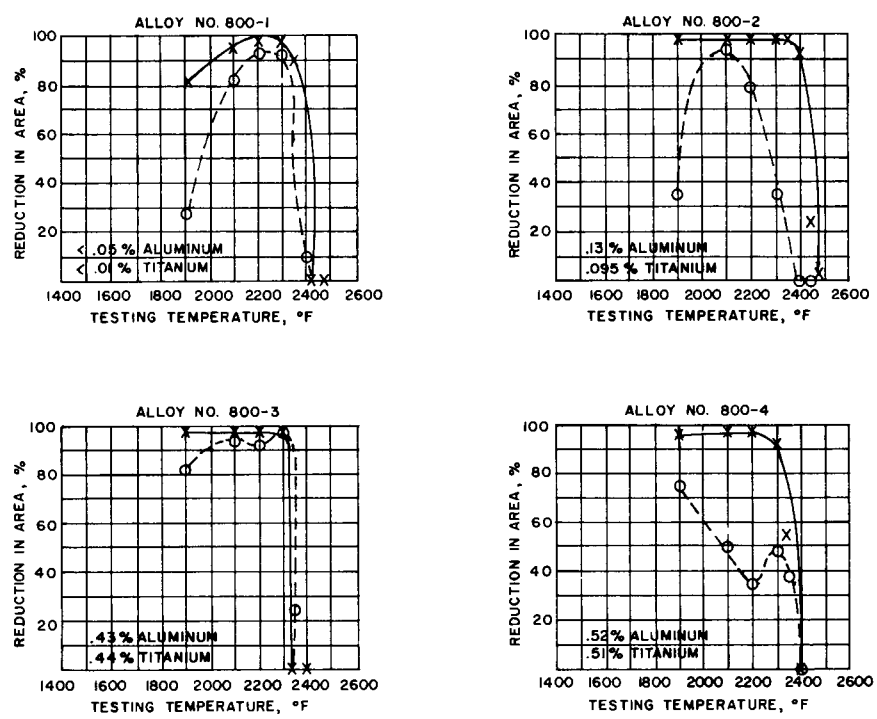

Fig. 7.2. The Combined Effect of Titanium and Aluminum on the Hot Ductility of the Experimental Incoloy 800 Alloys.

[redacted]

[redacted]

ORNL-DWG 67-13977

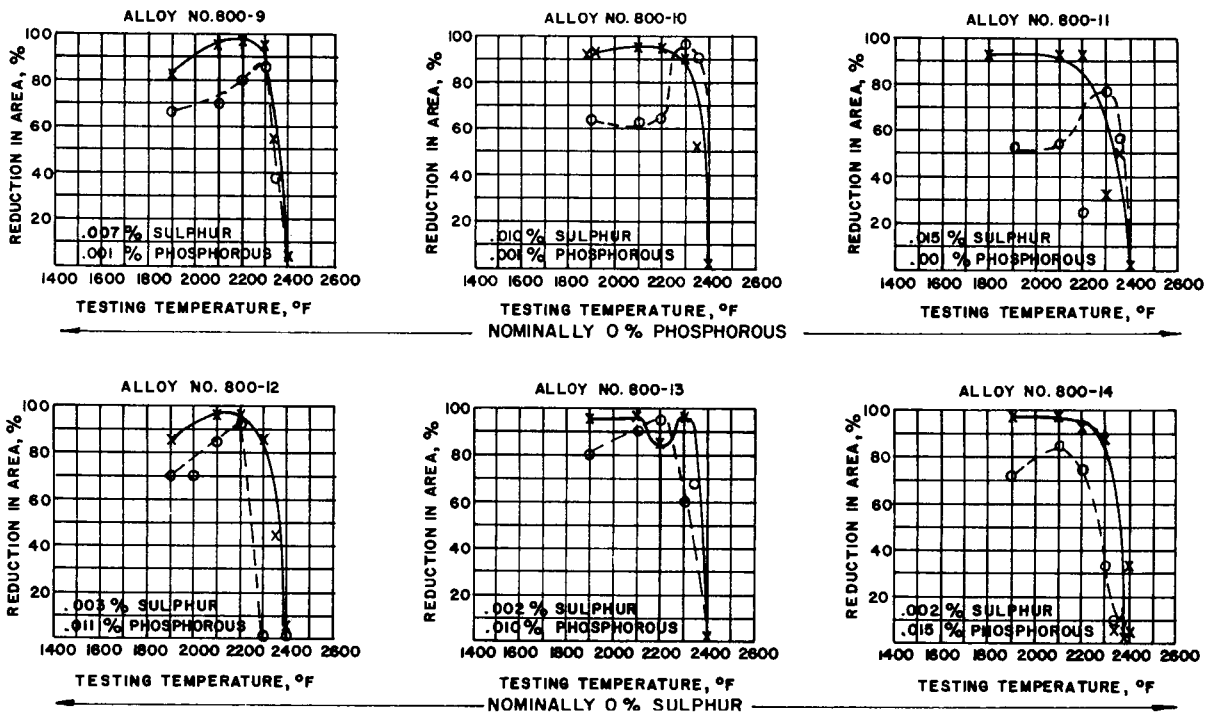

Fig. 7.3. The Individual Effect of Sulfur and Phosphorus on the Hot Ductility of the Experimental Incoloy 800 Alloys (Nominally 0.38% Al and 0.38% Ti).

ORNL-DWG 67-13978

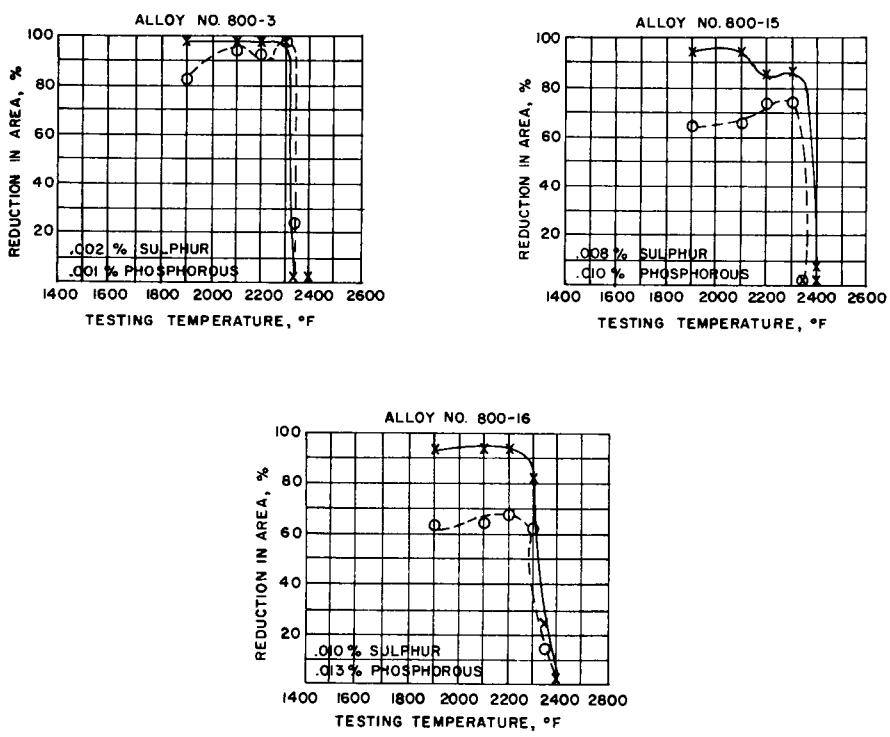

Fig. 7.4. The Combined Effect of Sulfur and Phosphorus on the Hot Ductility of the Experimental Incoloy 800 Alloys (Nominally 0.38% Al and 0.38% Ti).

[redacted]

[redacted]

Table 7.1. The Free Energy of Formation[a] for Various Sulfides

Compound	Temperature (°K)	Free Energy of Formation (cal/mole)
Al_2S_3	298.15	−65,670
FeS	298.15	−32,640
MgS	298.15	−92,900
MnS	298.15	−59,300
NiS	298.15	−30,700
TiS	298.15	−60,700

[a]Per mole of sulfur.

negate the bad effects of sulfur in iron-base alloys. Since the free energy of formation of Al_2S_3 and TiS is similar to that of MnS, it is felt that these elements may be tying up the sulfur in our special alloys.

Figure 7.5 shows the effect of titanium plus aluminum additions on the ZST of the experimental alloys. As expected, this temperature decreases with increasing alloying content, reflecting localized melting.

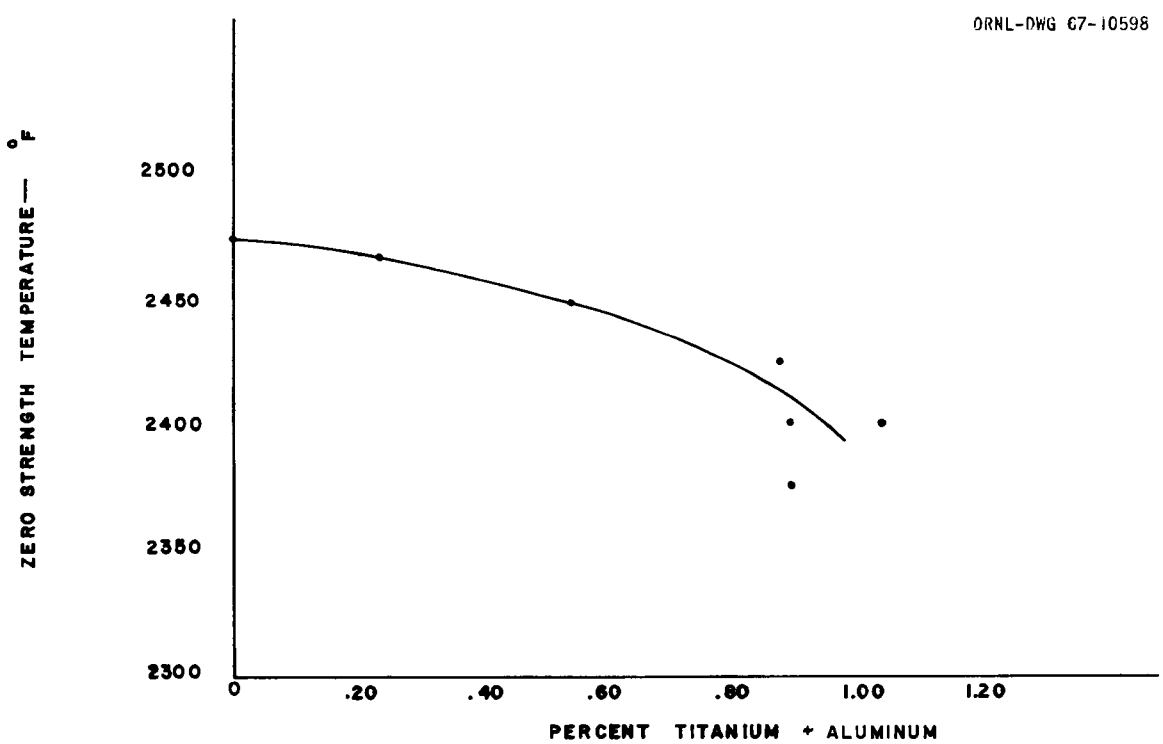

Fig. 7.5. Effect of Titanium Plus Aluminum on the Zero Strength Temperature of the Experimental Incoloy 800 Alloys.

[redacted]

[redacted]

Figure 7.6 shows the effect of sulfur, phosphorus, and sulfur plus phosphorus on the ZST of titanium- and aluminum-bearing Incoloy 800 alloys. As can be seen from the figure, there is no apparent systematic effect. This may be due to compound formation as previously discussed.

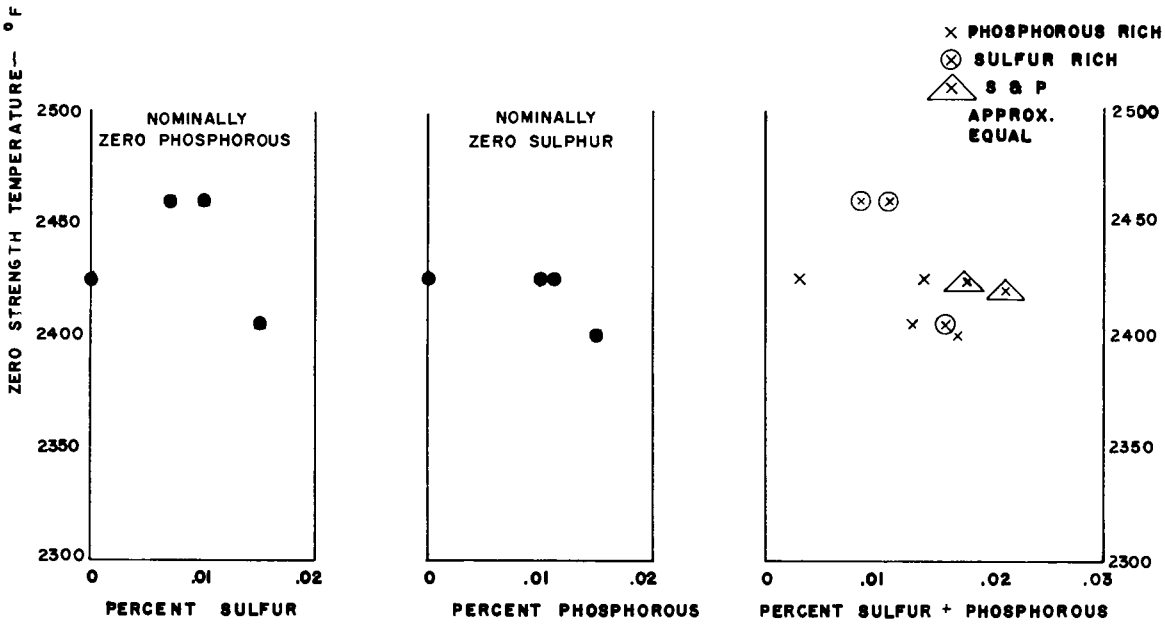

Fig. 7.6. Effect of Sulfur and Phosphorus on the Zero Strength Temperature of the Experimental Incoloy 800 Alloys. The experimental alloys contained from 0.63 to 0.80% Ti plus aluminum.

VARESTRAINT Testing Performed Under Subcontract at Rensselaer Polytechnic Institute[4]

W. F. Savage[4] C. D. Lundin[4]

VARESTRAINT studies[5] were continued on the influence of titanium and aluminum additions on the hot-cracking behavior of Incoloy 800.

---

[4]Department of Materials Engineering, Rensselaer Polytechnic Institute, Troy, N. Y. Subcontract is funded jointly with BONUS Core II Superheater Research and Development.

[5]W. F. Savage and C. D. Lundin, Welding J. (N.Y.) 44(10), 433-s–442-s (1965).

[redacted]

[redacted]

Figure 7.7 shows the results of the tests conducted to date plus the average data for two commercial heats of material. There is no apparent correlation between aluminum content, titanium content, or titanium plus aluminum content, and susceptibility toward hot cracking as determined by the VARESTRAINT test. About all that can be said at this point is that the cracking tendencies of the aluminum- and titanium-doped alloys fall in a range between the commercial material and the pure ternary alloy.

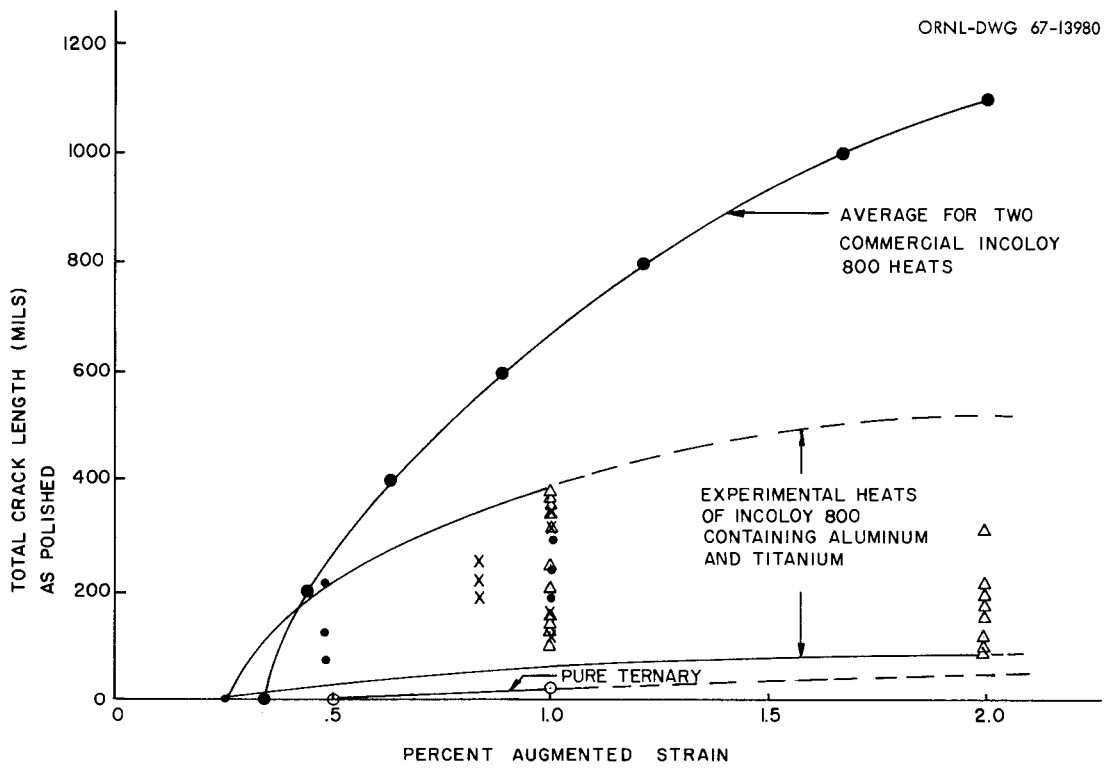

Fig. 7.7. VARESTRAINT Results for the Experimental Heats of Incoloy 800 Composition. The results of two commercial heats have been included for comparison.

The difference between the special alloys doped with aluminum and titanium and the commercial materials is felt to be due to the additional residuals in the commercial materials and/or melting and fabrication practices. Studies are continuing in an effort to explain these differences.

[redacted]

[redacted]

[redacted]

[redacted]

PART II.

REACTOR CHEMISTRY DIVISION

[redacted]

[redacted]

[redacted]

[redacted]

FISSION-GAS RELEASE AND PHYSICAL PROPERTIES OF FUEL MATERIALS DURING IRRADIATION

R. M. Carroll R. B. Perez[1]
G. W. Watson J. G. Morgan
O. Sisman

Fission-gas release from UO_2 is being studied in an effort to determine the mechanism by which the gas migrates and escapes from the fuel. From these studies we hope to develop a model to make engineering calculations of noble gas escape from operating fuel materials. Our experimental method is to irradiate carefully selected and characterized specimens in an irradiation facility where the neutron flux and temperature are controlled independently. Fission gas released from the specimen is entrained in a moving stream of sweep gas and carried outside the reactor where it is analyzed by gamma-ray spectrometry.

A defect-trap model of fission-gas release has been developed and two methods are used to evaluate the coefficients of the model. One is the steady-state method, wherein the gas release is measured while irradiation conditions are constant. In the other method, the specimen is oscillated sinusoidally in the reactor so as to oscillate the neutron flux and the specimen temperature. Waves of fission-gas release are produced by the oscillations, and analyses of these waves add a considerable degree of freedom in fitting a model to the data.

This perturbation method offers promise of being a good way to measure thermal diffusivity during irradiation since the time lag between a change of fission heating and the resultant change of temperature depends on the thermal diffusivity of the specimen. For this reason, hollow-cylinder specimens of single-crystal and fine-grain UO_2 have been used to develop the instrumentation and techniques for in-reactor thermal diffusivity measurements.

---

[1]Consultant from the University of Florida.

[redacted]

[redacted]

Steady-State Fission-Gas Release from UO_2
Single-Crystal Specimen Cl-19

After a total burnup of about 8×10^{19} fissions/cm^3, we reported previously[2] that the activation energy of fission-gas release suggested that the release was mainly by the migration of clusters rather than by individual atoms or small defect traps. This theory was substantiated by the pattern of gas release during the cooling of the specimen (see Fig. 1).

[2]R. M. Carroll, R. B. Perez, J. G. Morgan, and O. Sisman, Fuels and Materials Development Program Quart. Progr. Rept. June 30, 1967, ORNL-TM-1941, p. 84.

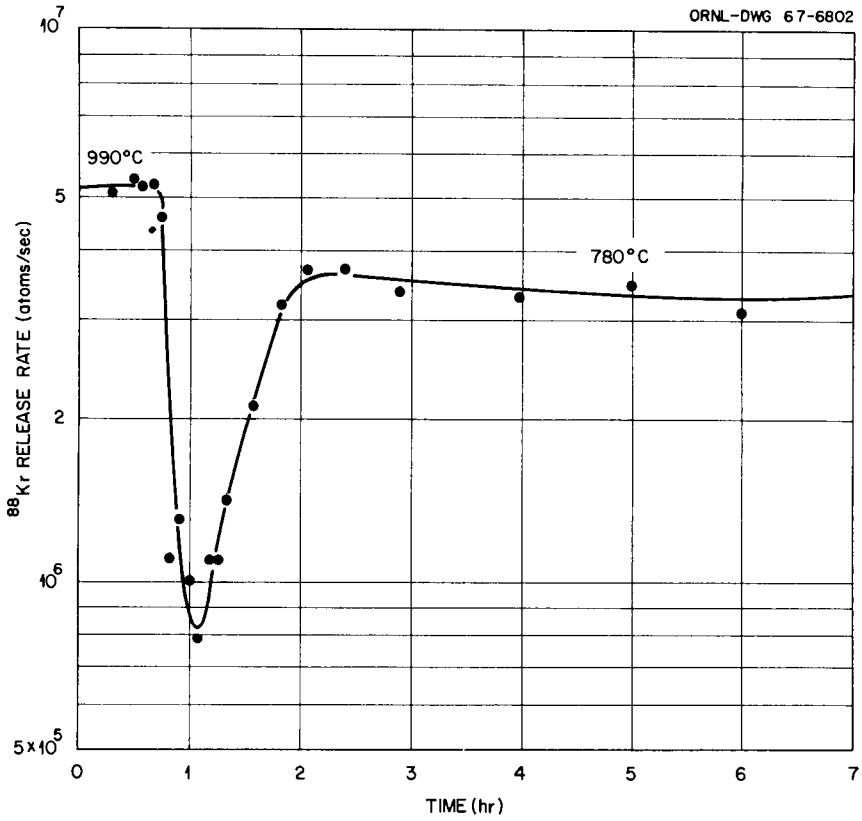

Fig. 1. Release of ^{88}Kr when Temperature of Single-Crystal UO_2 Specimen (Cl-19) was Reduced from 990 to 780°C at Constant Neutron Flux (After 8×10^{19} fissions/cm^3).

[redacted]

[redacted]

In our past experience, when a UO_2 specimen is cooled, the release decreases smoothly to its new steady-state level without any oscillation. This observation was one of the reasons we did not believe the gas release was by a pure diffusion process. By diffusion theory, a heating burst is caused by a change of concentration gradients. By the same token, when a specimen is cooled we would expect a reversible change of concentration gradient and an inverse burst, or dip, in the gas release. Such a gas-release pattern is shown in Fig. 1 and this, along with activation energy mentioned above, indicates the gas is being released by the diffusion of clusters.

The Cl-19 specimen has now been examined for changes of microstructure during irradiation. Figure 2 shows an as-polished 200× section of the specimen. The gas bubbles appear mainly clustered along subgrain boundaries. We think that the high operating temperature (1700°C) toward the end of the irradiation has caused the segregation of the gas bubbles. The same section of specimen is shown after light etching in Fig. 3 and after heavier etching in Fig. 4. After the etching, worm-like

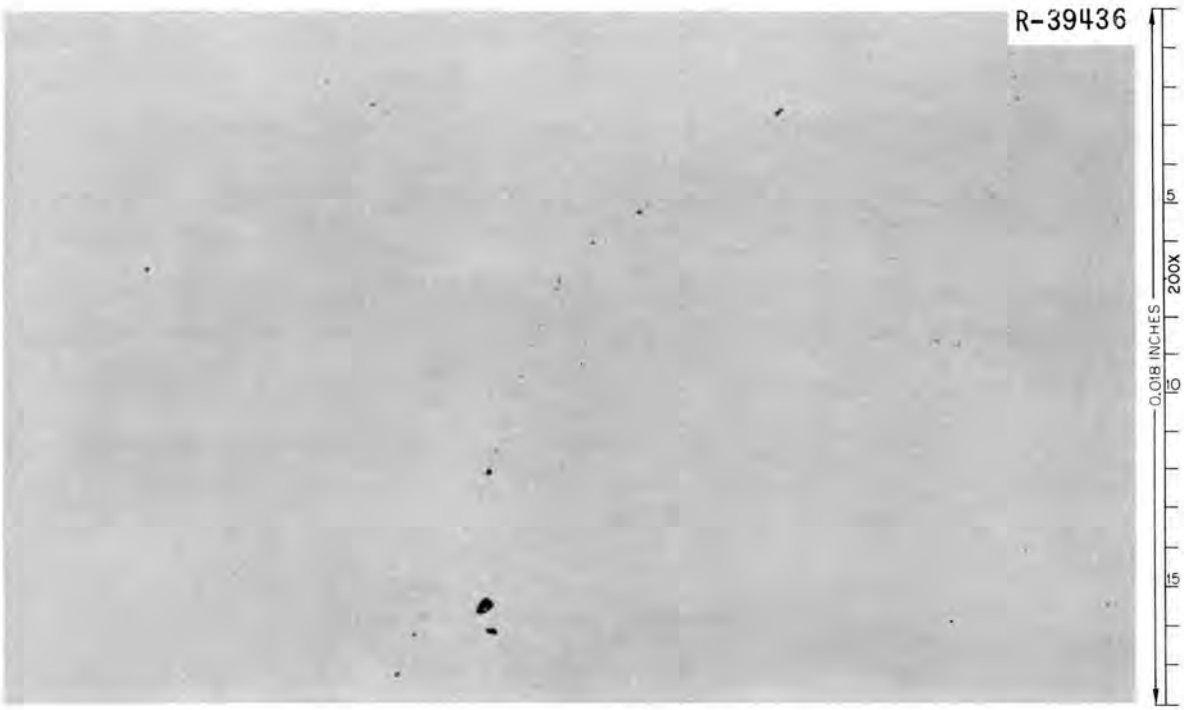

Fig. 2. Single-Crystal Specimen Cl-19. As polished.

[redacted]

[redacted]

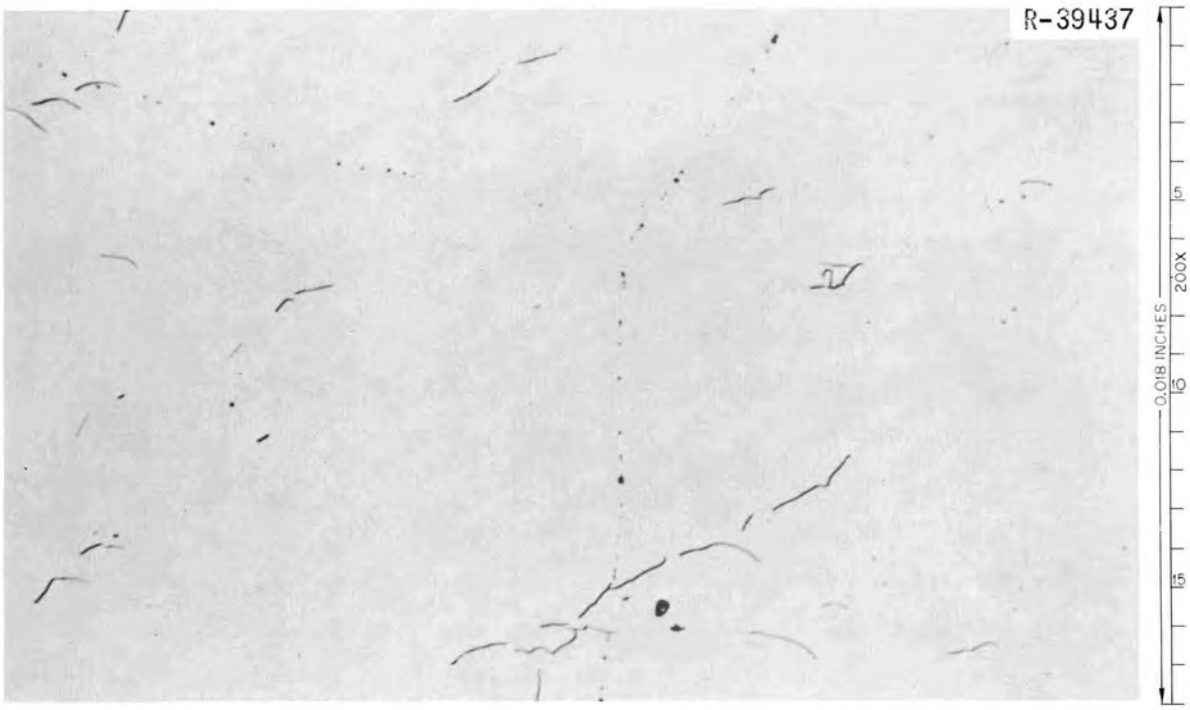

Fig. 3. Single-Crystal Specimen Cl-19, Lightly Etched. Etchant: 70% H_2O, 20% H_2O_2 (30% concd), and 10% HNO_3.

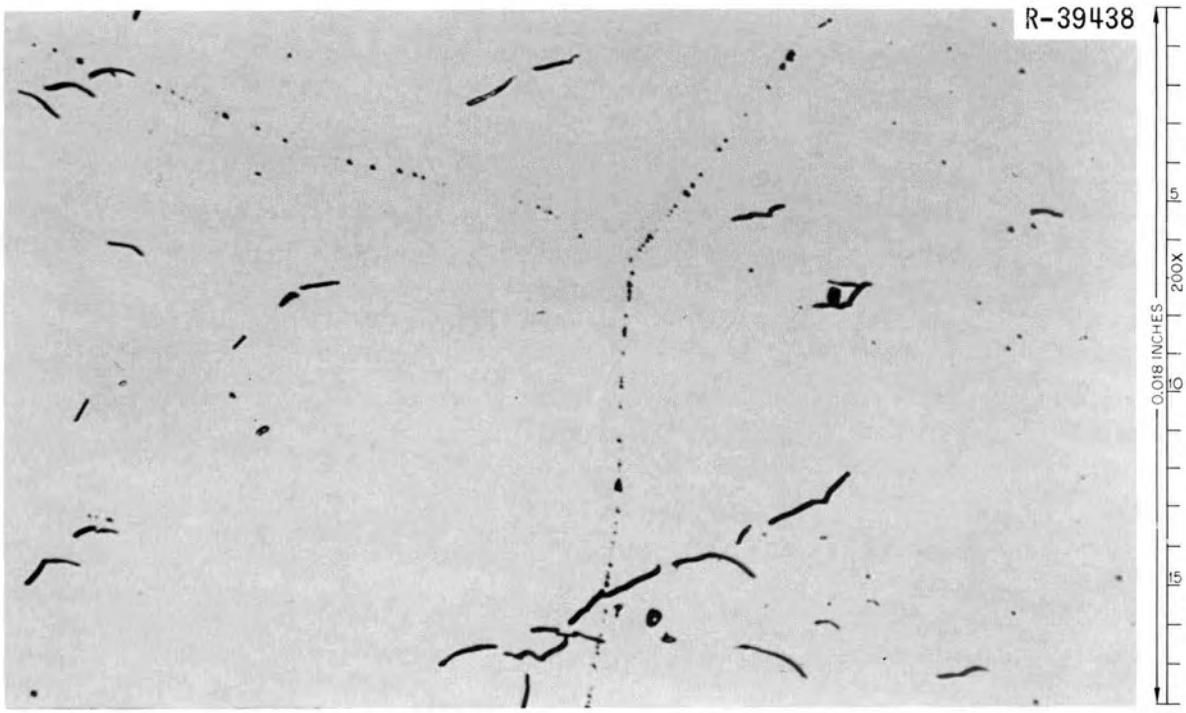

Fig. 4. Single-Crystal Specimen Cl-19, More Heavily Etched. Etchant: 70% H_2O, 20% H_2O_2 (30% concd), and 10% HNO_3.

[redacted]

voids were revealed, yet the bubbles along the subgrain boundary were not much enlarged. This suggests that the worm-like tracks were regions of intense lattice strain. It seems likely that these represent large defect traps of an interstitial nature extending into the interior of the specimen. The diffusion nature of the gas release may have been caused by diffusion of the gas within the trap to escape at the trap-surface interface.

Steady-State Fission-Gas Release from Fine-Grain UO_2 Specimen C1-20

The C1-20 specimen is almost the same as the C1-19 specimen, except for being of sintered fine-grain structure rather than single crystal. It is a hollow cylinder, 1.125 in. long, 0.235 in. OD, with an 0.134-in.-ID hole and a total weight of 5.85 g. One of the objectives in this test was to irradiate the specimen at temperatures high enough to cause grain growth and void migration. Although we think we saw evidence of cluster migration in the single-crystal specimen, grain growth could not be observed, and the gas release showed a constant activation energy at temperatures up to 1700°C.

The fine-grain specimen behaved in a more conventional manner. At the beginning of irradiation the gas release decreased as burnup progressed. This initial decrease of gas release is believed to be caused by a smoothing process.[3] After the gas release was constant with time, the fission gas had the temperature dependence shown in Fig. 5 as "initial data." Later in the irradiation the gas release from the specimen suddenly increased by about 40%. We interpreted this as being caused by the specimen breaking and increasing the surface area by about 40%. The increased gas release is shown in Fig. 5 as "after breaking."

We found that the low-temperature gas release (< 600°C) is mainly by a knockout process which is proportional to the total surface area

---

[3]R. M. Carroll and O. Sisman, "In-Pile Fission-Gas Release from Single-Crystal UO_2," Nucl. Sci. Eng. 21, 147–158 (1965).

[redacted]

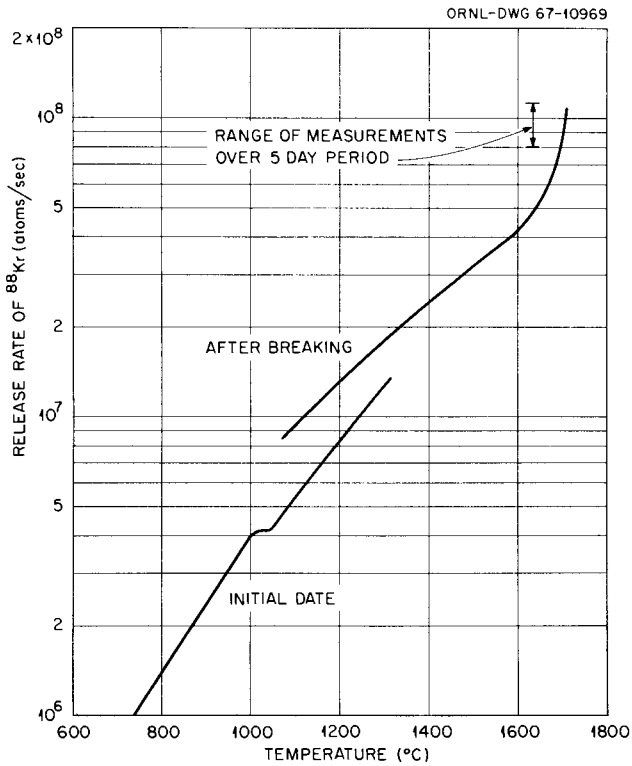

Fig. 5. The ^{88}Kr Release from Fine-Grain UO_2, Specimen Cl-20.

of a specimen. The fine-grain specimen released as much ^{88}Kr for a given neutron flux as did the single-crystal specimen Cl-19 (see Fig. 6). This indicated that the fine-grain specimen (before breaking) had about the same surface area as the single-crystal specimen, although the single-crystal specimen was broken. Thus, after the fine-grain specimen broke, it would have about 40% more surface area than the single-crystal specimen.

Even though the fine-grain specimen had a 40% larger surface area and lower density (98.4% of theoretical) than the single-crystal specimen, it released less fission gas at temperatures below 1600°C (see Fig. 7). This implies that grain boundaries act as traps. The grain-boundary trapping has been observed on other specimens and is consistent with the defect-trap model.[4]

---

[4]R. M. Carroll and O. Sisman, "In-Pile Fission-Gas Release from Fine-Grain UO_2," J. Nucl. Mater. 17, 305–312 (1965).

[redacted]

[redacted]

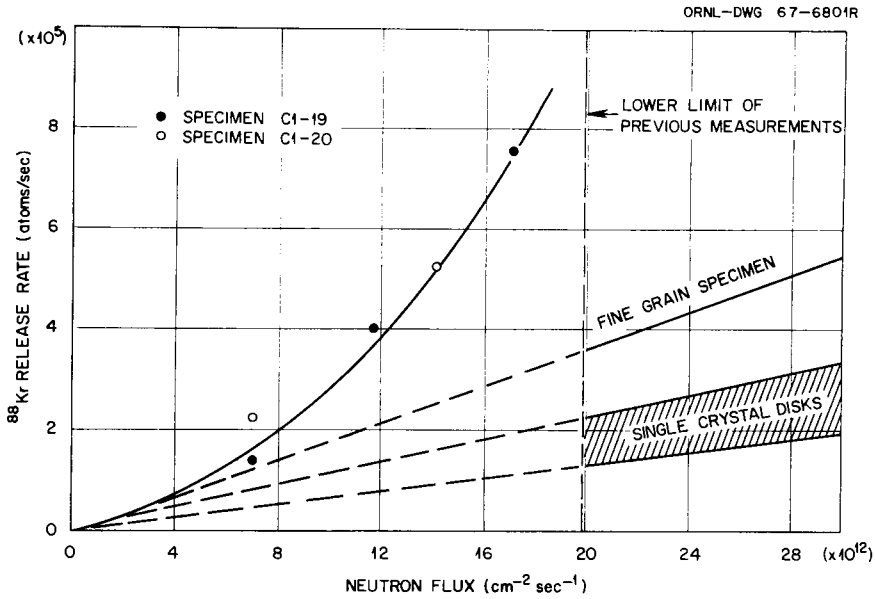

Fig. 6. Comparison of Surface Recoil from Fine-Grain Specimen C1-20 (Intact) with Single-Crystal Specimen C1-19 (Broken).

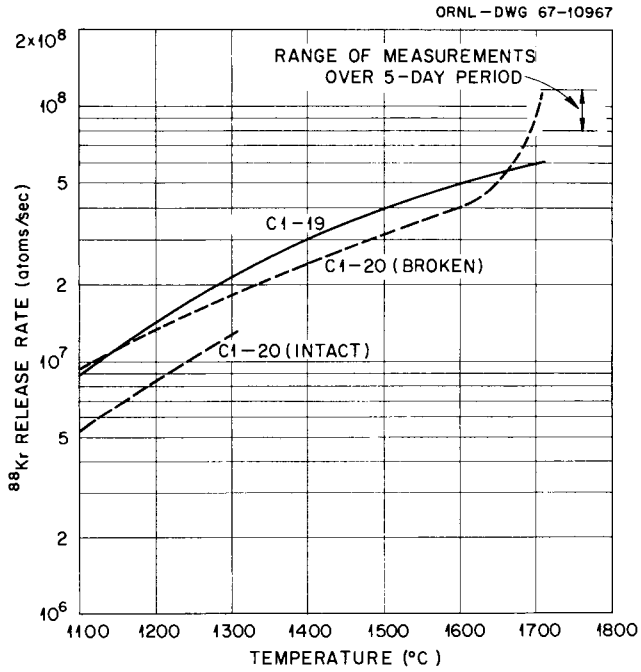

Fig. 7. Comparison of High-Temperature Release from Single-Crystal (C1-19) and Fine-Grain (C1-20) Specimens of UO_2.

[redacted]

In the past we have assumed that grain-boundary movement would be significant at 1600°C. At higher temperatures, the movement of grain boundaries and large defects would be expected to release a major portion of the fission gas. After such an alteration of the microstructure of the specimen, the gas release would be different if the specimens were irradiated again at lower temperatures.

The fine-grain specimen was irradiated at 1630°C for 5 days, and during this time there was no change of gas-release rate such as would have been expected for grain growth. The amount of gas released at 1630°C was the same as would be predicted by extrapolating the gas-release rate at lower temperatures. This indicated that the release mechanism was the same at 1630°C as for lower temperatures. After the 1630°C run, the gas release at lower temperatures was the same as we had measured before. We thus conclude that sweeping grain growth does not occur at 1600°C.

Recently we have operated the fuel specimen at 1700°C for 5 days. Here we did find that a gradual increase of fission-gas release occurred as the run progressed. There were also short bursts of activity that occurred during steady-state conditions. The span of fission-gas activity at 1700°C is shown in Fig. 5, and the relation of the 1700°C release to the previous data shows clearly that another release mechanism is operating at 1700°C.

At first it appeared that the sharp bursts of gas at steady-state conditions indicated large defect traps arriving at the specimen surface and releasing the stored fission gas; for example, a sweeping grain boundary could cause the burst as it reached the specimen surface. These bursts were not observed for the single-crystal specimen. However, these bursts were also observed when the fine-grain specimen was withdrawn from the reactor and was at a temperature of about 200°C (see Fig. 8).

Since some bursts of gas did occur at temperatures much too low for defect migration, we speculate that they are caused by microcracks in the UO_2 generated by localized high-pressure concentrations of fission gas. For example, the decay of iodine concentrated in a defect could increase the xenon pressure within a trap causing a crack that would

[redacted]

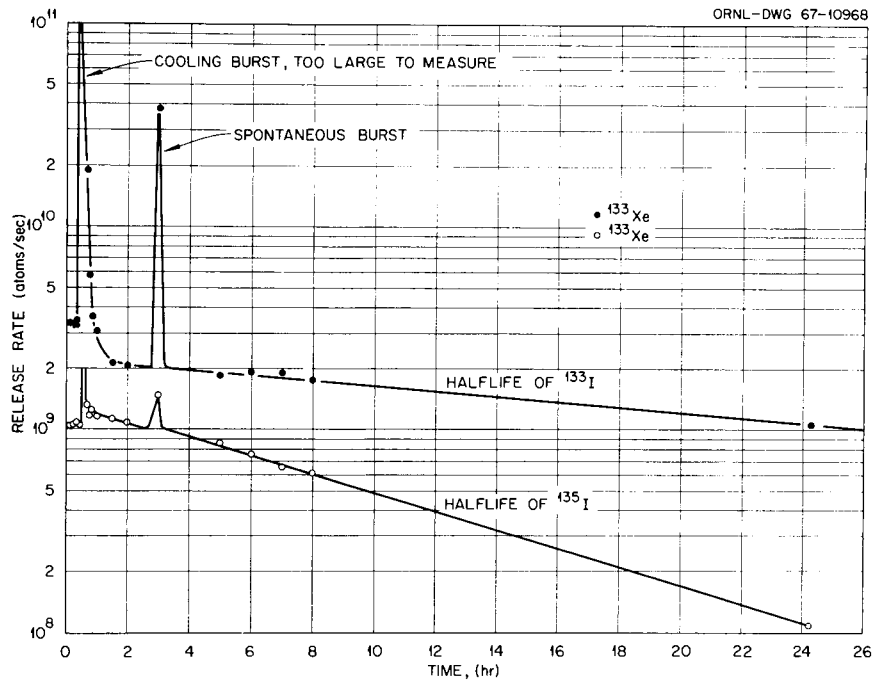

Fig. 8. Xenon-133 and Xenon-135 Release when Fine-Grain Specimen C1-20 was Withdrawn from Neutron Flux after 5 Days Irradiation at 1700°C ($\phi = 6.0 \times 10^{13}$).

allow the gas to escape. Apparently a high-temperature (≈ 1600°C) irradiation is necessary to allow the gas to concentrate in bubbles or at existing defects. These bursts have never been observed for lower temperature irradiations (< 1500°C).

After the 1700°C irradiation, measurements were made at lower temperatures to see if the 1700°C run had caused irreversible damage. Only one run has been made to date, at 1140°C, but the ^{88}Kr release is now lower than before the 1700°C run. The first measurements correspond to that listed as "initial data" on Fig. 5.

Cooling Bursts and Iodine Release

It is fairly rare for us to see a burst of gas being released when a specimen is cooled and the usual explanation is that the specimen has suffered a change of structure during the temperature drop. The type

[redacted]

of large burst shown in Fig. 8 has been explained by Rothwell[5] as the transformation of $UO_{2.0-x}$ (which is supposed to exist at high temperatures) to $UO_{2.0}$+U(metal). If, however, the cooling burst of Fig. 8 was caused by the combination of internal pressure and thermal stresses during cooling to cause microcracks, the cause would be consistent with our explanation for the spontaneous burst after the specimen had been cooled for several hours (see Fig. 8).

The cooling burst also released iodine from the fuel. The amount of ^{133}I was more than expected, based on lower temperature measurements. The ^{135}Xe release caused by the decay of ^{135}I is actually more after the cooling burst than the combined ^{135}Xe release from iodine decay plus gaseous escape before withdrawing the sample from the reactor. This means that iodine as well as rare gases must be released in the cooling bursts.

Computer Program for Defect-Trap Model

The computer program designed to fit the parameters of the defect-trap model to the experimental data has been written and checked. The program was run through the computer once and is now being investigated to obtain a feel for the value of the adjustable parameters.

An additional program is being developed for idealized inputs. The perfect data, although fictional, will serve to define the model and be a check for the program. After checking the idealized data, we will start processing actual data.

---

[5]E. Rothwell, "The Release of ^{85}Kr from Irradiated Uranium Dioxide on Postirradiation Annealing," J. Nucl. Mater. 5(2), 241–249 (1962).

[redacted]

PART III

SOLID STATE DIVISION

[redacted]

[redacted]

[redacted]

[redacted]

IRRADIATION EFFECTS ON ALLOYS AND STRUCTURAL MATERIALS

D. S. Billington, M. S. Wechsler, and J. T. Stanley

The major emphasis of research in the Radiation Metallurgy Section is the study of radiation hardening and radiation embrittlement in the bcc metals and alloys. These metals have in common the tendency toward low temperature brittleness which can be characterized by the ductile-brittle transition temperature. The increase in ductile-brittle transition temperature upon irradiation is of concern in reactor technology because of the possible catastrophic failure of reactor pressure vessels in service.

At the present time our attention is directed toward three materials: pressure vessel steels, iron, and niobium. In the pressure vessel steels, we are concluding our study of ASTM A-212 Grade B steels and are initiating experiments on more advanced types, such as ASTM A-533, Grade B, Class 1 and ASTM A-517, Grade E. Of particular interest is the weld heat-affected-zone microstructure. Sudden brittle fractures of steel vessels have been known to originate at the heat-affected zones adjacent to welds in large steel structures; one such case was reported recently.[1] In order to simulate the heat-affected-zone microstructure, a thermal cycling treatment based on actual weld characteristics is used.

However, to delve deeper into the mechanism of radiation embrittlement in pressure vessel steels, we are conducting experiments on high-purity iron with controlled additions of interstitial solutes. Special emphasis is given to the role of nitrogen, since experiments

[1] "Case History, Brittle Fracture of a Thick-Walled Pressure Vessel," Nucl. Engineering 11, p. 368 (1966).

[redacted]

have indicated that iron alloys and steels undergo greater radiation embrittlement[2,3,4] and radiation hardening[5,6] when the free nitrogen content is high. Tensile tests and resistivity measurements on irradiated vacuum-melted iron with and without nitrogen additions are described in this report. In general it is felt that complexes formed by the trapping of interstitial solute atoms at radiation produced defects play an important part in the radiation hardening and embrittlement. This is indicated by the observation that little hardening takes place upon low temperature irradiation, but when the iron alloy is heated into the temperature range where the interstitials are mobile, the hardening sets in.[7] Furthermore, internal friction measurements have indicated that the release of nitrogen from radiation-produced traps occurs in the same temperature range (300 - 400°C) as for the annealing of the radiation-induced increase in

---

[2] M. Castagna, A. Ferro, F. S. Rossi, and J. Sebille, "On the Effect of Nitrogen on the Mechanical Properties of Neutron Irradiated Pure Iron," in The Effects of Radiation on Structural Metals, ASTM-STP, American Society for Testing and Materials, Philadelphia, 1967 (Proceedings of a symposium at Atlantic City, June 29-July 1, 1966).

[3] F. S. Rossi and M. Castagna, "On the Influence of Some Killing Elements on the Mechanical Properties of Neutron Irradiated Iron," in Proceedings of the Colloquium on Brittle Fracture and Safety Problems in Nuclear Pressure Vessels, EUR 3121.d,f,e, pp. 391-410, Euratom, Brussels, 1966.

[4] R. L. Colombo, F. S. Rossi, and J. Sebille, "The Effect of Nitrogen on the Radiation Embrittlement of Iron," Solid State Communications 4, 55 (1966).

[5] P. J. Barton, D. R. Harries, and I. L. Mogford, "Effects of Dose Rate and Irradiation Temperature on Radiation Hardening in Mild Steels," J. Iron Steel Inst. 203, 507 (1965).

[6] D. R. Harries and B. L. Eyre, "Effects of Irradiation in Iron and Steels," in Flow and Fracture of Metals and Alloys in Nuclear Environments ASTM-STP-380, pp. 105-119, American Society for Testing and Materials, Philadelphia, 1965.

[7] N. E. Hinkle and N. K. Smith, "Tensile Tests on Irradiated Iron," Radiation Metallurgy Section Solid State Division Progress Report for Period Ending Jan. 1967, ORNL-4097, April 1967, p. 7.

yield stress.[8] For pressure vessel steels, 300°C is also the temperature above which radiation embrittlement is reduced, as is shown in this report and in the previous one.[9]

Another bcc metal, niobium, is also being investigated; it may be prepared in high-purity and in single crystal form. For the first time, radiation-produced defect clusters have been observed for niobium in the electron microscope.[10] As is described below, a dose of 2×10^{18} neutrons/cm^2 (E > MeV) produced about 5×10^{15} damage clusters per cm^3. The phenomenon of dislocation channeling was also observed, in which dislocations set in motion by plastic deformation appear to clear a channel free of defect clusters. The nature of the defect clusters is being studied by electron microscopy and by resistivity and internal friction measurements. As in the case of iron, interstitial solutes exert a great influence on the effects observed. In the case of niobium, interstitial oxygen is particularly important, and considerable evidence has been accumulated which shows that the so-called Stage III annealing stage is due to the motion of oxygen to radiation-produced defects.[11] An analysis of the kinetics indicates that the defects at which the oxygen atoms are trapped are small radiation-produced dislocation loops.[12]

---

[8] N. E. Hinkle, S. M. Ohr, and M. S. Wechsler, "Dose Rate, Annealing, and Stress-Relaxation Studies of Radiation Hardening in Iron," in The Effects of Radiation on Structural Metals, ASTM-STP, American Society for Testing and Materials, Philadelphia, 1967 (Proceedings of a symposium at Atlantic City, June 29-July 1, 1966).

[9] R. G. Berggren, W. J. Stelzman, and T. N. Jones, "Radiation Effects on Pressure Vessel Steels," Radiation Metallurgy Section Solid State Division Progress Report for Period Ending Jan. 1967, ORNL-4097, p. 1.

[10] R. P. Tucker and S. M. Ohr, "Direct Observation of Neutron Irradiation Damage in Niobium," Phil. Mag., to be published.

[11] J. M. Williams, W. E. Brundage, and J. T. Stanley, "The Effect of Oxygen on 'Stage III' Annealing in Neutron-Irradiated Niobium," submitted for publication.

[12] R. Bullough, J. T. Stanley, and J. M. Williams, "The Kinetics of Migration of Impurities to Small Dislocation Loops," submitted for publication.

The connection between the trapping of oxygen and radiation hardening in niobium is being pursued. One point being investigated is the possibility that the radiation-anneal hardening observed by Makin and Minter[13] upon annealing irradiated niobium is due to the motion of oxygen, as is suggested by the similarity of the activation energies observed in our experiments and by the above authors.

The nature of the hardening agents in irradiated iron and niobium is being investigated by yield stress measurements as a function of test temperature and strain rate and by stress relaxation experiments. The results described below indicate, in contrast to F.C.C. metals, that the temperature and strain rate dependence of the yield stress is not greatly changed by the irradiation, thus indicating no important change in the rate-controlling mechanism of plastic flow.

Dislocation dynamics in unirradiated and irradiated niobium is also being studied by means of an etching technique. A direct determination of the stress dependence of dislocation velocity has been carried out and some preliminary results are described below for neutron-irradiated samples. Several indirect techniques are also being employed, and attempts are underway to establish a correlation between the various results.

Radiation Effects on Pressure-Vessel Steels

R. G. Berggren W. J. Stelzman
T. N. Jones

A. Effects of Irradiation Temperature and Post-Irradiation Annealing

Our studies of the effects of fast neutron dose, irradiation temperature, and post-irradiation recovery on the Charpy V-notch ductile-brittle transition temperature of ASTM A-212 Grade B steels (base plate and synthetic heat-affected zones) have been completed, and we are now starting

[13] M. J. Makin and F. J. Minter, "The Mechanical Properties of Irradiated Molybdenum," Acta Met. 7, 361 (1959).

similar studies on ASTM A-533, Grade B, Class 1 and ASTM A-517 Grade E (Armco SSS 100). These are steels currently being used for pressure vessel construction or being considered for future use. We have previously reported on the effects of neutron dose and irradiation temperature on the Charpy V-notch transition temperature of three ASTM A-212 Grade B base plate and heat-affected zone samples[9,14,15] and some data were reported on post-irradiation recovery of transition temperature.[14] Typical results of the post-irradiation recovery studies, including new data, are shown in Fig. 1. The number of irradiated specimens available for post-irradiation recovery studies was limited. In order to obtain the greatest possible information from the limited number of specimens, as few as two specimens were annealed at each temperature.

The results are summarized in Table 1 and in Figs. 2 and 3 where the change in ductile-brittle transition temperature, ΔDBTT, is plotted versus irradiation temperature or post-irradiation annealing temperature. The measured ΔDBTT was in each case converted to equivalent ΔDBTT at a neutron dose of 9×10^{18} n/cm^2 (E > 1 MeV) using the trend line for A-212 Grade B steel.

The figures show that the ΔDBTT decreases quite rapidly with increasing temperature of irradiation in a narrow temperature interval around 300°C. Post-irradiation recovery of the transition temperature occurs in a temperature range above 300°C for 100 minute anneals, but the recovery temperature should move towards lower temperatures with longer annealing times.

The large amount of scatter in the results shown in Figs. 2 and 3 is a matter of some concern. This scatter apparently comes from various sources: 1) The normalization of the data to a common dose according

---

[14] R. G. Berggren, W. J. Stelzman, and T. N. Jones, "Radiation Effects on Pressure-Vessel Steels," Radiation Metallurgy Section Solid State Division Progress Report for Period Ending February 1966, ORNL-3949, May 1966, p. 2.

[15] R. G. Berggren, W. J. Stelzman, and T. N. Jones, "Radiation Effects on Pressure-Vessel Steels," Radiation Metallurgy Section Solid State Division Progress Report for Period Ending July 1966, ORNL-4020, September 1966, p. 1.

[redacted]

ORNL-DWG 67-8821

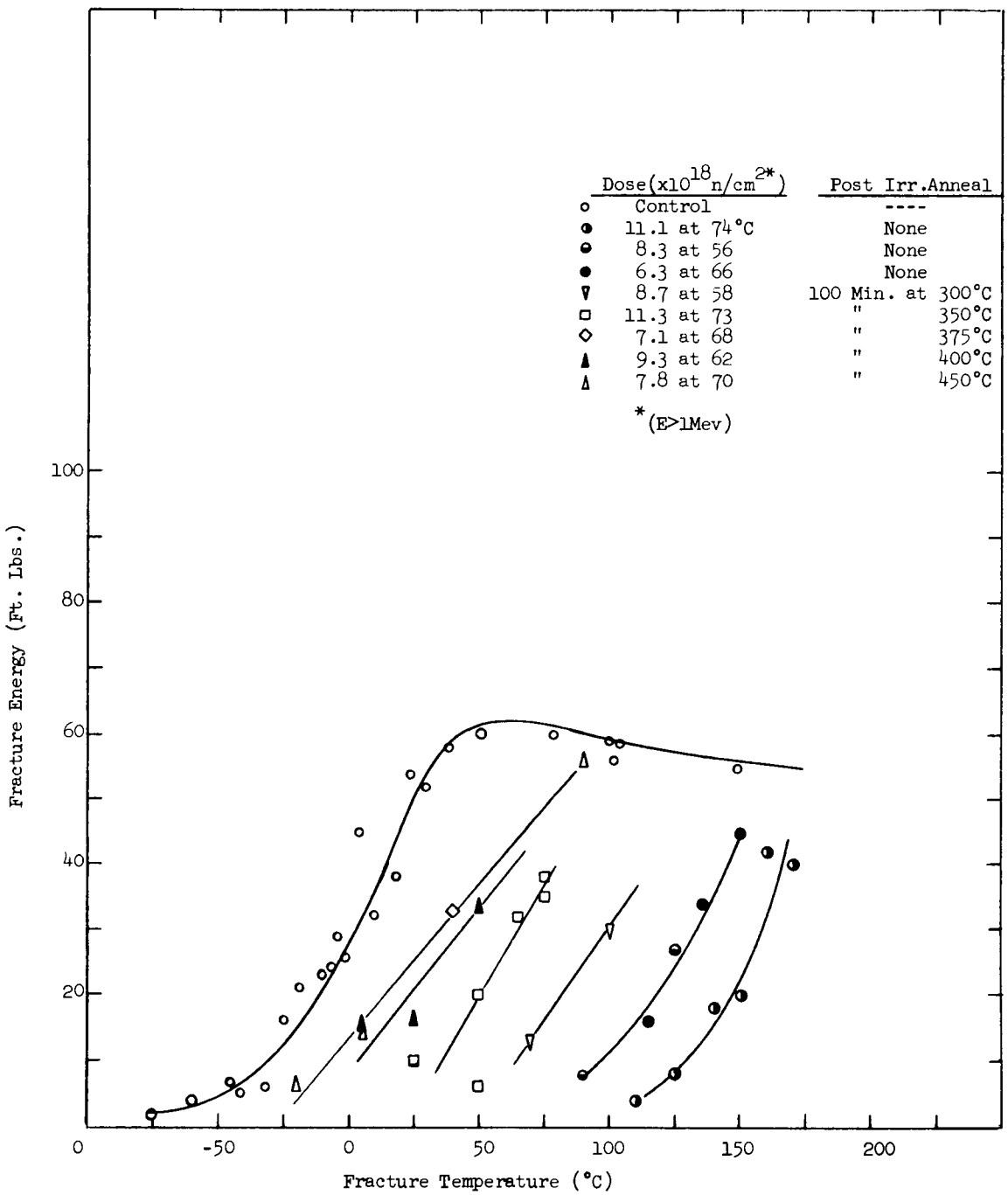

Fig. 1. Charpy V-Notch Fracture Energy vs Test Temperature for Unirradiated, Irradiated and Post-Irradiation-Annealed Base Plate Samples of ASTM A-212-B, Lukens Heat 2110, (SSD Item 156).

[redacted]

[redacted]

ORNL-DWG 67-8823

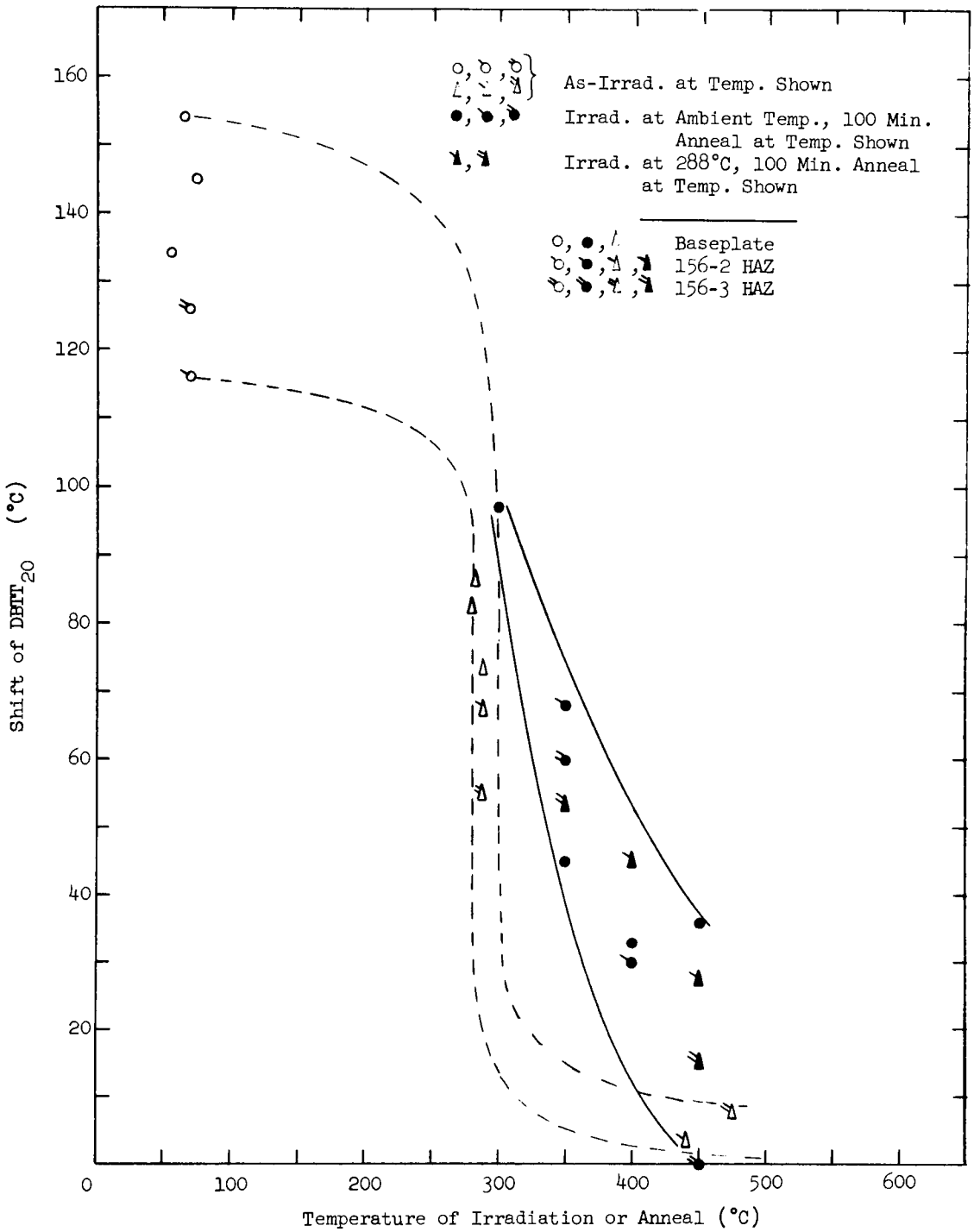

Fig. 2. Effect of Irradiation Temperature and Post Irradiation Anneal on Shift of Charpy V-Notch Transition Temperature of ASTM A-212-B, Lukens Heat 2110, (SSD Item 156) Base Plate and Heat-Affected-Zones.

[redacted]

[redacted]

ORNL-DWG 67-8822

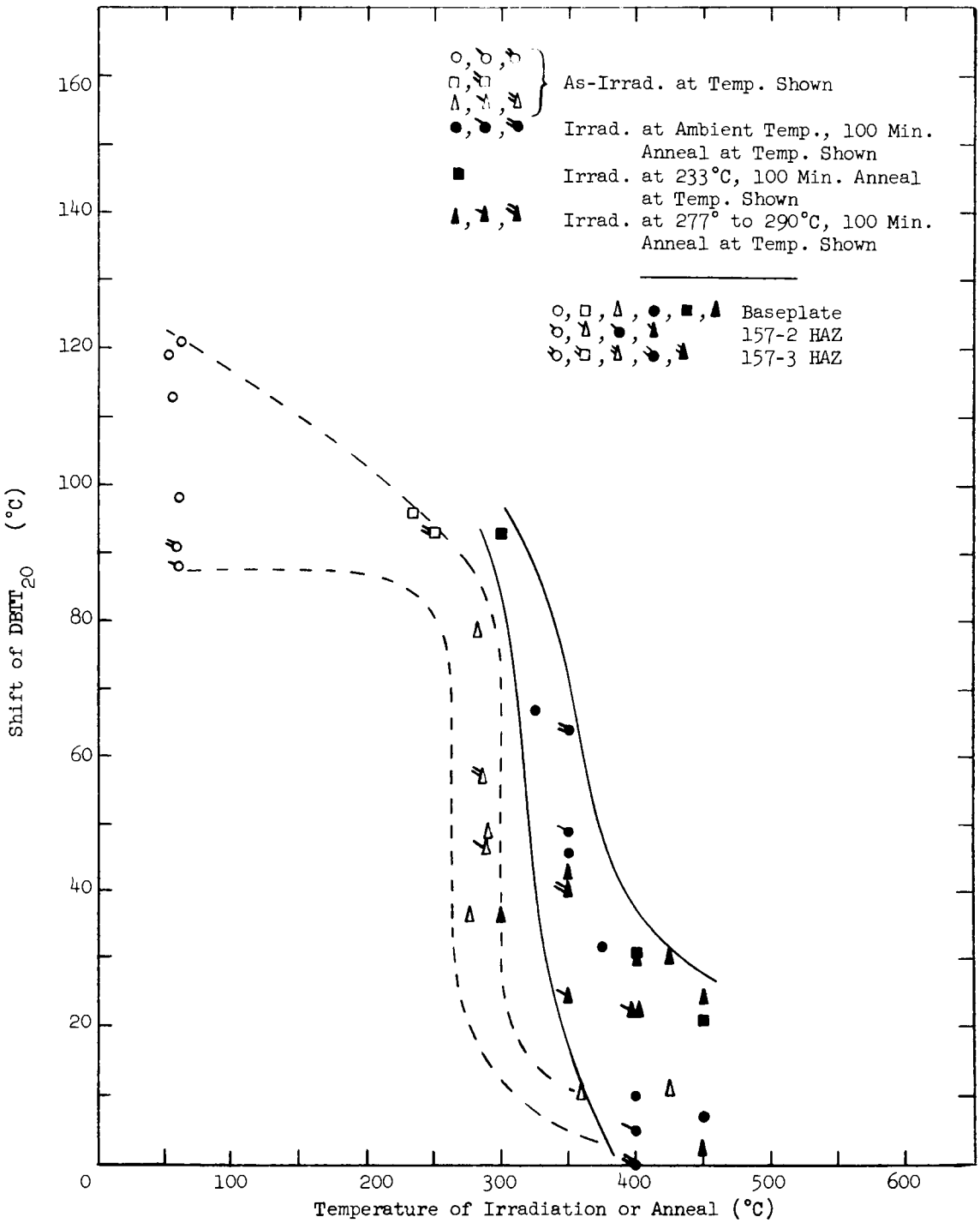

Fig. 3. Effect of Irradiation Temperature and Post Irradiation Anneal on Shift of Charpy V-Notch Transition Temperature of ASTM A-212-B, Lukens Heat 2056, (SSD Item 157) Base Plate and Heat-Affected-Zones.

[redacted]

Table 1. Effect of Post-Irradiation Annealing on Charpy V-Notch Ductile-Brittle Transition Temperature of ASTM A-212 Grade B Base Plate and Heat-Affected-Zone Specimens

SSD Item No.[16]	Irradiation Temp. (°C)	Irradiation Dose (E>1MeV) ($\times 10^{18}$ n/cm^2)	Post Irradiation Anneal Temp. (°C)	Post Irradiation Anneal Time (hr)	DBTT[a] (°C)	ΔDBTT[a] (°C)	ΔDBTT[a] Normalized to 9×10^{18} n/cm^2 (°C)	Fracture Appearance (Percent Fibrous) 25% (°C)	Fracture Appearance (Percent Fibrous) 50% (°C)
147 (Base Plate)	--	0	--	--	-20	--	--	-3	18
	--	--	482	1176	-25	-5	--	-13	15
	70	5	300	2.0	8	28	68	--	--
	70	7	350	2.0	-7	13	30	--	--
	333[b]	8	--	--	10	30	41	12	37
147-4B HAZ	--	0	--	--	-18	--	--	-35	8
	70	8	300	2.0	42	60	68	--	--
	340[b]	9	--	--	2	20	21	0	20
147-2B HAZ	--	0	--	--	60	--	--	52	78
	70	7	300	2.0	123	63	81	--	--
156 (Base Plate)	--	0	--	--	-12	--	--	-15	5
	65	6.3	--	--	118	130	154	98	115
	55	8.3	--	--	118	130	134	98	115
	60	8.7	300	1.67	82	94	97	70	87
	70	11.3	350	1.67	50	62	45	44	58
	60	9.3	400	1.67	23	35	33	13	37
	70	7.8	450	1.67	14	26	36	-2	14
156-2 HAZ	--	0	--	--	7	--	--	7	29
	288	8.8	400	1.67	50	43	45	38	67
	288	9.1	450	1.67	35	28	27	30	58
	70	9.1	350	1.67	76	69	68	67	88
	70	9.6	400	1.67	42	35	30	29	52

Table 1 (Cont'd.)

SSD Item No.[16]	Irradiation Temp. (°C)	Irradiation Dose (E>1MeV) ($x10^{18}$ n/cm^2)	Post Irradiation Anneal Temp. (°C)	Post Irradiation Anneal Time (hr)	DBTT[a] (°C)	ΔDBTT[a] (°C)	ΔDBTT[a] Normalized to $9x10^{18}$ n/cm^2 (°C)	Fracture Appearance (Percent Fibrous) 25% (°C)	Fracture Appearance (Percent Fibrous) 50% (°C)
156-3 HAZ	--	0	--	--	8	--	--	10	35
	288	9.6	350	1.67	65	57	53	64	93
	288	10.0	450	1.67	30	22	15	33	48
	70[b]	10.7	--	--	145	137	126	114	137
	70	10.7	350	1.67	81	73	60	75	98
	70	10.8	450	1.67	20	12	0	12	41
157 Base Plate	--	0	--	--	5	--	--	-6	11
	233	8	300	1.67	90	85	93	--	--
	233	8	400	1.67	28	23	31	--	--
	233	8	450	1.67	18	13	21	--	--
	277	11	300	1.67	55	50	36	--	--
	277	11	400	1.67	40	35	22	--	--
	277	11	425	1.67	30	25	11	--	--
	277	11	450	1.67	20	15	2	--	--
	55	6.0	--	--	90	85	113	67	80
	55	7.1	--	--	108	103	119	83	103
	55	7.6	325	1.67	60	55	67	43	58
	60	9.6	350	1.67	55	50	46	38	52
	55	6.5	375	1.67	15	10	32	12	28
	55	8.1	400	1.67	7	2	10	3	18
	55	6.9	450	1.67	-7	-12	7	-22	0
	280	6.3	--	--	59	54	78	47	63
	290	10.4	350	1.67	59	54	43	47	63
	290	10.0	400	1.67	43	38	30	27	56
	290	6.8	425	1.67	15	10	30	4	25
	285	7.4	450	1.67	23	18	24	4	25
	62	5.1[d]	--	--	85	80	121	63	82
	63	4.9[c]	--	--	85	80	121	63	82

Table 1 (Cont'd.)

SSD Item No.[16]	Irradiation Temp. (°C)	Irradiation Dose (E>1MeV) ($x10^{18}$ n/cm^2)	Post Irradiation Anneal Temp. (°C)	Post Irradiation Anneal Time (hr)	DBTT[a] (°C)	ΔDBTT[a] (°C)	ΔDBTT[a] Normalized to $9x10^{18}$ n/cm^2 (°C)	Fracture Appearance (Percent Fibrous) 25% (°C)	Fracture Appearance (Percent Fibrous) 50% (°C)
157-2 HAZ	--[b]	0	--	--	53	--	--	32	58
	60	8.3	--	--	135	82	88	108	131
	60	7.5	350	1.67	90	37	49	80	105
	60	8.8	400	1.67	56	3	5	43	67
	288	9.2	350	1.67	78	25	24	77	98
	288	8.1	400	1.67	68	15	22	58	85
157-3 HAZ	--	0	--	--	43	--	--	25	58
	55	9.2	350	1.67	108	65	64	96	113
	60	9.8	400	1.67	48	5	0	27	55
	249[b]	9.3	--	--	138	95	93	108	132
	290	10.3	350	1.67	93	50	40	86	108

(a) Ductile-Brittle Transition Temperature: 20 ft lb energy level.

(b) Previously reported, minor adjustments have been made as a result of additional tests.

(c) Shielded with 0.040 in. cadmium.

(d) Irradiated (unshielded) simultaneously with cadmium shielded experiment.

to a single trend band for all heats and conditions of heat treatment and irradiation is likely to be somewhat inaccurate, but at the present time there are not enough data points to establish a dose dependence for each condition of the steel. 2) Variations of composition and cooling rate from heat treatment temperatures occur within a single plate of steel so that ideally only specimens from similar positions in the plate should be compared.

B. Effect of Thermal Neutron Damage.

Thermal neutrons can produce radiation damage in steels since the iron nucleus gains a significant recoil energy from the emission of gamma rays after capture of a thermal neutron.[16] To see if this effect produces a significant amount of damage in our irradiations, we carried out an experiment with two sets of specimens. One set of specimens was shielded with 0.040 inches of cadmium, and the other was unshielded. Both sets contained Charpy V-notch specimens of an ASTM A-212 Grade B steel and an ASTM A-302 Grade B steel. Exposure temperature was 60°C. A cadmium ratio of 4:1 (cobalt monitors) and a thermal neutron to E > 1 MeV ratio of 7.5:1 has been previously measured for these positions. The results for the ASTM A-302 Grade B steel are presented in Table 2 and the results for the ASTM-212 Grade B steel appear in Table 1 as the last two entries under SSD Item No. 157, base plate. No significant effect of cadmium shielding on transition temperature shift was observed for either steel. The individual data points for the 1/3-thickness in the ASTM A-302 Grade B steel, plotted in Fig. 4, are typical of the inter-mingling of shielded and unshielded data. Thus, the study of thermal neutron irradiation effects on mechanical properties will undoubtedly require an almost pure thermal neutron flux.

[16] M. S. Wechsler, "Fundamental Aspects of Radiation Effects on Diffusion-Controlled Reactions in Alloys," Radiation Effects on Metals and Neutron Dosimetry, STP No. 341 p. 86 ASTM, Philadelphia, (1963).

[redacted]

ORNL-DWG 67-8820

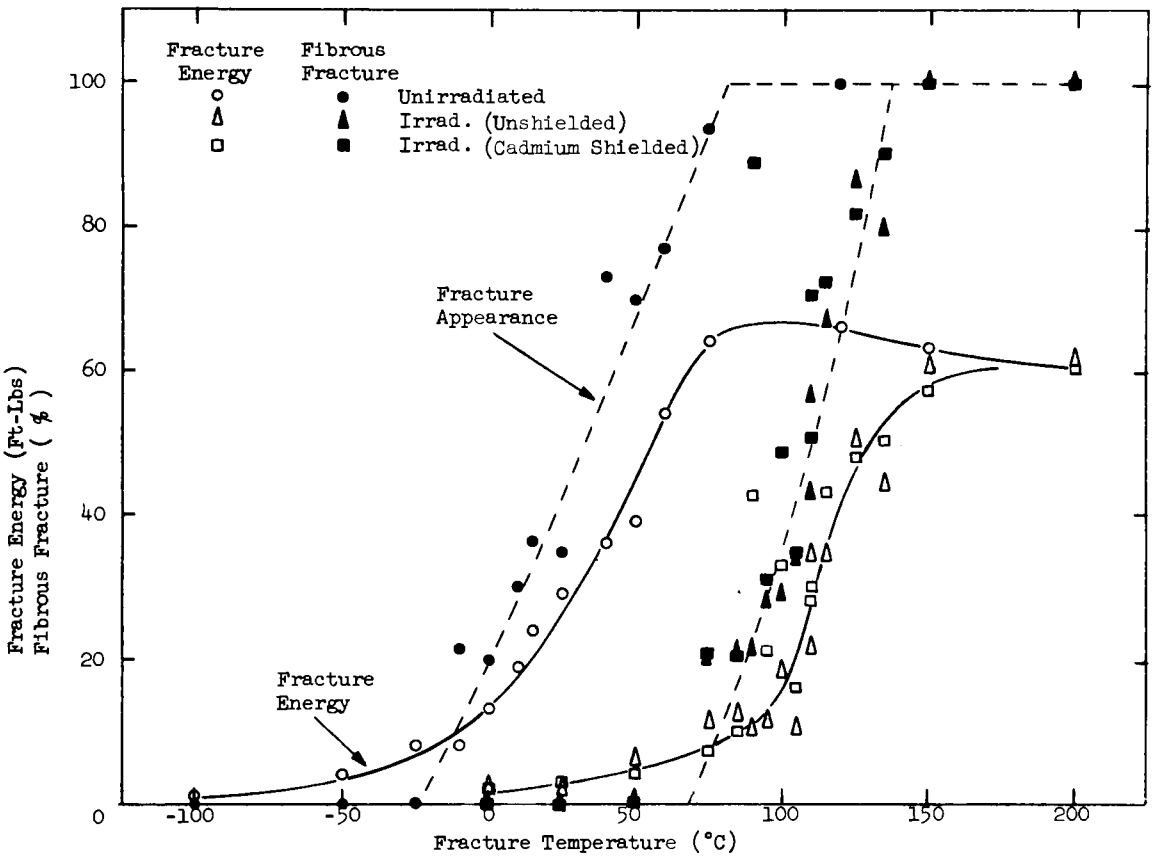

Fig. 4. Effect of Cadmium Shielding on Charpy V-Notch Impact Tests of A-302-B Steel Irradiated to 5.4×10^{-18} n/cm^2 at 50°C 1/3-Thickness Layer, Lukens Heat No. 21485 (SSD Item 127).

C. Fracture Appearance Measurements.

Fracture appearance measurements are now being made on all Charpy V-notch specimens (Tables 1 and 2 and Fig. 4). The fracture faces are photographed, enlarged, and the brittle fracture area measured by planimeter. We have generally found less "scatter" in fracture appearance data than in fracture energy data. The fracture appearance has provided a check on the accuracy of the fracture energy data. The intercepts of the fracture appearance curve with 0% and 100% ductile appearance are well defined. We have also made lateral expansion measurements on the same specimens and find much greater scatter of data than for either fracture appearance or fracture energy.

[redacted]

[redacted]

Table 2. Effect of Irradiation on Charpy V-Notch Ductile-Brittle Transition Temperature of 8 1/2 in ASTM A-302-B Plate, Lukens Heat 21485,[a] Irradiated at 60°C (SSD Item 127).

Specimen Location	Irradiation Dose (E > 1 MeV)	DBTT (30 ft-lb)	ΔDBTT	ΔDBTT Normalized to 5×10^{18} n/cm^2	Fracture Appearance (Percent fibrous) 25%	50%
	($\times 10^{18}$ n/cm^2)	(°C)	(°C)	(°C)	(°C)	(°C)
Surface	0	15	--	--	22	43
Surface	4.3[b]	87	72	82	64	94
Surface	4.0[b]	87	72	86	64	94
1/4 T	0	20	--	--	0	23
1/4 T	4.3[b]	96	76	86	78	98
1/4 T	4.4[b]	96	76	81	78	98
1/3 T	0	30	--		5	32
1/3 T	5.4[b]	112	82	77	92	110
1/3 T	5.3[b]	112	82	78	92	110

(a) Normalized at 1650°F for 1 hr/in of thickness, fan cooled, stress relieved at 1200°F for 1 hr/in of thickness, fan cooled.

Mill Analysis (%)

C	Mn	P	S	Si	Mo
0.19	1.36	0.020	0.025	0.26	0.48

(b) Shielded with 0.040 in. cadmium.

[redacted]

Effect of Interstitial Solutes on Radiation Hardening in Iron

N. E. Hinkle W. E. Brundage
J. M. Williams J. T. Stanley

Introduction

It has been shown[17,18] that a vacuum-melted iron (Ferrovac E), annealed at 815°C and furnace cooled, is strengthened by 10-minute anneals at temperatures between 0 and 100°C following irradiation to a neutron dose of 7.8×10^{16} n/cm^2 at −130°C. This behavior of irradiated metals, which has been termed "thermal hardening," was also observed by Makin and Minter[19] in niobium, by Wronski and Johnson[20] in molybdenum, and by Moteff[21] in tungsten and molybdenum. The thermal hardening in these metals occurs at about 15 percent of their absolute melting temperatures (0.15 T_M). Post-irradiation resistivity recovery experiments by Nihoul[22] on molybdenum, by Peacock and Johnson[23] on molybdenum and niobium, and by Williams, et al.[24] on niobium, also showed a recovery peak at about

---

[17] M. S. Wechsler, "Fundamental Aspects of Radiation Effects on Diffusion-Controlled Reactions in Alloys," Radiation Effects on Metals and Neutron Dosimetry, STP No. 341 p. 86 ASTM, Philadelphia, (1963).

[18] N. E. Hinkle and N. K. Smith, "Tensile Tests on Irradiated Iron," Radiation Metallurgy Section Solid State Division Progress Report for Period Ending Jan. 1967, ORNL-4097, April 1967, p. 7.

[19] M. J. Makin and F. J. Minter, "The Mechanical Properties of Irradiated Molybdenum," Acta Met. 7, 361 (1959).

[20] A. S. Wronski and A. A. Johnson, "A Hardening Effect Associated with Stage III Recovery in Neutron Irradiated Molybdenum," Phil. Mag. 8, 1067 (1963).

[21] J. Moteff, "Radiation Damage in Body-Centered Cubic Metals and Alloys," Radiation Effects in Materials, Gordon and Breach, New York, 1966.

[22] J. Nihoul, "The Recovery of Radiation Damage in Molybdenum," Phys. Stat. Sol. 2, 308 (1962).

[23] E. E. Peacock and A. A. Johnson, "Stage III Recovery in Neutron Irradiated Molybdenum and Niobium," Phil. Mag. 8, 563 (1963).

[24] J. M. Williams, J. T. Stanley, and W. E. Brundage, "The Interaction of Radiation Produced Defects and Interstitial Impurity Atoms in Niobium," Radiation Metallurgy Section Solid State Division Progress Report for Period Ending Jan. 1967, ORNL-4097, April 1967, p. 30.

0.15 T_M. The study on niobium[24] indicated that this resistivity recovery peak is caused by the removal of interstitial oxygen from solid solution. Wuttig, Stanley, and Birnbaum,[25] using the magnetic aftereffect technique, found that both nitrogen and carbon are removed from solution in iron in the temperature range of 30°C to 80°C (0.16 T_M to 0.20 T_M), the same region where thermal hardening is observed.[18]

In studies bearing more heavily on engineering properties, McRickard and co-workers,[26,27] using low temperature tensile tests, showed that iron irradiated at 70°C exhibited a marked decrease in ductility at −140°C, but for irradiations at 0°C or −70°C no embrittlement occurred. It was suggested that the difference in the low temperature tensile characteristics of iron as a function of irradiation temperature is due to the presence of carbon which migrates to irradiation-induced defects at an irradiation temperature of 70°C and forms embrittling defects. Colombo et al.[28] in impact tests on Fe-N and Fe-Ti samples concluded that when the nitrogen is removed from solid solution by forming titanium nitrides, there is a significant decrease in the amount of radiation embrittlement. However, the carbon present in the iron-nitrogen samples may have also played a part in the observed embrittlement.

---

[25] M. Wuttig, J. T. Stanley, and H. K. Birnbaum, "Interstitial Solute Trapping in Irradiated and Quenched Iron," submitted for publication.

[26] S. B. McRickard, "Effect of Low Temperature Radiation on Embrittlement of Iron," Quarterly Progress Report: Irradiation Effects on Reactor Structural Materials, Aug., Sept., Oct., 1965, BNWL-CC-355, pp. 5.2 and 5.3 Dec., 1965.

[27] S. B. McRickard and J. G. Y. Chow, "Effect of Irradiation on the Mechanical Properties of Iron," Quarterly Progress Report: Irradiation Effects on Reactor Structural Materials, May, June, July, 1966, BNWL-CC-784, pp. 5.3 and 5.4 Aug., 1966.

[28] R. L. Colombo, F. S. Rossi, and J. Sebille, "The Effect of Nitrogen on the Radiation Embrittlement of Iron," Solid State Communications 4, 55 (1966).

Studies by Hawthorne et al.[29] suggest that a decrease in the concentration of substitutional and interstitial residual elements leads to reduced susceptibility to brittle fracture of pressure vessel steels.

Although there are suggestions in the literature that point defects are responsible for the recovery stage at 0.15 T_M,[30,20] other studies have emphasized the importance of interstitial impurities[18,22,24,25,26] on the radiation hardening of body-centered cubic metals. However, definitive experiments that relate the mechanical property changes with the interstitial concentrations in solution have not been performed. These experiments are needed to obtain an understanding of the mechanism of the interaction between interstitial atoms and radiation produced defects. Therefore, an investigation was begun to determine which interstitials contribute to the thermal hardening and the radiation embrittlement in iron and to understand the basic mechanisms involved. This information might lead the way to changes in the chemistry of steelmaking which would minimize or eliminate the problem of radiation embrittlement.

The present study combines measurements of resistivity, internal friction, magnetic aftereffect, and tensile properties. The resistivity, internal friction, and elastic aftereffect measurements give indications of the concentrations and distributions of interstitial solutes. Thus, a determination of these properties in conjunction with determinations of mechanical properties elucidates the role of interstitials in radiation hardening.

Material

The starting material for this study was Ferrovac-E iron of 1-1/4 inch diameter bar stock. The iron was swaged to 1/16 inch diameter and decarburized in hydrogen at 800°C for about 96 hours. The decarburized iron

---

[29] J. R. Hawthorne, C. Z. Serpan, Jr., H. E. Watson, and R. A. Gray, Jr., "Experimental Heats of A-302-B Steel Found Insensitive to Radiation Embrittlement at 550°F," Quarterly Progress Report: Irradiation Effects on Reactor Structural Materials, Nov., Dec., 1966-Jan. 1967, BNWL-CC-1053, pp. 9.1 to 9.4 Feb. 15, 1967.

[30] M. J. Makin and F. J. Minter, "The Mechanical Properties of Irradiated Molybdenum," Acta Met. 7, 361 (1959).

was further swaged and finally drawn to 0.050 inch diameter and cut to the following lengths: 2-1/4 inches for resistivity samples, 3-3/4 inches for internal friction samples, and 1-1/2 inches for tensile samples. The shoulders of the tensile samples were fabricated by cold-upsetting the ends of the 1-1/2 inch long wire blank in a double-ended, hydraulically-operated die.

The samples were heat-treated for four hours in hydrogen at 700°C and 800°C followed by furnace cooling to establish grain sizes of 35 μ and 130 μ respectively. Samples of each grain size were further heat-treated at 590°C for ten hours and quenched in water. In this heat treatment, one group of samples of both grain sizes was nitrided in a hydrogen-ammonia atmosphere; a second control group was treated in a pure hydrogen atmosphere. The concentration of nitrogen as determined by internal friction measurements was 15-20 ppm by weight for the nitrided samples and less than 1 ppm for the control samples. The carbon content was below 2 ppm as determined by internal friction measurements and confirmed by measurements of the magnetic after effect.

Irradiation

The neutron irradiations were performed in a liquid-nitrogen-cooled cryostat located adjacent to the ORNL Bulk Shielding Reactor.[31] The neutron flux in this facility was about 3×10^{12} n/cm^2 sec (E > 1 MeV) as calculated from the disintegration rate of nickel dosimeters assuming a threshold cross section of 420 mb, a threshold energy of 2.9 MeV, and a fission spectrum. The irradiation assemblies consisted of a cluster of nine (or less) thin-walled cadmium tubes held together with aluminum end plates. The samples placed within the cadmium tubes were shielded from about 99 percent of the thermal neutrons, thus decreasing the induced activity by about two orders of magnitude. The activity of an iron resistivity sample a couple of weeks after the irradiation was about 10 mr/hr. The sample temperatures were continuously monitored

[31] B. C. Kelley and C. E. Klabunde, "Irradiation Facilities in the Oak Ridge National Laboratory Bulk Shielding Reactor," Proceedings of the International Symposium on Developments in Irradiation Capsule Technology, Pleasanton, Calif., May 3-5, 1966. TID-4500 (Conf.--660511).

using copper-constantan thermocouples.

Four fully-loaded assemblies, containing 20 tensile, q resistivity, and 3 internal friction samples were irradiated to a dose of 4×10^{17} n/cm^2 (E > 1 MeV) at temperatures ranging between −50 and −90°C. One partially-loaded assembly containing 12 tensile samples and two resistivity samples was irradiated to a dose of 1.1×10^{18} n/cm^2 (E > 1 MeV) at temperatures between −75 and −95°C. Samples of both nitrogen contents and grain sizes were irradiated, but results for only the smaller grain-size samples are discussed.

Following the irradiation, the assemblies were removed from the irradiation facility without exceeding the irradiation temperature and stored in liquid nitrogen for a radioactivity decay period. Then the assemblies were taken apart in a liquid nitrogen bath, and the samples were stored in liquid nitrogen until testing commenced.

Results

Post-irradiation isochronal annealing measurements were made on the resistivity samples. The resistivities were measured in liquid helium with and without a magnetic field. No differences in the annealing spectrum were observed as a function of the magnetic field. Figure 5 shows the derivative of the resistivity annealing curve from −30°C to 390°C for the iron of both nitrogen concentrations, irradiated to a dose of 4×10^{17} n/cm^2 (E > 1 MeV). Unirradiated control samples were step annealed and measured simultaneously with the irradiated samples and show no change in the resistivity up to 400°C. The most outstanding feature of the curves in Fig. 5 is the large peak centered at 35°C for the iron-nitrogen sample. It is believed that this peak is due to the removal of nitrogen from solid solution by forming complexes with radiation-produced defects. This conclusion is supported by internal friction measurements on a sample from the same irradiation; it was found that the nitrogen was completely removed from solution in about 12 hours at 26°C, whereas previous studies of unirradiated iron-nitrogen indicated no change in the nitrogen concentration at this temperature. Minor peaks are also seen for the Fe-N curve in Fig. 5 on either side of the peak at 35°C. However, a discussion of these and other features

[redacted]

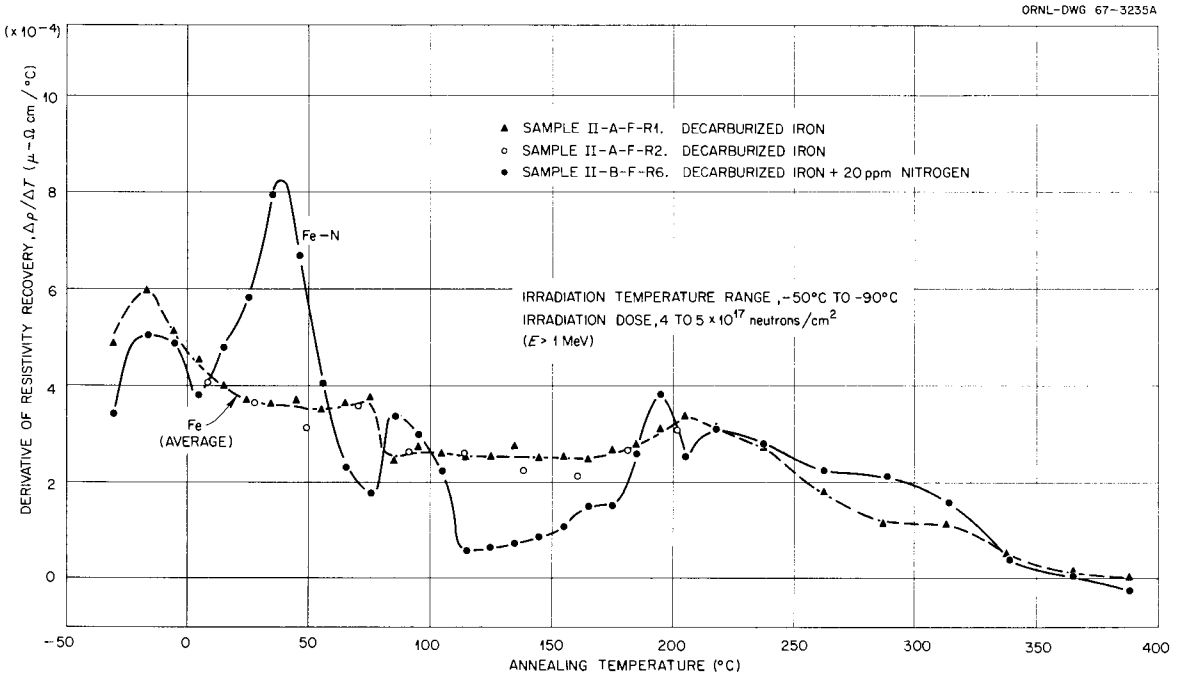

Fig. 5. Derivative of the Isochronal Recovery of Resistivity After Dose of 4×10^{17} n/cm^2 (E > 1 MeV) as a Function of the Annealing Temperature for Decarburized Iron and for the Decarburized Iron Plus about 20 ppm (by weight) Nitrogen. The Annealing Time at Each Temperature was 15 Minutes up to 225°C and 30 Minutes Above 225°C. The Measurements Were Made in Liquid Helium at a Magnetic Field of 0.6 to 0.8 Kilogauss.

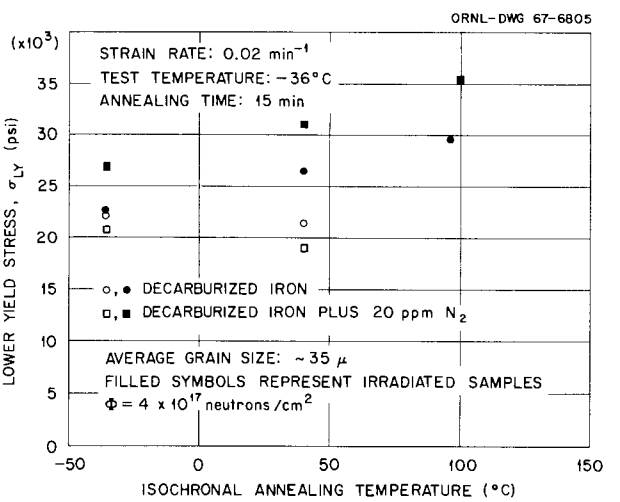

Fig. 6. Lower Yield Stress at −36°C and a Strain Rate of 0.02 min.$^{-1}$ as a Function of Annealing Temperature After a Neutron Dose of 4×10^{17} n/cm^2 (E > 1 MeV) at −50°C to −90°C for Decarburized Low Nitrogen (< 1 ppm) Iron and for Decarburized Iron Containing About 20 ppm Nitrogen. Annealing Time was 15 Minutes.

[redacted]

of the annealing spectrum will be deferred until further results are available

Concerning the effect of irradiation at sub-ambient temperatures on tensile properties, it was shown in a previous report (Fig. 9, Ref. 18) that little hardening is observed upon irradiation at −130°C, but that the increase in yield stress will set in upon post-irradiation annealing in the temperature range from 0°C to 150°C. Additional experiments of this type have now been carried out on the iron tensile samples with low nitrogen content (< 1 ppm) and with about 20 ppm nitrogen. Figure 6 shows that for both types of samples post-irradiation annealing following irradiation at −50°C to −90°C gives rise to an increase in yield stress for anneals between −40°C and 100°C. No such increase in yield stress is observed for the unirradiated samples. However, these measurements are still underway and further results will be reported subsequently.

Observation of Neutron Irradiation Damage in Niobium by Transmission Electron Microscopy

R. P. Tucker* and S. M. Ohr

Although direct observations by transmission electron microscopy of damage resulting from neutron bombardment have been reported for a number of b.c.c. metals, e.g. iron,[32-35]

---

*Oak Ridge Graduate Fellow from the University of Tennessee under appointment from Oak Ridge Associated Universities.

[32] B. L. Eyre, "Direct Observations of Neutron Irradiation Damage in α-Iron," Phil. Mag. 7, 2107 (1962).

[33] B. C. Masters, "Dislocation Loops in Irradiated Iron," Phil. Mag. 11, 881 (1965).

[34] B. L. Eyre and A. F. Bartlett, "An Electron Microscope Study of Neutron Irradiation Damage in Alpha-Iron," Phil. Mag. 12, 261 (1965).

[35] J. S. Bryner, "A Study of Neutron Irradiation Damage in Iron by Electron-Transmission Microscopy," Acta Met. 14, 323 (1966).

molybdenum,[36-40] and tungsten,[41] similar results for niobium have not not been available. A report of the first direct observations of neutron damage in niobium and a preliminary evaluation of the characteristics of the damage are given here. A similar account will be published in the open literature[42].

Materials and Experimental Procedures

The niobium used in this study was obtained as a powder from CIBA Limited and was particularly attractive for irradiation studies because of its relatively low tantalum and tungsten contents. The niobium powder was compacted and subsequently grown into single crystal rods by the passage of an electron-beam induced molten zone.[+] To prepare samples suitable for electron microscopy, the rod was rolled to a thickness of 0.005 inch and then was given a recrystallization anneal at 1050°C for one hour in a vacuum of approximately 3×10^{-8} torr. Following the recrystallization anneal, analysis gave the impurities by weight as: Ta, 20 ppm; W, 10 ppm; C, 60 ppm; N, 5 ppm; H, 2 ppm, and O, 38 ppm.

---

[36] M. E. Downey and B. L. Eyre, "Neutron Damage in Molybdenum," Phil. Mag. 11, 53 (1965).

[37] J. D. Meakin and I. G. Greenfield, "Interstitial Loops in Neutron Irradiated Molybdenum," Phil. Mag. 11, 277 (1965).

[38] B. Mastel and J. L. Brimball, "The Combined Effect of Carbon and Neutrons Radiation on Molybdenum," Acta Met. 13, 1109 (1965).

[39] B. L. Eyre and M. E. Downey, "The Influence of Irradiation Temperature on the Damage Structure in Neutron-Irradiated Molybdenum," Metal Science Journal 1, 5 (1967).

[40] P. Rao and G. Thomas, "Defects in Neutron Irradiated Molybdenum," Acta Met. 15, 1153 (1967).

[41] K. Lacefield, J. Moteff and J. P. Smith, "Neutron Radiation Damage in Tungsten Single Crystals," Phil. Mag. 13, 1079 (1966).

[42] R. P. Tucker and S. M. Ohr, "Direct Observation of Neutron Irradiation Damage in Niobium," Phil. Mag., to be published.

[+] The niobium rods were produced within the Research Materials Program.

Irradiation of these polycrystalline sheet samples was carried out in the Hydraulic Facility (Tube 12) at the Oak Ridge Research Reactor to doses from 2×10^{17} to 5×10^{18} neutrons/cm^2 (E > 1 MeV). During irradiation the samples were in contact with the pool water, and the irradiation temperature is estimated to be less than 50°C. After irradiation, thin foils suitable for electron microscopy were prepared by electropolishing in a solution by volume 85% nitric acid and 15% hydrofluoric acid. The foils were examined in a Hitachi 11A electron microscope operated at 100 kV and equipped with a tilting stage.

Experimental Results and Discussion

Figure 7 shows the irradiation damage in the form of black spots observed under the kinematical diffraction condition in a specimen receiving a dose of 2×10^{18} neutrons/cm^2. For this irradiation dose the size of the black spots ranged from about 50 to 170 Å. The thickness of the foil was estimated as 2500 Å on the basis of the projected width of slip traces which were created in the microscope. With this sample thickness the overall density of the spots is approximately 5×10^{15} cm^{-3}. A preliminary size distribution of spots for doses of 5×10^{17} and 2×10^{18} neutrons/cm^2 is given in a later section of this report.

When the defects are examined under the dynamical diffraction condition ($s \approx 0$), a fraction of the spots exhibit black-white contrast[43,44] as shown in Fig. 8. For each black-white contrast, a symmetry line may be drawn from the black side of the contrast to the white side. It is found that the symmetry lines of the black-white contrasts do not rotate with the diffraction vector as the foil is tilted so as to vary diffraction conditions. This is taken as evidence that the majority of the defects observed are dislocation loops rather than spherically

---

[43] M. F. Ashby and L. M. Brown, "Diffraction Contrast from Spherically Symmetrical Coherency Strains," Phil. Mag. 8, 1083 (1963).

[44] M. Ruhle, M. Wilkens and U. Essmann, "Zur Deutung der elektronenmikroskopischen Kontrasterscheinungen an Fehlstellenagglomeraten in neutron-enbestrahtem Kupfer," Phys. Stat. Sol. 11, 819 (1965).

[redacted]

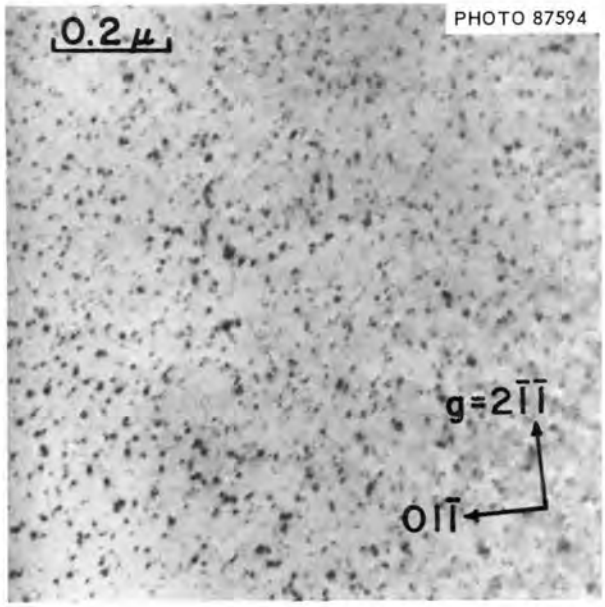

Fig. 7. Defect Images in Neutron-Irradiated Niobium, 2×10^{18} neutrons/cm^2 ($E > 1$ MeV), Revealed Under Kinematical Diffraction Condition ($s > 0$).

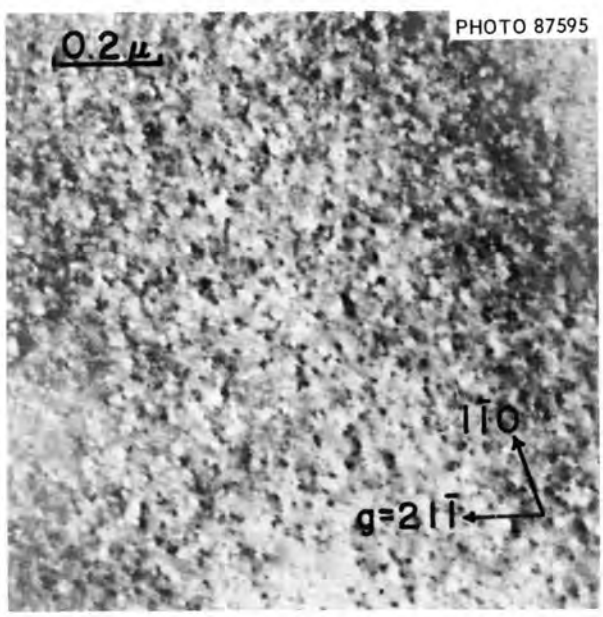

Fig. 8. Black-White Contrast Images of Neutron Irradiation Damage in Niobium Shown Under Bright Field, Dynamical Diffraction Condition ($s \approx 0$).

[redacted]

shaped clusters. From the directions of the symmetry lines, the probable Burgers vectors of the loops are (a/2) ⟨110⟩, a ⟨100⟩, and (a/2) ⟨111⟩.

A comparison of the bright-field and dark-field images reveals that some but not all of the black-white contrasts reverse their directions with respect to the diffraction vector. This observation indicates that the contrasts originate from defects lying close to both top and bottom surfaces of the foil. It has not yet been possible to measure the position of defects accurately to within one-fourth of the extinction distance, which is necessary to determine unambiguously whether the loops are interstitial or vacancy in nature. Preliminary application of the theory of Rühle, Wilkins, and Essmann[44] indicates that the loops are predominately interstitial in nature. However, establishment of the loop nature must await the results of a more detailed study on the depth of the loops in the foil by a stereo technique.

Figure 9 shows a micrograph of a sample which was irradiated and plastically deformed in tension to a strain of approximately 6 percent. Slip traces (or "dislocation channels") can be seen in which the defects are swept out during plastic deformation by moving dislocations.[45-47] The traces are consistent with slip on {110}, {112}, and {123} planes along ⟨111⟩ directions as also is true for the slip lines observed on the surface of irradiated niobium tensile samples.[48]

---

[45] A. H. Cottrell, "Point Defects and the Mechanical Properties of Metals and Alloys at Low Temperatures," in Vacancies and Other Point Defects in Metals and Alloys, The Institute of Metals, London, 1958, p. 1.

[46] B. Mastel, H. F. Kissinger, J. J. Laidler, and T. K. Bierlein, "Dislocation Channeling in Neutron-Irradiated Molybdenum," J. Appl. Phys. 34, 3637 (1963).

[47] A. Seeger, "Work-Hardening of Metal Single Crystals, Slip Lines and Transmission Electron Microscopy," in The Relation Between the Structure and Mechanical Properties of Metals. Vol. I, H.M.S.O., London, 1963.

[48] R. P. Tucker, R. E. Reed and M. S. Wechsler, "Slip Line Observations on Irradiated Niobium Single Crystals," Radiation Metallurgy Section Solid State Division Progress Report for Period Ending February 1966, ORNL-3949, May 1966, p. 63.

[redacted]

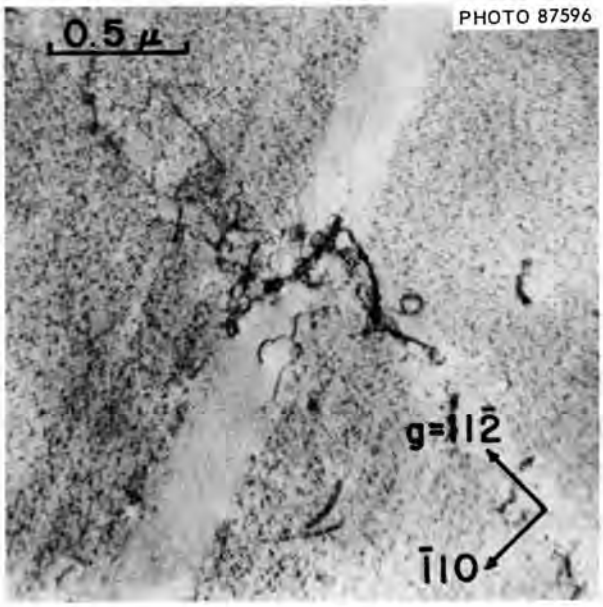

Fig. 9. Slip Traces ("Dislocation Channels") in Neutron Irradiated Niobium Believed to have Been Swept Relatively Free of Defects by Moving Dislocations During Straining in Tension to 6 Percent.

Observations made on unirradiated samples prepared in an identical manner do not show the black spots. Also, only a very few spots were observed in samples irradiated to a dose of 2×10^{17} neutrons/cm^2. Therefore, it is concluded that the spots are indeed defects that are produced as a consequence of fast neutron bombardment and not by electropolishing or in the electron microscope.

The Effect of Oxygen on "Stage III" Annealing in Neutron-Irradiated Niobium

J. T. Stanley, J. M. Williams, W. E. Brundage

I. Introduction

The term "Stage III" annealing in b.c.c. metals refers to a well-defined electrical resistivity decrease which occurs at about 15% of the melting point after either neutron irradiation or deformation in

[redacted]

Nb, Mo, W, and Fe.[49-55] In other reports in this series,[56,57] we have presented evidence that this effect in neutron irradiated niobium is caused by the migration of interstitial oxygen to radiation produced defects. We observed that post-irradiation annealing at 150° reduced the height of the oxygen Snoek peak and that significant resistivity decreases did not appear upon annealing oxygen-free samples up to 200°C. In the present report this evidence is extended to include a kinetics study which shows a clear connection between the oxygen Snoek peak decrease and the resistivity decrease in Stage III. We have also annealed a heavily deformed oxygen-free sample through the Stage III region and the results reveal no significant resistivity decreases in this temperature range.

---

[49] D. E. Peacock and A. A. Johnson, "Stage III Recovery in Neutron Irradiated Molybdenum and Niobium," Phil. Mag. 8, 563 (1963).

[50] L. Stals and J. Nihoul, "Stage III Recovery in Cold-Worked Niobium," Phys. Stat. Sol. 8, 785 (1965).

[51] L. J. Cuddy, "An Electrical Resistivity Study of Deformation and Recovery of Iron at Low Temperature," Phil. Mag. 12, 855 (1965).

[52] G. H. Kinchin and M. W. Thompson, "Irradiation Damage and Recovery in Molybdenum and Tungsten," J. Nuclear Energy 6, 275 (1958).

[53] D. G. Martin, "The Annealing of Point Defects in Cold Worked Molybdenum," Acta Met. 5, 371 (1957).

[54] H. Schultz, "Die Erholung des Elektrischen Widerstandes von Kaltverformtem Wolfram," Acta Met. 12, 649 (1964).

[55] J. Moteff and J. P. Smith, "Recovery of Defects in Neutron-Irradiated Tungsten," Flow and Fracture of Metals and Alloys in Nuclear Environments, ASTM Special Technical Publication No. 380, ASTM, Philadelphia, 1965. p. 171.

[56] J. T. Stanley and W. E. Brundage, "The Interaction of Radiation Produced Defects and Interstitial Impurity Atoms in Niobium," Radiation Metallurgy Section Solid State Division Progress Report for Period Ending July 1966, ORNL-4020, September 1966, p. 49.

[57] J. M. Williams, J. T. Stanley, and W. E. Brundage, "The Interaction of Radiation Produced Defects and Interstitial Impurity Atoms in Niobium," Radiation Metallurgy Section Solid State Division Progress Report for Period Ending January 1967, ORNL-4097, April 1967, p. 30.

II. Experimental Procedures

The material to be irradiated (Sample G) was produced by annealing and outgassing a 0.030" dia. niobium wire by the procedure used for Samples E and F, whose preparation has been described before.[57] The final vacuum achieved was 5×10^{-9} torr at 2200°C. A controlled quantity of oxygen was then added by an anodizing procedure similar to that described by Tedmon, Rose, and Wulff.[58] After outgassing, the wire was removed from the vacuum system and anodized to a depth of about 580 Å. It was then replaced in the vacuum system and homogenized for 2 hrs. at 1000°C. at a vacuum of 1×10^{-8} torr. The amount of niobium pentoxide formed by the anodizing treatment was calculated to give an oxygen concentration of 50 wt. ppm. The wire was then cut into several internal friction and electrical resistivity specimens. The internal friction and resistivity measurements confirmed that the oxygen concentration was about 50 wt. ppm.

The specimens were then irradiated to a fluence of 2×10^{18} neutrons/cm^2 ($E > 1.0$ MeV) in the liquid-nitrogen-cooled cryostat in the Bulk Shielding Reactor. The irradiation temperature was 40-50°C.

Following the irradiation the specimens were isochronally and isothermally annealed. The resistivity specimens were annealed in a silicone oil bath controlled to ± 0.1°C. Annealing of the internal friction specimens was done with the specimens mounted in the torsion pendulum. Resistivity measurements were made at 4.2°K. The methods used in making resistivity and internal friction measurements have been given in previous reports.[56,57]

The deformed sample was made from a 3/16" dia. high-purity zone-refined single crystal whose preparation has been described in detail.[59] The resistance ratio, R(300°K)/R(4.2°K), of the single crystal was 1420.

---

[58] C. S. Tedmon, Jr., R. M. Rose, and J. Wulff, "Controlled Additions of Small Amounts of Oxygen to Niobium (Columbium)," Trans. AIME 230, 1732 (1964).

[59] R. E. Reed, "Niobium: Purification and Perfection," Radiation Metallurgy Section Solid State Division Progress Report for the Period Ending January 1967, ORNL-4097, April 1967, p. 20.

The residual resistivity was approximately 0.01 μΩ-cm, and this sets an upper limit of about 3 wt. ppm on the interstitial impurity level using impurity resistivity contributions cited in the previous report.[57] A portion of the single crystal was rolled and drawn at room temperature to a reduction in area of 95%. Changes in resistivity upon isochronal annealing up to 200°C were made by the same methods used to study Sample G.

III. Results

After irradiation, an internal friction specimen and a resistivity specimen from Sample G were isothermally annealed at 150°C. For the internal friction measurement, the frequency was 0.89Hz, so that the temperature of the oxygen peak was very nearly 150°C. Both the resistivity and internal friction decreased with annealing time at 150°C, and after 8000 minutes they were still decreasing slowly. Nevertheless, to facilitate comparison of the kinetics of the two property changes, the effects in each sample were normalized to the total change observed after 8000 min. The results are shown in Fig. 10. The agreement in kinetics of the internal friction decrease with the resistivity decrease provides convincing evidence that the two property changes are reflecting the same process in the region of Stage III annealing.

A significant feature of the resistivity measurements is the fact that the final resistivity after annealing was well below the pre-irradiation value. Upon irradiation the resistivity increased from 0.185 to 0.233 μΩ-cm, and after 8000 min. at 150°C the resistivity had decreased to 0.148 μΩ-cm. On the assumption that the resistivity contribution of oxygen in solid solution is 0.0039 μΩ-cm/wt. ppm,[58] the decrease in resistivity from 0.233 to 0.148 μΩ-cm corresponds to 22 wt. ppm of oxygen removed from solid solution, which comprises 46 percent of the initial oxygen concentration. On the other hand, the internal friction results indicated removal of 60% of the initial concentration. This difference is accounted for by assuming that the oxygen still contributes somewhat to the resistivity when it is removed from solid solution by being trapped at radiation-produced defects. The necessary resistivity contribution for the trapped oxygen is about 27 percent of the contribution when in solid solution.

[redacted]

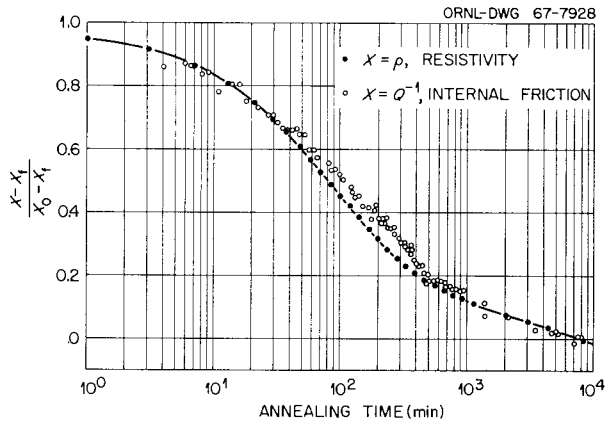

Fig. 10. Normalized Resistivity and Internal Friction Decrease Versus Log Annealing Time at 150°C for Sample G Irradiated to 2 x 10^{18} n/cm^2 (E > 1 MeV) at 40-50°C. X_o and X_f Refer to the Property Immediately After Irradiation and After Annealing for 8000 Min. Respectively.

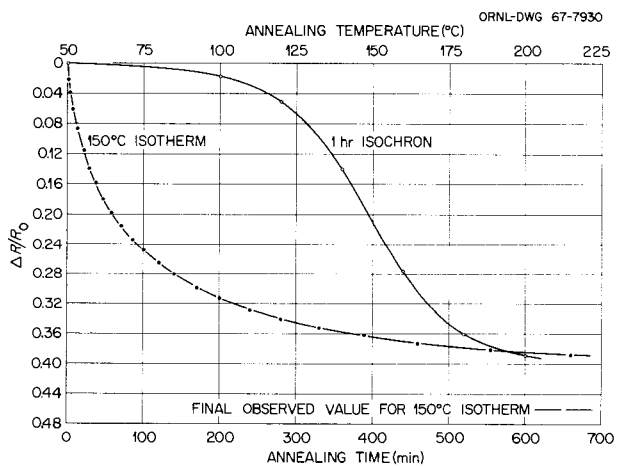

Fig. 11. Fractional Change in Electrical Resistance Upon Isochronal and Isothermal Annealing of Sample G.

[redacted]

Another resistivity specimen from Sample G was isochronally annealed up to 200°C. The results are shown in Fig. 11, together with a replot of the isotherm shown in Fig. 10. In order to plot the two curves in a common unit free of geometrical factors, the quantity $\Delta R/R_o$ has been plotted on the ordinate. R_o is the pre-irradiation resistance and ΔR is the change in the resistance upon annealing.

The two curves in Fig. 11 were combined in a Meechan-Brinkman analysis[60] and the results are shown in Fig. 12. A least squares fit to the first four points yields an activation energy of 1.19 eV. The two points corresponding to the 180°C and 200°C isochronal anneals fall off this line. However, referring again to Fig. 11, we see that the sample is approaching saturation at these temperatures, and thus the analysis becomes inaccurate. The activation energy 1.19 eV agrees with the values 1.19 - 1.25 eV obtained by Peacock and Johnson[49] for neutron-irradiated niobium and 1.20 eV by Stals and Nihoul[50] for cold-worked niobium. This serves to identify the process observed in the present experiment with the "Stage III" annealing observed by the other workers.

Figure 13 shows the isochronal annealing results for the high-purity deformed sample. The magnitude of the resistivity decrease up to 200°C is only 0.002 μΩ-cm. This is less than 10% of the resistivity introduced by deformation and could be accounted for by removal of only about 0.5 wt. ppm of oxygen from solid solution.

IV. Discussion

We believe these results taken in conjunction with the data presented previously[56,57] serve to complete the argument that Stage III in neutron irradiated niobium is caused by the migration of oxygen to radiation produced defects. The evidence favoring this conclusion may now be summarized

---

[60] C. J. Meechan and J. A. Brinkman, "Electrical Resistivity Study of Lattice Defects Introduced in Copper by 1.25-MeV Electron Irradiation at 80°K," Phys. Rev. 103, 1193 (1956).

[redacted]

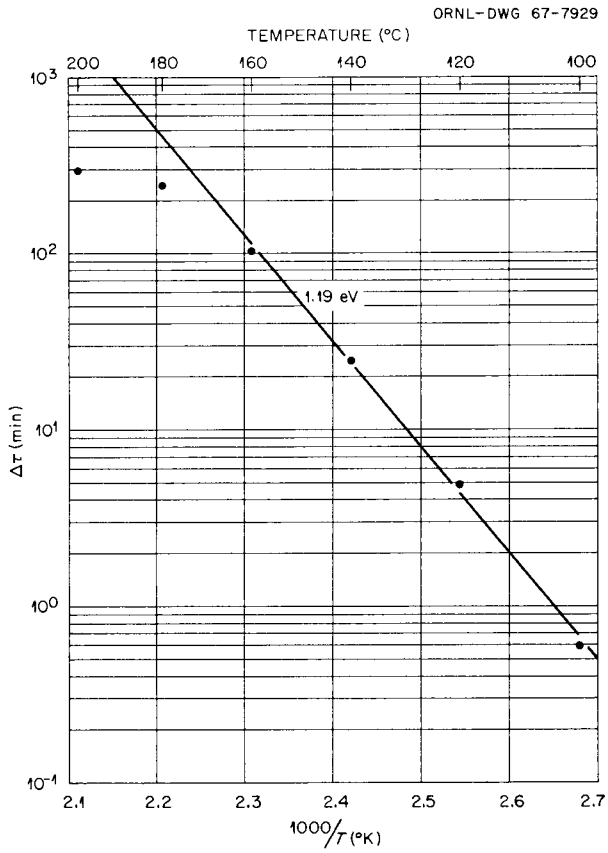

Fig. 12. Meechan - Brinkman Plot for Sample G.

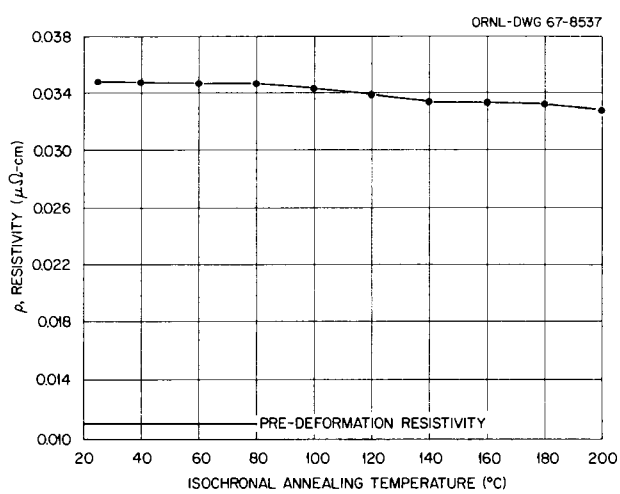

Fig. 13. Resistivity Versus Isochronal Annealing Temperature for Heavily-Deformed High-Purity Niobium.

[redacted]

as follows:

1) A pronounced resistivity annealing stage did not occur between 100°C and 200°C unless oxygen was present in solid solution above about 5 wt. ppm.

2) Post-irradiation annealing between 100°C and 200°C reduced the height of the oxygen Snoek peak. The kinetics of the internal friction decrease and the resistivity decrease were similar.

3) The resistivity went well below the pre-irradiation value during "Stage III" annealing of oxygen-bearing samples. This cannot be understood in terms of simple annealing of defects introduced by irradiation, but would be a natural consequence of removal of oxygen from random solid solution.

4) The activation energy of about 1.2 eV for the stage as determined in this and other experiments[61,62] is near the diffusion activation energy of 1.17 eV for oxygen as determined by Powers and Doyle.[63]

The nature of the defects which act as sinks for the oxygen atoms is suggested by the recent electron microscope observation of Tucker and Ohr,[64,65] which showed small dislocation loops in niobium specimens neutron-irradiated under conditions similar to those used for our experiments. An analysis of the kinetics appropriate for drift of oxygen atoms to the dislocation loops supports the idea that the loops act as sinks for the oxygen atoms.[66]

---

[61] L. Stals and J. Nihoul, "Stage III Recovery in Cold-Worked Niobium," Phys. Stat. Sol. 8, 785 (1965).

[62] L. J. Cuddy, "An Electrical Resistivity Study of Deformation and Recovery of Iron at Low Temperature," Phil. Mag. 12, 855 (1965).

[63] R. W. Powers and M. V. Doyle, "Diffusion of Interstitial Solutes in the Group V Transition Metals," J. Appl. Phys. 30, 514 (1959).

[64] R. P. Tucker and S. M. Ohr, "Direct Observation of Neutron Irradiation Damage in Niobium," Phil. Mag., to be published.

[65] R. P. Tucker and S. M. Ohr, this report.

[66] R. Bullough, J. T. Stanley, and J. M. Williams, "The Kinetics of Migration of Impurities to Small Dislocation Loops," submitted for publication.

The absence of annealing in the deformed sample indicates that Stage III observed after cold work[61] in niobium is also due to oxygen. Since this experiment was undertaken, other annealing studies on high-purity deformed niobium have been published.[67,68] These authors conclude that the recovery stages in the 25 to 200°C range after deformation are due to impurities, and our results support this conclusion.

As concerns mechanical properties, the present results lend strong support to the idea that the thermal hardening observed by Makin and Minter[69] in neutron irradiated niobium is caused by the migration of oxygen to dislocation loops. The activation energy for thermal hardening is 1.3 ± 0.1 eV, which is equal within experimental error of the activation energy determined in the present study. We have started measurements to determine the temperature at which oxygen returns to solution after being trapped at the dislocation loops. The measurements made thus far show that oxygen dissociates from the loops in the temperature range where the recovery of the radiation induced hardness occurs.

Radiation Hardening in B.C.C. Metals Niobium and Iron

S. M. Ohr, R. P. Tucker* and M. S. Wechsler

I. Introduction

Although the effect of neutron irradiation on plastic deformation of b.c.c. metals has been the subject of a number of investigations, the mechanism of radiation hardening has not been well established. In the past, most of the work in this field has dealt with polycrystalline materials, and more specifically, in fitting the data to the Petch relationship.

---

[67] A. Köthe and F. Schlät, "Recovery of Deformed Niobium and Tantalum Degassed in Ultra-High Vacuum," Phys. Stat. Sol. 21, K73 (1967).

[68] R.-J. Dinter, "High Vacuum Purification of Niobium and Tantalum and its Influence on the Electrical Resistivity," Z. Metallkunde 58, 70 (1967).

[69] M. J. Makin and F. J. Minter, "The Mechanical Properties of Irradiated Molybdenum," Acta Met. 7, 361 (1959).

*Oak Ridge Graduate Fellow from the University of Tennessee under appointment from Oak Ridge Associated Universities.

Cottrell[70] proposed that at the yield stress an avalanche of dislocations pile up against grain boundaries and build up stress concentrations which then activate dislocation sources in adjacent grains. In this scheme, the Petch parameter τ_i is a measure of the lattice friction stress, while k_y is directly proportional to the unpinning stress. Thus, an analysis of radiation hardening in terms of the Petch equation should provide in polycrystalline materials a means of distinguishing between the friction and source types of hardening. The Petch analysis has proved satisfactory in certain studies[71-74] on neutron irradiated b.c.c. metals, but the work by Johnson et al.[75,76] on neutron irradiated molybdenum has case serious doubt as to the usefulness of this type of approach for establishing the underlying mechanism of hardening.

In an attempt to clarify certain aspects of the problem, the present work has sought to determine the magnitude and the temperature dependance of the yield stress in neutron irradiated single crystal niobium and polycrystalline iron. These measurements are further supplemented by the strain rate dependency of radiation hardening, in an effort to establish the nature of the interaction between radiation induced defects

---

[70] A. H. Cottrell, "Theory of Brittle Fracture in Steel and Similar Metals," Trans. Met. Soc. A.I.M.E. 212, 192 (1958).

[71] D. Hull and I. L. Mogford, "Precipitation and Irradiation Hardening in Iron," Phil. Mag. 6, 535 (1961).

[72] I. L. Mogford and D. Hull, "Effect of Temperature and Neutron Irradiation on Yield and Work Hardening in Iron," J. Iron and Steel Inst. 201, 55 (1963).

[73] P. R. V. Evans, A. F. Weinberg and R. J. Van Thyne, "Irradiation Hardening in Niobium (Columbium)," Acta Met. 11, 143 (1963).

[74] J. D. Campbell and J. Harding, "The Effect of Grain Size, Rate of Strain, and Neutron Irradiation on the Tensile Strength of α-Iron," in Response of Metals to High Velocity Deformation, edited by P. G. Shewmon and V. F. Zakay, Interscience Publishers, New York, 1961. p. 51.

[75] A. A. Johnson, N. Milasin and F. N. Zein, "The Embrittlement of Body-Centered Cubic Transition Metals by Neutron Irradiation," in Radiation Damage in Solids, Vol. 1, I.A.E.A., Vienna, 1962. p. 259.

[76] A. S. Wronski, G. A. Sargent and A. A. Johnson, "Irradiation Hardening and Embrittlement in Body-Centered Cubic Transition Metals," in Flow and Fracture of Metals and Alloys in Nuclear Environments, STP 380, A.S.T.M., Philadelphia, 1965. p. 69.

and mobile dislocations. In order to seek direct evidence of such interaction, observations have been made of the microstructure of neutron irradiated and plastically deformed samples by transmission electron microscopy. On the basis of these preliminary experimental studies, the nature of the interaction between the defects and the moving dislocations is discussed and a mechanism of radiation hardening in b.c.c. metals has been formulated.*

II. Experimental Procedure

Single crystals of niobium were grown in the form of 3/16-inch diameter rods in a Material Research Corporation electron-beam floating zone refiner. These rods were seeded so as to give the orientation for maximum resolved shear stress on the {110} ⟨111⟩ slip system. The Schmid Factor was always greater than 0.496 on the indicated system. Round tensile samples were prepared from 1.5-inch long segments of the zoned rod by centerless grinding a 0.75-inch gage length and an average gage diameter of 0.085 inch. Twenty mils were chemically polished from the gage diameter in a solution of nitric and hydrofluoric acids mixed in proportions of 3 to 2 to remove the damage introduced by the grinding. Tensile samples of polycrystalline Ferrovac E iron were prepared from cold rolled sheets of 0.01-inch thickness with gage lengths of 0.50 inch. These sheet samples were annealed *in vacuo* to achieve a uniform average grain diameter of approximately 30μ.

Sample irradiations were carried out in facilities located in the Oak Ridge Research Reactor and the Bulk Shielding Reactor at temperatures below 110°C to doses between 1.2×10^{16} and 2×10^{18} neutrons/cm^2 ($E > 1$ MeV). Tensile deformation was carried out in an Instron testing machine. The test temperature was varied between 77°K and 298°K by immersing the samples in constant temperature baths.

---

*The authors wish to thank Dr. R. Bullough, on assignment from AERE, Harwell, for invaluable discussions and comments.

III. Experimental Results

Yield Stress Measurements

The increase in the upper yield stress as a function of neutron dose for the niobium single crystals has already been presented in this series of reports.[77] The temperature dependence of yield stresses* for unirradiated and irradiated niobium single crystals is shown in Fig. 14. The overall effect of neutron irradiation is an upward shift of the yield stress curves over that of the unirradiated samples without an appreciable change in its shape. This is in marked contrast with the hardening observed in neutron irradiated f.c.c. metals in which the major part of the strengthening is in the temperature dependent portion of the yield stress. A similar plot obtained from polycrystalline iron samples appeared in a previous report.[78] It is again noted that the temperature dependence of the yield stress is not appreciably affected by neutron irradiation.

The strain-rate and temperature dependencies of irradiation hardening were evaluated in terms of the thermal activation parameters.[79] One of the parameters of interest is the activation volume, v, which represents the strain rate sensitivity of the yield stress. It can be determined experimentally through the expression

$$v = kT \left(\frac{\partial \ln \dot{\varepsilon}}{\partial \tau^*}\right)_T , \qquad (1)$$

---

[77] R. P. Tucker, M. S. Wechsler and N. E. Hinkle, "Dependence of Yield Stress on Neutron Dose in Niobium Single Crystals," Radiation Metallurgy Section Solid State Division Progress Report for Period Ending July 1966, ORNL-4020, September 1966, p. 29.

*The tensile tests were carried out by one of us (MSW) while on assignment with the Metal Physics Group, Battelle Institute, Geneva, Switzerland. The assistance of Miss R. Bode is greatfully acknowledged.

[78] S. M. Ohr and E. D. Bolling, "On the Temperature and Strain Rate Dependence of Radiation Hardening in Iron," Radiation Metallurgy Section Solid State Division Progress Report for Period Ending January 1967, ORNL-4097, April 1967, p. 13.

[79] H. Conrad, "On the Mechanism of Yielding and Flow in Iron," J. Iron and Steel Inst. 198, 364 (1961).

[redacted]

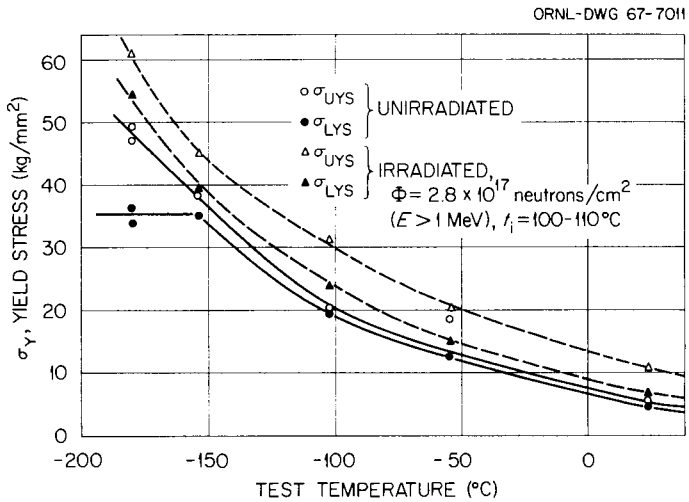

Fig. 14. Temperature Dependence of Yield Stress in Unirradiated and Neutron Irradiated Niobium Single Crystals.

where $\dot{\epsilon}$ is the strain rate, τ^* is the effective shear stress, k is Boltzmann's constant, and T is the test temperature. The activation volume is related to the following microscopic quantities

$$v = b\ d\ \ell \quad , \tag{2}$$

where b is the Burgers vector, d and ℓ are the size and the average spacing, respectively, of the barriers that give rise to the short range resistance to dislocation motion. In determining the activation volume, both the rate change test and the stress relaxation method were employed. A plot of the activation volume as a function of the effective stress for both unirradiated and irradiated iron was given in a preceding report.[78] The effective stress was obtained from the applied stress by subtracting the athermal stress, which was determined from the stress relaxation technique suggested by Li.[80] It can be seen from that plot that data from both unirradiated and irradiated samples fall along a single smooth curve. This is in contrast to some observations reported on neutron

[80] J. C. M. Li, "Dislocation Dynamics in Deformation and Recovery," in Proc. Int. Conf. Deformation of Crystalline Solids, Ottawa, 1966 Canadian J. Phys. 45, No. 2, Part 2, 493 (1967).

[redacted]

irradiated iron[81] and molybdenum.[76] It may be stated that the effect of neutron irradiation is to raise the effective stress for deformation, but when the activation volume is compared at the same level of effective stress there is no change due to irradiation.

Another parameter of interest is the activation energy, H, associated with the thermal activation of dislocation motion. The activation energy is defined as

$$H = H_o - v\,\tau^* \quad , \tag{3}$$

where H_o is the maximum interaction energy between the barriers and the moving dislocations. The second term on the right hand side corresponds to the work done by the applied stress during the thermal activation. The activation energy is determined experimentally through the expression

$$H = -vT\left(\frac{\partial \tau^*}{\partial T}\right)_{\dot{\epsilon}} \quad . \tag{4}$$

A past report[78] also shows a plot of the activation energy as a function of the effective stress for iron. It shows that the activation energy has increased slightly after neutron irradiation. The estimated values of H_o are approximately 0.87 eV and 0.97 eV for unirradiated and irradiated samples, respectively. This difference is indeed not greater than the accuracy of the present experimental technique. Even if the difference is real the magnitude is too small to indicate any change in the rate controlling mechanism of plastic deformation after neutron irradiation.

Electron Microscope Observations

Neutron irradiation damage was observed directly in niobium by transmission electron microscopy in samples irradiated to doses greater than 2×10^{17} neutrons/cm^2. Figure 15 shows the damage appearing as black spots under the kinematical electron diffraction condition. As the neutron dose is raised, both the density and size of the spots increase. Figure 15 (C) shows the damage structure in a sample irradiated to 2×10^{18} neutrons/cm^2 and subsequently annealed at 300°C for 1 hr. According to

[81] F. A. Smidt, Jr., "Effects of Irradiation on Thermally Activated Flow in Iron," J. Appl. Phys. 36, 2317 (1965).

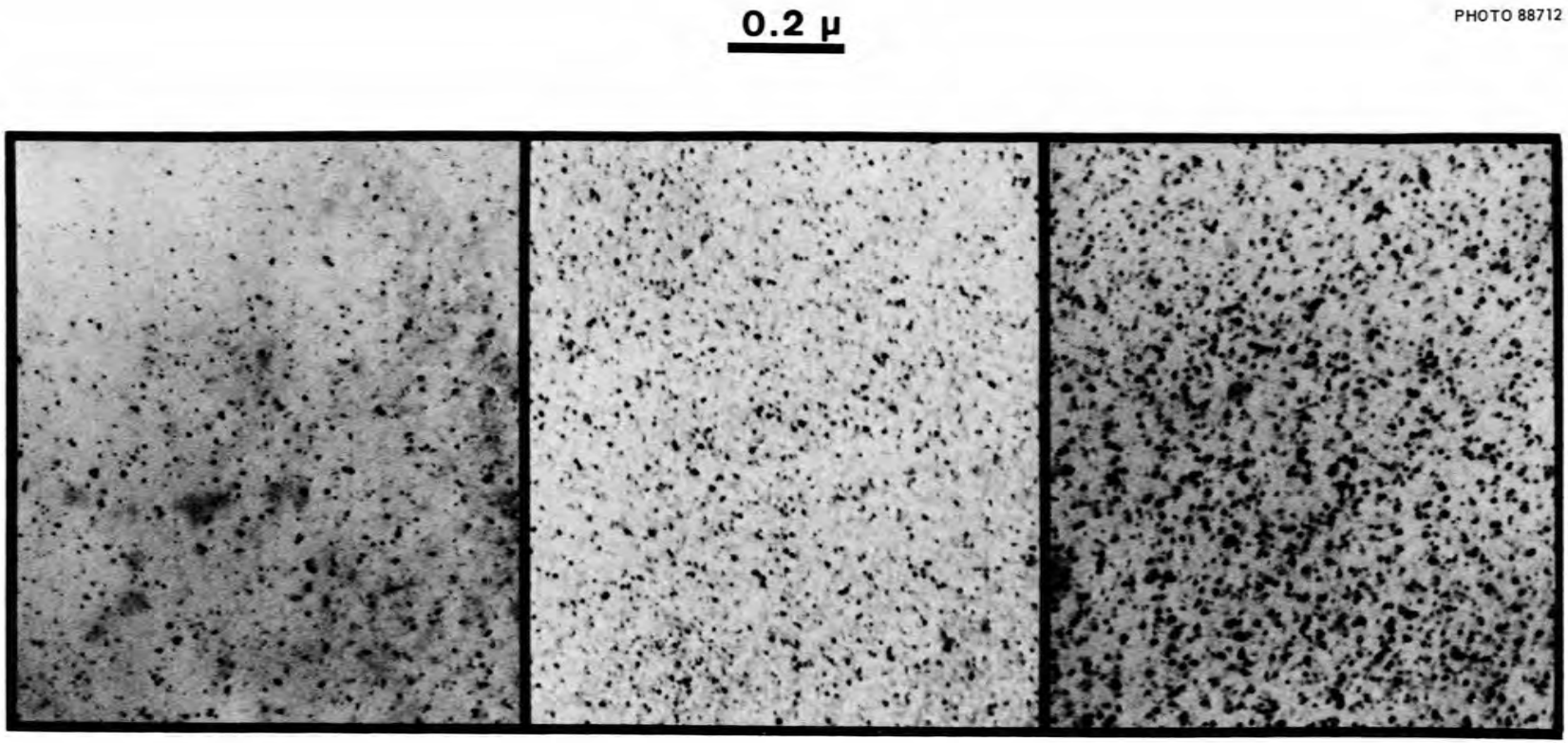

(A) 5×10^{17} neutrons/cm^2

(B) 2×10^{18} neutrons/cm^2

(C) 2×10^{18} neutrons/cm^2 + 300°C Anneal for 1 hour

Fig. 15. Comparison of Defect Images in Niobium Irradiated with Neutrons ($E > 1$ MeV) to the Indicated Doses.

the work in copper by Makin et al.,[82] one expects a mild anneal to reveal defects which initially are submicroscopic in size. In niobium, it is found that the anneal at 300°C for 1 hr. increased the total density of spots by approximately 16%. It is likely that in niobium the 300°C annealing temperature is not sufficiently high to reveal all of the submicroscopic defects.

From these kinematical electron micrographs, counts have been made of the spots as a function of the spot size on a Zeiss particle size analyzer. The results are shown in Fig. 16. As the neutron dose is raised from 5×10^{17} to 2×10^{18} neutrons/cm^2, there is a slight increase in the peak spot size. A more prominent change is in the increase in the densities of large spots. Upon post-irradiation annealing for 1 hr. at 300°C, there is a trend toward a further increase in the density of large spots. A major feature of all three curves is the sharp decrease in spot density below a spot size of about 70 Å; the reason for this is not clear at present. This drop in spot density is more likely due to insufficient contrast than limitations in the resolution of the electron microscope, which is expected to be better than 30 Å.

IV. Discussion

In contrast to radiation hardening in f.c.c. metals, the characteristic feature of the increase in hardening in b.c.c. metals by neutron irradiation is its relative insensitiveness to test temperature. As was pointed out by Friedel,[83] this implies that the interaction energy between the mobile dislocations and the barriers introduced by irradiation is quite large, i. e. the process of overcoming the barriers is not thermally activated. A type of interaction that would agree with this experimental observation is the elastic interaction between dislocations and large dislocation loops. The choice of such a model also draws

---

[82] M. J. Makin, F. J. Minter and S. A. Manthorpe, "The Correlation between the Critical Shear Stress of Neutron Irradiated Copper Single Crystals and the Density of Defect Clusters," Phil. Mag. 13, 729 (1966).

[83] J. Friedel, "On the Elastic Limit of Crystals," in Electron Microscopy and Strength of Crystals edited by G. Thomas and J. Washburn, Interscience Publishers, New York, 1963. p. 605.

[redacted]

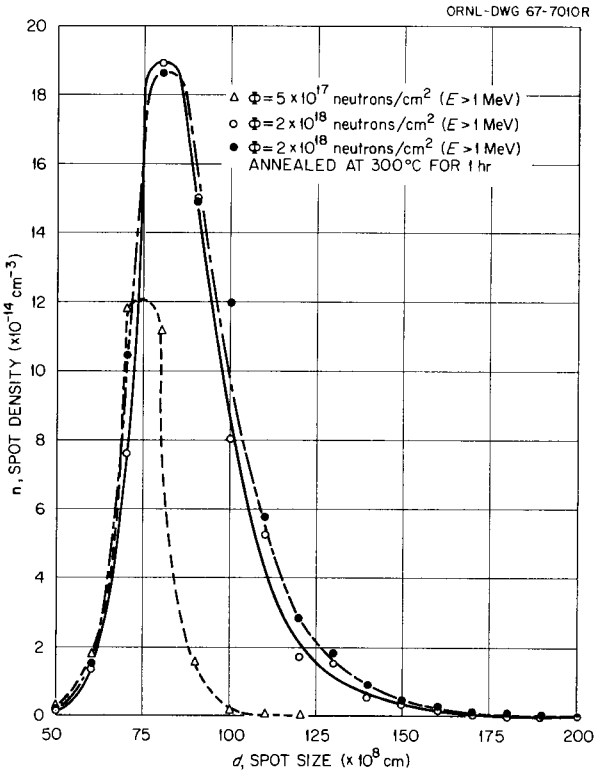

Fig. 16. Density of Defects as a Function of Diameter in Neutron Irradiated Niobium.

impetus from the observations in the electron microscope of the presence of irradiation induced dislocation loops and of slip traces free of these loops subsequent to plastic deformation.

In formulating the mechanism of radiation hardening, one must examine the possible role of small loops that are invisible in the electron microscope. According to Kroupa,[84] the elastic interaction energy between a dislocation loop and straight dislocation is directly proportional to the size of the loop. Thus the large loops, visible in the electron microscope, will be predominant in the elastic interaction. The small loops, however, could be quite effective in impeding dislocation motion

[84] F. Kroupa, "The Interaction between Prismatic Dislocation Loops and Straight Dislocations. Part I," Phil. Mag. 7, 783 (1962).

[redacted]

and hence could contribute substantially to hardening that is sensitive to test temperature. This is believed to be the mechanism of radiation hardening operative in f.c.c. metals.[82,85] In b.c.c. metals, the present work has shown that the hardening introduced is relatively insensitive to test temperature and furthermore there is essentially no change in the parameters of thermally activated dislocation motion following irradiation. A possible explanation may be found in the strong temperature dependence of the yield stress already present in b.c.c. metals prior to neutron irradiation. This type of behavior suggests that in b.c.c. metals there are numerous small obstacles that can interact strongly with dislocations in the absence of neutron irradiation damage. It appears that the small loops introduced by irradiation are either not sufficient in number or less effective relative to the barriers already present prior to irradiation. In the following, therefore, estimates have been made of hardening due to irradiation solely on the basis of elastic interaction between moving dislocations and large dislocation loops that are visible in the electron microscope.

According to Saada and Washburn,[86] the long range interaction between a straight dislocation and a dislocation loop is weak due to the rapid fall off in the stress field around the loop. It is also shown that the critical stage in the interaction occurs when the dislocation comes in contact with the loop. The contact interaction then depends on the type and orientation of the loop relative to the slip plane and burgers vector of the slip dislocation. In the case of b.c.c. metals, between pure edge prismatic loops on {111} planes and slip dislocations on {110} planes with Burgers vector (a/2) ⟨111⟩, there are five essentially different orientations. Since the dislocations are always attracted to a certain portion of a loop, only the attractive interaction is considered.

---

[85] T. J. Koppenaal and R. J. Arsenault, "A Rate Controlling Mechanism for Slip in Neutron Irradiated Copper Single Crystals," Phil. Mag. 12, 951 (1965).

[86] G. Saada and J. Washburn, "Interaction Between Prismatic and Glissile Dislocations," in Int. Conf. Crystal Lattice Defects, Kyoto, 1962, J. Physic. Soc. Japan 18, suppl. I, 43 (1963).

[redacted]

By applying the method of Kroupa and Hirsch[87] to b.c.c. metals and by considering the contact interaction within a plate of thickness twice the radius of the loop, R, the maximum interaction energy for a screw dislocation is found to be

$$E_{max} = \frac{1}{4} \mu b^2 R \quad , \tag{5}$$

where μ is the shear modulus and b is the Burgers vector. The maximum force on the dislocation is

$$F_{max} = \frac{1}{4} \mu b^2 \quad , \tag{6}$$

and hence the increase in the yield stress is

$$\Delta \tau = \frac{\mu b}{4\ell} \quad , \tag{7}$$

where ℓ is the average spacing of the loops along the dislocation.

The average spacing, ℓ, depends on the strength of the barriers,[88] which determines the extent of "bow-out" to cause the slip dislocation to break away from the barrier. The strength of the barrier is directly related to the maximum force, F_{max}, i. e. the maximum slope of the interaction energy versus distance curve and thus is independent of the magnitude of the interaction energy *per se*. In the case of strong barriers the breakaway angle is large, while it is quite small for weak barriers. The breakaway angle corresponding to the maximum force given by (6) is rather small, but it is not small enough to rule out the strong barrier model. For the strong barriers the average spacing, ℓ, may be taken to be equal to the actual average spacing of barriers in the slip plane of thickness 2R, and when there is a spectrum of loop size it is given by

---

[87] F. Kroupa and P. B. Hirsch, Elastic Interaction Between Prismatic Dislocation Loops and Straight Dislocations," in *Dislocations in Solids*, Discussions No. 38, The Faraday Society, London, 1964. p. 49.

[88] A. J. E. Foreman and M. J. Makin, "Dislocation Movement Through Random Arrays of Obstacles," Phil. Mag. 14, 911 (1966).

[redacted]

$$\ell = (\Sigma\, n_i d_i)^{-1/2} \quad , \tag{8}$$

where n_i is the density of loops of diameter d_i. It then follows from equation (7) that the increase in the yield stress due to strong barriers is

$$\Delta\, \tau = \frac{1}{4}\, \mu b\, (\Sigma\, n_i d_i)^{1/2} \quad . \tag{9}$$

This expression is almost identical to the one obtained by Fleischer[89] for f.c.c. metals on the basis of the interaction between dislocations and tetragonal distortions around dislocation loops.

In the case of weak barriers, Friedel[83] suggested that the dislocations will tend to move in a zig-zag fashion so that the effective barrier spacing along the dislocation is greater than the average barrier spacing, ℓ. The effective barrier spacing, ℓ', is given by Friedel as

$$\ell' = \left(\frac{2\, T\, \ell^4}{E_{max}}\right)^{1/3} \quad , \tag{10}$$

where $T = \mu\, b^2/2$ is the line tension. From equations (5), (7), (8), and (10) it follows that the increase in the yield stress for weak barriers is

$$\Delta\, \tau = \frac{1}{8}\, \mu b^2\, \langle d \rangle^{1/3}\, (\Sigma\, n_i d_i)^{2/3} \quad , \tag{11}$$

where $\langle d \rangle$ is the average diameter of the loops.

In estimating the magnitudes of hardening for niobium, the electron microscope measurements of the density-size distribution of loops shown in Fig. 16 have been used. In Table 3, the estimated values of hardening are compared with the increases in yield stresses in single crystals of niobium neutron irradiated to doses of 5×10^{17} and 2×10^{18} neutrons/cm^2.

---

[89] R. L. Fleischer, "Solution Hardening by Tetragonal Distortions: Application to Irradiation Hardening in F.C.C. Crystals," Acta Met. 10, 835 (1962).

The agreement is quite reasonable for the case of strong barriers. Although this agreement may be fortuitous in view of simplifying assumptions inherent in the theoretical model and the preliminary nature of the data, it seems clear that in b.c.c. metals the major factor contributing to radiation hardening is the contact interaction between the radiation induced large dislocation loops and dislocations set in motion during deformation.

Table 3

Radiation Hardening by Contact Interaction in Niobium

		THEORY		EXPERIMENT	
Dose (neutrons/cm^2)	$E\ n_i d_i$ (cm^{-2})	Strong Barrier (Kg/mm^2)	Weak Barrier (Kg/mm^2	$\Delta\ \sigma_{LY}$ (Kg/mm^2)	$\Delta\ \sigma_{UY}$ (Kg/mm^2)
5×10^{17}	2.0×10^{9}	1.24	0.20	1.05	1.38
2×10^{18}	5.7×10^{9}	2.07	0.43	1.88	2.11

Dislocation Mobility in Single Crystal Niobium

H. D. Guberman

The etching technique involving the decoration of dislocations in niobium with carbon[90] permitted measurements of the stress dependence of the dislocation velocity to be made with greater certainty. The results of additional measurements with temperature and purity as variables will be discussed below. Certain indirect techniques for the determination of the mobility parameters were examined and will also be reported on.

The etching and velocity measurements were performed as before. With respect to the carbon decoration of the dislocations, it was found that aging at 900°C for 30 minutes sufficed to produce the desired results. Measurements made in this manner were compared to earlier undecorated results at room temperature and found to agree quite well. The maximum difference between the two methods was found to be no greater than 8%, quite reasonable for this sort of measurement. Agreement is in keeping with the fact that recovery or recrystallization is immeasurable for this combination of time, temperature, and degree of deformation.[91] In addition, computation indicates that the mean self-diffusion distance in niobium for 30 min. at 900°C is less than 30 Å, so that any dislocation rearrangement due to climb, etc., will very likely be too small to be observed.

---

[90] H. D. Guberman, "Concerning the Etching of Dislocations in Niobium," Radiation Metallurgy Section Solid State Division Progress Report for Period Ending January 1967, ORNL-4097, April 1967, p. 26.

---

[91] Ingard Kvernes, "Über das Rekristallisationsverhalten von elektronenstrahlgeschmolzenem Niob," Z. Metallk. 54, 449 (1963). E. M. Savitskii, V. V. Baron and K. N. Ivanova, "Diagramma Rekristallizatsii Niobiya," Doklady Akad. Nauk., S.S.S.R. 126, 771 (1959). E. Erben and F. Sperner, "Untersuchungen über die Rekristallisation von electronenstrahlgeschmolzenem Niob, Metall. 17, 1019 (1963).

The surface sources were introduced both by scratching as before with a 0.5-mil-radius diamond stylus under a light load, and also by forming a rosette when the stylus was dropped from a known height under varying loads. Both methods gave the same velocity results but the measurements from the rosettes had to be corrected for the distance dislocations had been induced to move out from the source by the stresses involved in producing the source. This factor was no greater than 0.09 mm. Examples of patterns of dislocations which have moved under stress are shown in Figures 17 and 18 for the two types of sources.

The earlier velocity measurements were repeated at 77°K and performed also at 194°K (Fig. 19). In addition, measurements were made in purer samples of Wah Chang niobium grown with two passes of the floating zone. The resistance ratio of this material (R 300°K/R 4.2°K) is about 220 compared to a ratio of about 125 for the single pass material. The mobility is strongly dependent upon the purity level (Fig. 20), in this case related apparently to the difference in interstitial content. In all cases the expression

$$\bar{v} = (\tau/\tau_o)^{m^*} \qquad (1)$$

fits the data quite well, where τ is the applied stress, m^* and τ_o are constants, and $\bar{v}$ is the average velocity.

The results shown in Fig. 19 indicate no change in slope (m^*) upon decreasing the temperature from 300°K to 194°K, but upon further decrease in temperature to 77°K a slightly increased slope is apparent. This latter observation differs with the one given earlier[92] where a decreased slope at 77°K was claimed. Also the displacement toward higher stresses at 77°K is greater than previously thought. An increasing slope with decreasing temperature is consistent with similar measurements for iron-silicon.[93] All the mobility data for niobium are summarized in Table 4.

---

[92] H. D. Guberman, "Stress Dependence of Dislocation Velocity in Irradiated and Unirradiated Niobium," Radiation Metallurgy Section Solid State Division Progress Report for Period Ending July 1966, ORNL-4020, September 1966, p. 41.

[redacted]

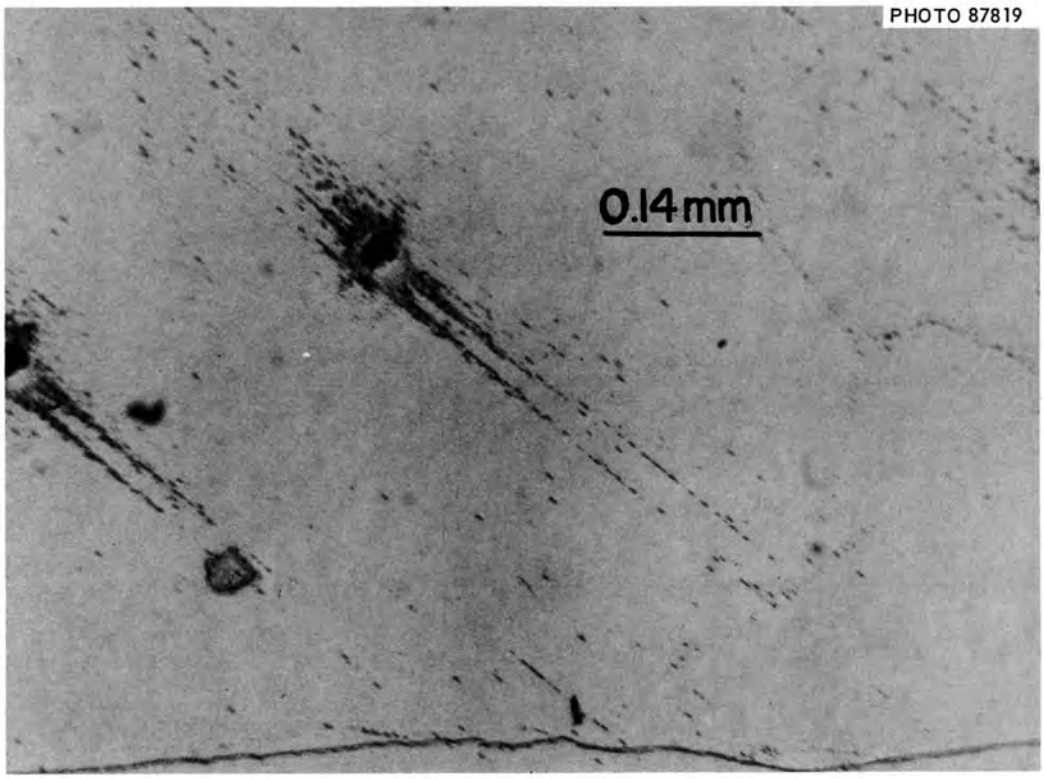

Fig. 17. Etch Figures Surrounding a Rosette After Stressing Revealed by the Carbon Decoration Technique.

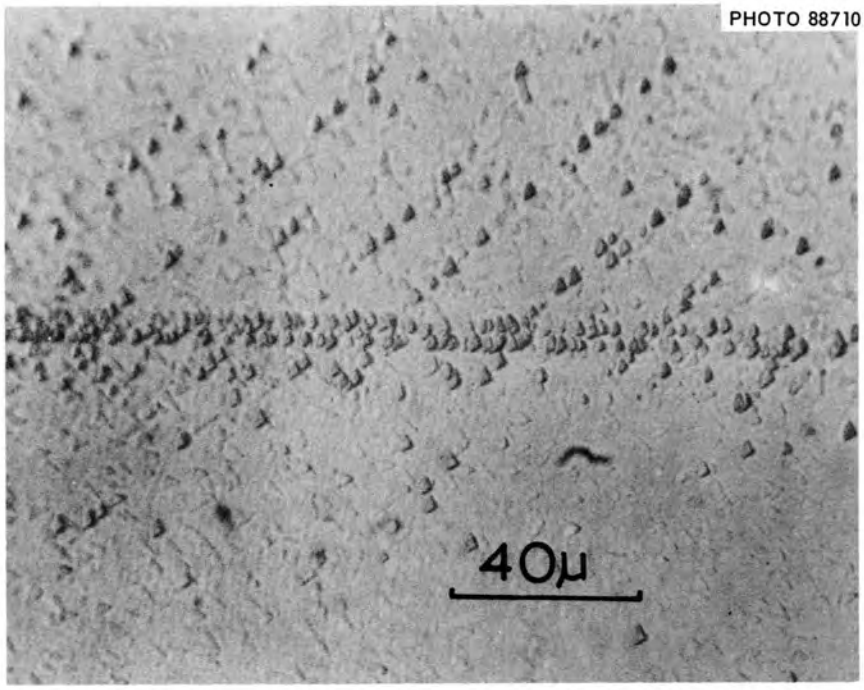

Fig. 18. Etch Figures Surrounding a Scratch After Stressing Revealed by the Carbon Decoration Technique.

[redacted]

[redacted]

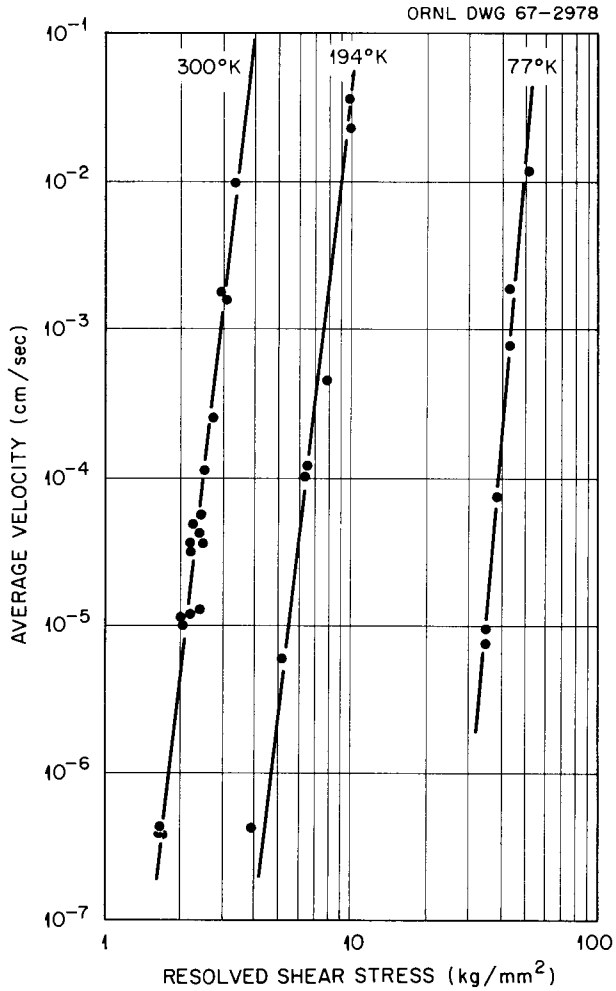

Fig. 19. Dislocation Velocity vs. Stress as a Function of Temperature in Single-Pass Single Crystal Niobium.

[redacted]

[redacted]

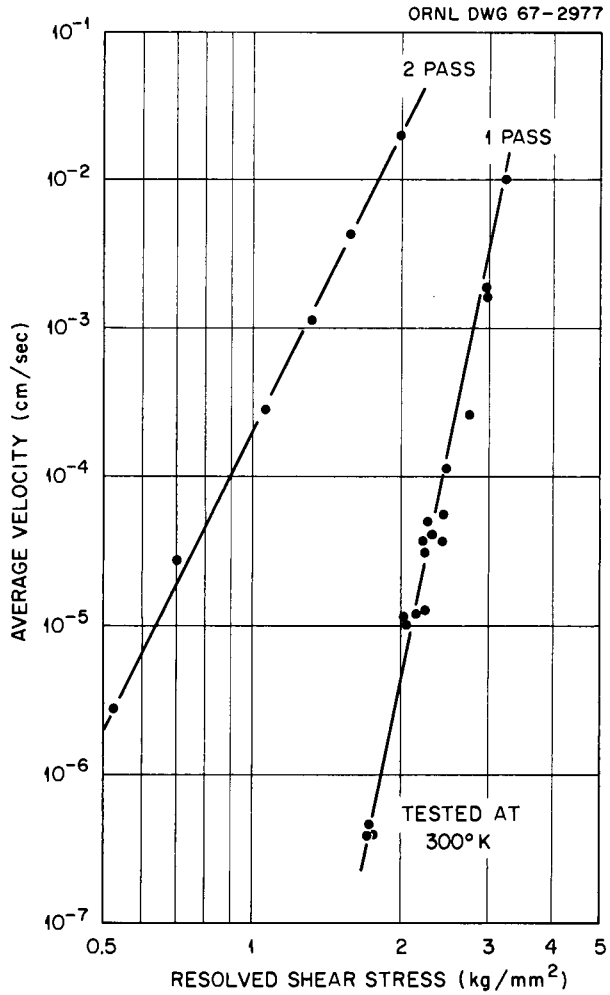

Fig. 20. Dislocation Velocity vs. Stress as a Function of Purity in Single-Crystal Niobium.

[redacted]

[redacted]

Table 4

Summary of Dislocation Mobility Parameters
For Niobium by the Etch-Pit Method

Sample[(a)]	Test Temp. (°K)	m^*	τ_o
Non-irradiated	300	15	4.4
Non-irradiated	194	15	12
Non-irradiated	77	18	63
Non-irradiated, 2 Zone Pass	300	6.7	3.5
1.6×10^{17} n/cm^2 (E > 1 MeV)	300	10	7.7
8.3×10^{17} n/cm^2 (E > 1 MeV)	300	7	24

(a) All samples are one-zone-pass material except as noted.

Work is in progress to measure the neutron dose dependence of the dislocation mobility in niobium with substantially lower tantalum content than before.[92] The lower residual activity after irradiation will permit the samples to be handled much more easily and hence it should be possible to derive more reliable data. As shown in Table 4 the present results indicate a decreasing slope with increasing dose. However, other factors which tend to decrease mobility, such as decreasing temperature and increasing interstitial content, tend at the same time to increase the slope of the velocity-stress curve. On this basis the present results would appear to be anomalous.

---

[93] D. F. Stein and J. R. Low, "Mobility of Edge Dislocations in Silicon-Iron Crystals," J. Appl. Phys. 31, 362, (1960); D. D. Stein and R. P. Laforce, "Mobility of Edge Dislocations in Silicon-Iron Crystals at 20°K," J. Appl. Phys. 36, 661 (1965).

[redacted]

[redacted]

In order to extend the investigation of dislocation mobility, two indirect methods of measurement were investigated. In one, the exponent of the stress dependence of dislocation velocity $(d \ln \bar{v})/(d \ln \sigma)$ is assumed to be related to the strain-rate sensitivity coefficient, $m' = (d \ln \sigma)/(d \ln \dot{\epsilon})$ through the following:[94]

$$\frac{d \ln \bar{v}}{d \ln \sigma} + \frac{d \ln \rho}{d \ln \sigma} = \frac{d \ln \dot{\epsilon}}{d \ln \sigma} \qquad (2)$$

where $\bar{v}$ is the dislocation velocity, ρ is the mobile dislocation density, $\dot{\epsilon}$ is the strain rate and σ is the applied stress. If the second term in Eq. 2 may be neglected, then the exponent of the stress dependence, m^*, equals the reciprocal of the strain-rate sensitivity coefficient, $1/m'$. This was demonstrated in the case of LiF and 3.25% silicon-iron,[95] and in a modified way, in tungsten.[96]

The second indirect method by which the exponent of the stress dependence may be determined is based upon the stress-relaxation technique suggested by Noble and Hull.[97] The analysis for this technique has been refined by Ohr[98] and Li.[99] Li's analysis was applied to the data in this investigation.

---

[94] R. W. Guard, "Rate Sensitivity and Dislocation Velocity in Silicon Iron," Acta Met. 9, 163 (1965).

[95] W. G. Johnston and F. F. Stein, "Stress Dependence of Dislocation Velocity Inferred from Strain Rate Sensitivity," Acta Met. 11, 317 (1963).

[96] H. W. Schadler, "Mobility of Edge Dislocations on {110} Planes in Tungsten Single Crystals," Acta Met. 12, 861 (1964).

[97] F. W. Noble and D. Hull, "Stress Dependence of Dislocation Velocity From Stress Relaxation Experiments," Acta Met. 12, 1089 (1964).

[98] S. M. Ohr, "A Study of Radiation Hardening in Iron by Stress Relaxation Techniques," Radiation Metallurgy Section Solid State Division Progress Report for Period Ending August 1965, ORNL-3878, January 1966, p. 16.

[99] J. C. M. Li, "Dislocation Dynamics in Deformation and Recovery," in Proc. Int. Conf. Deformation of Crystalline Solids, Ottawa, 1966 Canadian J. Phys. 45, No. 2, Part 2, 493 (1967).

[redacted]

Under the assumption that the mobile dislocation density, the internal stress and the combined modulus for sample and testing machine are constant, the stress relaxation curve should be described by

$$\sigma - \sigma_i = K(t + a)^{-n} \tag{3}$$

where K and a are constants, $n = 1/(m^* - 1)$, t is time, σ is the applied stress, and σ_i the long-range internal stress. This relation predicts that a plot of log $(-d\sigma/dt)$ vs. log t should approach a straight line with a slope of $m^*/(1 - m^*)$. Alternatively, a plot of $-d\sigma/d \log t$ vs. σ should fall on a straight line with a slope of $2.303/(m^* - 1)$ at relatively long times.

Compression samples were prepared for both these tests in the same orientation as the etch samples and from the same material. The compression surfaces were lapped flat and parallel by hand. Measurements showed the ends of the samples to be parallel to within less than 0.058°. In the strain-rate-change test, the change in flow stress was determined upon the discontinuous change in strain rate in an Instron testing machine. For stress relaxation, the crosshead motion was stopped at a suitable value of the strain and the load relaxation was recorded.

Results of the strain-rate tests are shown in Fig. 21. Additional results on similar material are given in a recent publication.[100] All the curves show a definite structure: An initial increase, a more or less linear portion, and finally, an additional increase. Their shape is such that it is almost impossible to make a meaningful extrapolation to zero strain. In addition, there is not a very significant difference between one-pass and two-pass material in comparison to etch measurements which show m^* to change from 15 to 6.5 for one-pass and two-pass niobium respectively.

Insofar as the stress relaxation is concerned, Li's equations appear to describe the relaxation extremely well (Figs. 22 and 23). However,

---

[100] R. W. Armstrong, R. E. Reed and H. D. Guberman, "Characterization of the Strain Rate Dependence of the Shear Stress for Niobium Single Crystals," Scripta Met., in Press.

[redacted]

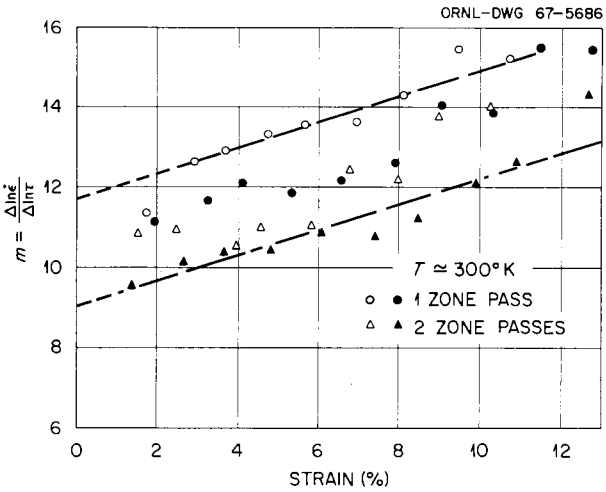

Fig. 21. Reciprocal of the Strain-Rate Sensitivity Coefficient vs. Strain for Niobium Single Crystals in Compression.

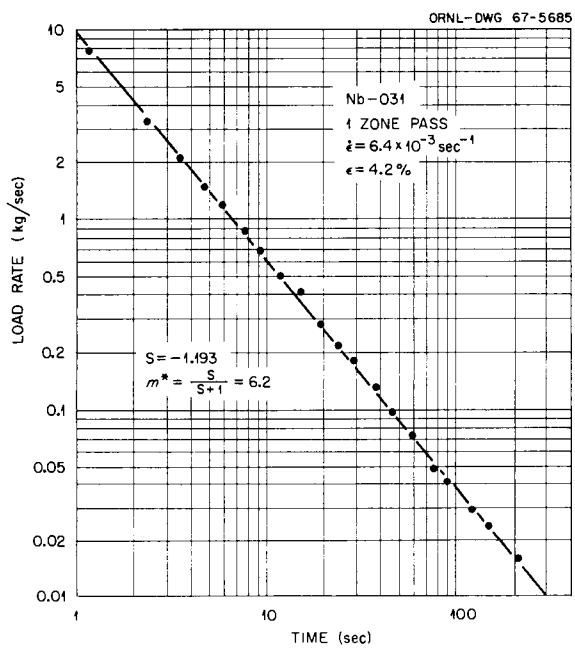

Fig. 22. Determination of the Exponent m^* from the Stress Relaxation of Single-Crystal Niobium, According to Li.

[redacted]

[redacted]

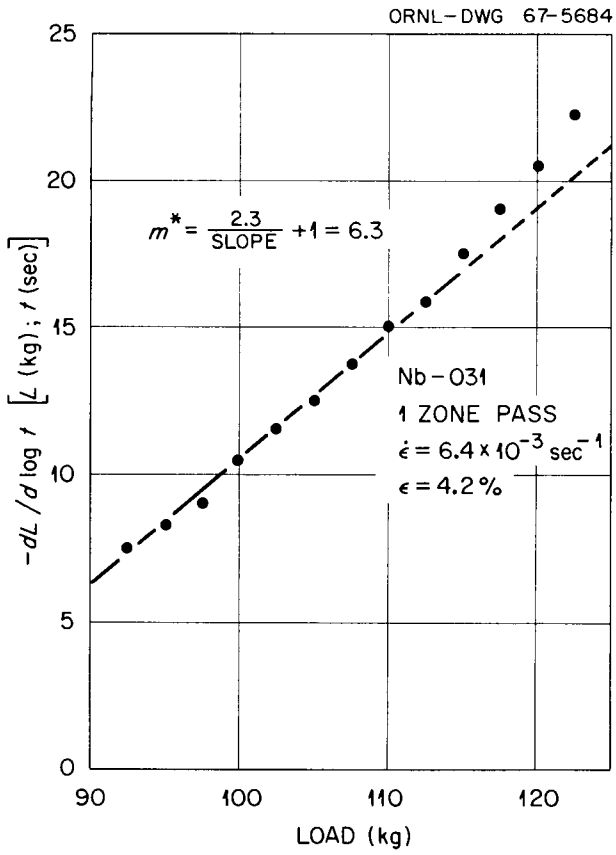

Fig. 23. Alternative Determination of the Exponent m^* from the Stress Relaxation of Single-Crystal Niobium, According to Li.

the test appears to be incapable of distinguishing between one-pass and two-pass material (Table 5). In addition, there appears to be a very definite relationship between the strain rate at which deformation was performed prior to relaxation and the value of m^* derived from the relaxation. As the strain rate increases, m^* decreases.

Thus one can only conclude that neither indirect technique can provide information on dislocation mobility, at least in single-crystal niobium. The reasons for this are not entirely clear, but it is felt that the assumption of a constant mobile dislocation density during relaxation and during strain-rate change is a difficult one to support. In the relaxation test, the variation of the derived parameters with strain rate and the insensitivity to material suggest that the test results are highly overshadowed by a machine response. In other materials, such as so-called high-purity iron and the alkali halides, where correspondence between parameters derived from etching and the indirect techniques

[redacted]

[redacted]

Table 5

Summary of Relaxation Results[a]

Sample		ϵ (%)	$\dot{\epsilon}$ (sec^{-1})	
Nb-020-1	1 Pass	1.96	1.7×10^{-4}	15.7
Nb-202-2	1 Pass	2.7	1.7×10^{-4}	15.7
Nb-023-1	2 Pass	1.15	8.5×10^{-5}	17.2
		10.8	8.5×10^{-5}	≈ 18.3
Nb-023-2	2 Pass	1.34	8.8×10^{-5}	14.3
Nb-028	1 Pass	1.1	1.3×10^{-4}	14.7
		6.07	1.3×10^{-4}	14.8
		9.36	1.3×10^{-4}	15.5
Nb-024-1	2 Pass	~2	1.3×10^{-4}	12.1
		~9	1.3×10^{-4}	13.9
Nb-024-2	2 Pass	3.9	6.5×10^{-3}	4.8
		14.9	6.5×10^{-3}	3.9
Nb-031	1 Pass	4.2	6.4×10^{-3}	6.3
Nb-032	1 Pass	4.8	6.9×10^{-3}	4.7-9.6
		13.7	6.9×10^{-3}	6.2
Nb-033	1 Pass	0.78	6.5×10^{-3}	4.4-5.9
Nb-035[b]	1 Pass	0.7	8.4×10^{-3}	6.6

(a) Tested in compression (except as noted) at room temperature, in non-irradiated crystals with a ⟨491⟩ rod axis.

(b) Tested in tension.

[redacted]

has been reported,[99] mobile interstitials are present at room temperature and should have an effect. Yet this has been ignored in all previous treatments. In at least one investigation under similar conditions,[101] i.e. relaxation under constant strain, the most prominent feature observed by means of internal friction was the pinning of dislocations by migrating point defects according to a $t^{2/3}$ law. Obviously, there may be more occurring than can perhaps be detected by a relatively crude mechanical testing machine.

[101] A. Granato, A. Hikata and K. Lücke, "Recovery of Damping and Modulus Changes Following Plastic Deformation," Acta Met. 6, 470 (1958).

[redacted]

Previous reports in this series are:

ORNL-TM-920	Period Ending June 30, 1964
ORNL-TM-960	Period Ending September 30, 1964
ORNL-TM-1000	Period Ending December 31, 1964
ORNL-TM-1100	Period Ending March 31, 1965
ORNL-TM-1200	Period Ending June 30, 1965
ORNL-TM-1270	Period Ending September 30, 1965
ORNL-TM-1400	Period Ending December 31, 1965
ORNL-TM-1500	Period Ending March 31, 1966
ORNL-TM-1570	Period Ending June 30, 1966
ORNL-TM-1700	Period Ending September 30, 1966
ORNL-TM-1720	Period Ending December 31, 1966
ORNL-TM-1825	Period Ending March 31, 1967
ORNL-TM-1941	Period Ending June 30, 1967

[redacted]

[redacted]

[redacted]

[redacted]

INTERNAL DISTRIBUTION

1–3. Central Research Library
4–5. ORNL – Y-12 Technical Library
Document Reference Section
6–15. Laboratory Records Department
16. Laboratory Records, ORNL R.C.
17. ORNL Patent Office
18. G. M. Adamson, Jr.
19. J. H. Barrett
20. S. E. Beall
21. R. J. Beaver
22. M. Bender
23. R. G. Berggren
24. J. O. Betterton, Jr.
25. D. S. Billington
26. A. L. Boch
27. B. S. Borie
28. G. E. Boyd
29. R. B. Briggs
30. R. E. Brooksbank
31. W. E. Brundage
32. D. A. Canonico
33. R. M. Carroll
34. J. V. Cathcart
35. G. W. Clark
36. K. V. Cook
37. G. L. Copeland
38. F. L. Culler
39. J. E. Cunningham
40. J. H. DeVan
41. C. V. Dodd
42. K. Farrell
43. J. I. Federer
44. D. E. Ferguson
45. B. E. Foster
46. A. P. Fraas
47. J. H Frye, Jr.
48. R. J. Gray
49. W. R. Grimes
50. H. D. Guberman
51. D. G. Harman
52. W. O. Harms
53–54. M. R. Hill
55. N. E. Hinkle
56. D. O. Hobson
57. H. W. Hoffman
58. R. W. Horton
59. W. R. Huntley
60. H. Inouye
61. G. W. Keilholtz
62. B. C. Kelley
63. J. A. Lane
64. A. P. Litman
65. A. L. Lotts
66. R. N. Lyon
67. H. G. MacPherson
68. R. E. MacPherson
69. M. M. Martin
70. W. R. Martin
71. R. W. McClung
72. H. E. McCoy, Jr.
73. H. C. McCurdy
74. R. E. McDonald
75. D. L. McElroy
76. C. J. McHargue
77. F. R. McQuilkin
78. A. J. Miller
79. E. C. Miller
80. J. G. Morgan
81. F. H. Neill
82. T. A. Nolan (K-25)
83. S. M. Ohr
84. P. Patriarca
85. A. M. Perry
86. S. Peterson
87. R. E. Reed
88. P. L. Rittenhouse
89. W. C. Robinson
90. M. W. Rosenthal
91. G. Samuels
92. A. W. Savolainen
93. J. L. Scott
94. O. Sisman
95. G. M. Slaughter
96. S. D. Snyder
97. I. Spiewak
98. J. T. Stanley
99. W. J. Stelzman
100. J. O. Stiegler
101. D. B. Trauger
102. R. P. Tucker

[redacted]

[redacted]

103. J. T. Venard
104. G. M. Watson
105. M. S. Wechsler
106. A. M. Weinberg
107. J. R. Weir, Jr.
108. W. J. Werner
109. H. L. Whaley
110. G. D. Whitman
111. J. M. Williams
112. R. O. Williams
113. J. C. Wilson
114. R. G. Wymer
115. F. W. Young, Jr.
116. C. S. Yust

EXTERNAL DISTRIBUTION

117–120. F. W. Albaugh, Battelle, PNL
121–123. R. J. Allio, Westinghouse Atomic Power Division
124. R. D. Baker, Los Alamos Scientific Laboratory
125. C. Baroch, Babcock and Wilcox
126. L. Brewer, University of California, Berkeley
127. V. P. Calkins, GE, NMPO
128. S. Christopher, Combustion Engineering, Inc.
129. D. B. Coburn, Gulf, General Atomic
130. D. F. Cope, RDT, SSR, AEC, Oak Ridge National Laboratory
131. G. K. Dicker, Division of Reactor Development and Technology, AEC, Washington
132. D. E. Erb, Division of Reactor Development and Technology, AEC, Washington
133. E. A. Evans, GE, Vallecitos
134. W. C. Francis, Idaho Nuclear Corporation
135. A. J. Goodjohn, Gulf, General Atomic
136. J. F. Griffo, Division of Space Nuclear Systems, AEC, Washington
137. R. G. Grove, Mound Laboratory
138. D. H. Gurinsky, BNL
139. A. N. Holden, GE, APED
140–142. J. S. Kane, Lawrence Radiation Laboratory, Livermore
143. H. Kato, U.S. Department of the Interior, Bureau of Mines
144. E. A. Kintner, Fuel Fabrication Branch, AEC, Washington
145. J. H. Kittel, ANL
146. E. J. Kreih, Westinghouse, Bettis Atomic Power Laboratory
147. W. J. Larkin, AEC, Oak Ridge Operations
148. W. L. Larsen, Iowa State University, Ames Laboratory
149. C. F. Leitten, Jr., Linde Division, Union Carbide Corp.
150. P. J. Levine, Westinghouse Advanced Reactor Division, Waltz Mill Site, Box 158, Madison, Pa. 15663
151. J. J. Lombardo, NASA, Lewis Research Center
152. J. H. MacMillan, Babcock and Wilcox
153. C. L. Matthews, RDT, SR, AEC, Oak Ridge National Laboratory
154. M. McGurty, GE, NMPO
155. M. Nevitt, ANL
156. R. E. Pahler, Division of Reactor Development and Technology, AEC, Washington
157. S. Paprocki, BMI
158. W. E. Ray, Westinghouse Advanced Reactor Division, Waltz Mill Site, Box 158, Madison, Pa. 15663

[redacted]

[redacted]

159. W.L.R. Rice, AGMR, AEC, Washington
160. B. Rubin, Lawrence Radiation Laboratory, Livermore
161. F. C. Schwenk, Division of Reactor Development and Technology, AEC, Washington
162. P. G. Shewmon, ANL
163–165. J. M. Simmons, Division of Reactor Development and Technology, AEC, Washington
166. L. E. Steele, Naval Research Laboratory
167. R. H. Steele, Division of Reactor Development and Technology, AEC, Washington
168. W. F. Sheely, Division of Research, AEC, Washington
169. A. Strasser, United Nuclear Corporation
170. A. Taboada, Division of Reactor Development and Technology, AEC, Washington
171. A. Van Echo, Division of Reactor Development and Technology, AEC, Washington
172. R. Van Tyne, Illinois Institute of Technology Research Institute
173. James Watson, Gulf, General Atomic
174. C. E. Weber, Atomics International
175. J. F. Weissenberger, RDT, OSR, GE, NMPO
176. G. W. Wensch, Division of Reactor Development and Technology, AEC, Washington
177. G. A. Whitlow, Westinghouse Advanced Reactor Division, Waltz Mill Site, Box 158, Madison, Pa. 15663
178. E. A. Wright, AEC, Washington
179. Laboratory and University Division, AEC, Oak Ridge Operations
180–194. Division of Technical Information Extension

[redacted]